UNIVERSITÉ DU LUXEMBOURG

PhD-FSTC-2012-08

The Faculty of Sciences, Technology and Communication

DISSERTATION

Defense held on 05/03/2012 in Luxembourg

to obtain the degree of

DOCTEUR DE L'UNIVERSITÉ DU LUXEMBOURG EN PHYSIQUE

by

Georg Friedrich ALTENHÖFER

Born on 7th of July 1979 in Lippstadt (Germany)

Photo Hall Measurements on $CuInSe_2$

Dissertation defense committee

Dr. Susanne Siebentritt, Dissertation Supervisor
Professor, University of Luxemburg

Dr. Roland Sanctuary, Chairman
Professor, University of Luxemburg

Dr. Sascha Sadewasser, Vice Chairman
International Iberian Nanotechnology Laboratory, Braga (Portugal)

Dr. Silvana Botti
École Polytechnique-CNRS-CEA, Palaiseau (France)
CNRS-Université Lyon 1, Villeurbanne (France)

Dr. Levent Gütay
University of Luxemburg

Contents

Chapter 1

Introduction

The photovoltaic market today is dominated by crystalline silicon cells, although the production of crystalline silicon wafers is a very material and energy consuming process. The absorber layers have a thickness of around 200 μm and a lot of material gets lost in the process of cutting the wafers.

The development of thin film solar cells aims at reducing material consumption to a minimum by using highly absorptive material which is deposited directly on a substrate. There are different types of thin film cells available on the market of which Cu(In,Ga)Se_2 cells deliver the highest efficiencies. Cu(In,Ga)Se_2 for photovoltaic applications has to be in the chalcopyrite crystal structure and can be grown with every desired indium to gallium ratio from pure $CuInSe_2$ to pure $CuGaSe_2$. This makes it possible to adapt the absorber band gap to the optimal value for the energy conversion of the incident sunlight.

Cu(In,Ga)Se_2 photovoltaic modules are available on the market for several years now and today have reached efficiencies of up to 13.4% in mass production. Record efficiencies reach 15.7% [Gre11] for a module and 20.3% [Jac11] with a 0.50 cm^2 laboratory cell.

The standard Cu(In,Ga)Se_2 cell is designed as follows: A molybdenum backcontact is sputtered on a glass substrate. The next step is the p-type Cu(In,Ga)Se_2 absorber layer. An advantage of Cu(In,Ga)Se_2 is the tunable bandgap that can be varied with the gallium to indium ratio between the band gaps of $CuInSe_2$ (1.0 eV) and $CuGaSe_2$ (1.6 eV). The most efficient cells have polycrystalline absorber layers, produced by a PVD[1] process with a gallium to indium ratio of around 30/70. On top of the absorber is a buffer layer, usually consisting of CdS that acts as a diffusion barrier and improves the band alignment between absorber and window layer. The transparent ZnO window layer forms the n-type part of the p-n junction. Finally a grid of a Ni/Al double layer is deposited on top as the front contact.

Despite the success of Cu(In,Ga)Se_2 solar cells, many material properties are not known and research is done on the structure and materials of the cell as well as on alternative production processes [Sche11].

After the generation of an electron hole pair in the absorber, the charge carrier transport properties of the materials are extremely important for the transport of holes and electrons to the front and back contact respectively.

[1] Physical Vapour Deposition

Usually studies of the transport properties are made with the sample in the dark. Electrical properties like the charge carrier density and mobility can be measured using the Hall effect and require strong magnetic fields of several Tesla. The superconducting magnets typically used to generate those fields in most cases do not have an optical feedthrough. Hence it is not possible to illuminate the sample.

Nevertheless, people tend to use solar cells under illumination, so that it is important to be able to describe and control the effects of incident photons.

In first place, a semiconductor under illumination experiences an additional source of charge carriers: the light induced generation of electron hole pairs. But this is only the most obvious effect. The incident photons can lead to serious changes in the electronic structure of the semiconductor. To detect such changes, Hall effect measurements under illumination – so called photo hall measurements – can be used.

Up to now, a photo Hall study for chalcopyrites was only done for $CuGaSe_2$ on epitaxially grown and polycrystalline thin films [Ris07, Sie08].

Based on the results, it was assumed for the epitaxial $CuGaSe_2$ films that also under illumination, the electrical transport is dominated by free holes originating from thermally activated defect states inside the band gap while the influence of photo generated electrons is small enough to be neglected. However, the illumination lead to the disappearance of the compensating donors, which was assigned to the light induced transformation of metastable donors to acceptors.

The aim of this work is to investigate if those effects occur similarly in other chalcopyrite compounds. Theoretical considerations show that the behaviour of defects in different chalcopyrite compounds is similar, but not identical (see. e.g. [Lan06]).

In $Cu(In,Ga)Se_2$ compounds with both indium and gallium, one can not exclude local fluctuations of the gallium to indium ratio [Gue10]. Therefore, this work only discusses properties of the ternary compound $CuInSe_2$.

Chapter 2 gives an overview of the basic effect responsible for the electric transport in semiconductors and chalcopyrites and a literature review about the properties of $CuInSe_2$.

In chapters 3 and 4, the experimental methods and equipment are introduced.

Simulations of the influences of different charge carrier generating effects on the interpretation of experimental data are introduced in Chapter 5.

The results of measurements performed in the dark are discussed in chapter 6 and the behaviour of samples with different electronic configurations is explained. In chapter 7, the effects occurring under illumination of the $CuInSe_2$ thin films are presented.

Chapter 8 finally summarises the work.

Chapter 2

Background on Electrical Transport

2.1 Electrical Transport Properties of Semiconductors

2.1.1 Charge Carrier Statistics

In the ground state of a semiconductor, all states in the valence band are filled while the conduction band is empty. In that state no charge transport is possible. Through excitation, for example by temperature or light, electrons can reach the conduction band, leaving a hole in the valence band, so that conduction in both bands becomes possible.

The occupation probability of a state at a certain energy level E in a semiconductor with the Fermi Energy E_F is given by the Fermi-Dirac-Statistics:

$$f(E) = \frac{1}{e^{\frac{E-E_F}{k_B T}} + 1} \tag{2.1}$$

The charge carrier densities in the conduction and valence band can be calculated as

$$n = \int_{E_C}^{\infty} D_C(E) f(E) dE, \tag{2.2a}$$

$$p = \int_{-\infty}^{E_V} D_V(E)[1 - f(E)] dE, \tag{2.2b}$$

where $D_C(E)$ and $D_V(E)$ are the densities of state in the conduction band and valence band, respectively.

$$D_C = 4\pi \left(\frac{2m_n^*}{h^2}\right)^{\frac{3}{2}} \sqrt{(E - E_C)} \tag{2.3a}$$

$$D_V = 4\pi \left(\frac{2m_p^*}{h^2}\right)^{\frac{3}{2}} \sqrt{(E_V - E)} \tag{2.3b}$$

$m_{n,p}^*$ is the effective mass of a charge carrier. It is defined analogous to Newton's second law $m = F/a$ as the inverse of the second derivative of the band $E(k)$ with respect to the momentum k. The effective mass is a symmetric tensor m_{ij}^*, so that the coordinate system can be chosen in a way that the components m_{ij}^* are zero for $i \neq j$ and the diagonal elements can be written

$$m_{ii}^* = \pm\hbar^2 \left(\frac{\delta^2 E(k)}{(\delta k_i)^2}\right)^{-1}. \tag{2.4}$$

Using Equations (2.1),(2.2) and (2.3), one obtains:

$$n = \int_{E_C}^{\infty} 4\pi \left(\frac{2m_n^*}{h^2}\right)^{\frac{3}{2}} \cdot \frac{\sqrt{(E-E_C)}}{e^{\frac{E-E_F}{k_BT}}+1}\, dE \tag{2.5a}$$

$$p = \int_{-\infty}^{E_V} 4\pi \left(\frac{2m_p^*}{h^2}\right)^{\frac{3}{2}} \cdot \frac{\sqrt{(E_V-E)}}{e^{\frac{E_F-E}{k_BT}}+1}\, dE \tag{2.5b}$$

By introducing

$$\eta_n = \frac{E_F - E_C}{k_BT} \qquad \text{for the conduction Band and} \tag{2.6a}$$

$$\eta_p = \frac{E_V - E_F}{k_BT} \qquad \text{for the valence Band} \tag{2.6b}$$

and using the Fermi-Dirac-integral $F_{1/2}$

$$F_{1/2}(\eta) = \frac{2}{\sqrt{\pi}} \int_0^{\infty} \frac{\sqrt{\varepsilon}\, d\varepsilon}{1+e^{\varepsilon-\eta}} \tag{2.7}$$

(2.5) can be written as

$$n = N_C F_{1/2}(\eta_n) \tag{2.8a}$$

$$p = N_V F_{1/2}(\eta_p) \tag{2.8b}$$

N_V and N_C are the effective densities of states of the conduction band and the valence band respectively.

$$N_C = 2\left(\frac{2\pi m_n^* k_B T}{h^2}\right)^{3/2} \tag{2.9a}$$

$$N_V = 2\left(\frac{2\pi m_p^* k_B T}{h^2}\right)^{3/2} \tag{2.9b}$$

The Fermi-Dirac-Integral can only be solved numerically, but if the Fermi level is inside the band gap and the distance to the band edges is considerably higher than k_bT ($\eta_{n,p} \gg 1$), it can be approximated by e^{η} so that we finally obtain the expressions

$$n = N_C \cdot e^{\frac{E_F-E_C}{k_BT}}, \text{ and} \tag{2.10a}$$

$$p = N_V \cdot e^{\frac{E_V-E_F}{k_BT}}. \tag{2.10b}$$

2.1.2 Doping

The properties of semiconductors can be influenced by adding doping defects to the pure semiconductor. In an elemental semiconductor these can be atoms of other elements, but also vacancies (missing atoms) in the crystal lattice or interstitial atoms (atoms placed between the lattice points). In compound semiconductors, there can also be anti-sites (elements of the compound that occupied a lattice point of an other element). The dopants create additional states in the band structure and can act either as donors (if they provide an electron) or as acceptors (if they can catch an electron). If the concentration of dopants

$N_{A,D}$ is high enough, the charge carrier distribution of the semiconductor will be changed significantly.

If we look at the whole crystal, it will always be charge neutral in equilibrium. This means that the sum of densities of the electrons in the conduction band and the negatively charged acceptors N_A^- is equal to the sum of densities of the holes in the valence band and the positively charged donors N_D^+, i.e.,

$$n + N_A^- = p + N_D^+. \tag{2.11}$$

The activation probability is given by Equation (2.1) and thus can be written for acceptors and donors:

$$N_A^- = \frac{N_A}{g e^{\frac{E_A - E_F}{k_B T}} + 1} \tag{2.12}$$

$$N_D^+ = \frac{N_D}{\frac{1}{g} e^{\frac{E_F - E_D}{k_B T}} + 1}, \tag{2.13}$$

with g the degeneracy factor of the doping level and E_A and E_D the energy levels of the acceptor and donor respectively. We define the activation energy $E_{a,d}$ of an acceptor or donor as the distance to the band edges:

$$E_a = E_A - E_V \tag{2.14}$$

$$E_d = E_C - E_D \tag{2.15}$$

Doping a semiconductor with donors will move the Fermi energy towards the conduction band and thereby increase the concentration n of electrons in the conduction band (Eq. (2.10a)). An important value for charge carrier statistics is the inversion density $n_i = n \cdot p$. It defines the carrier density at which the transition from n- to p-conduction takes place. A semiconductor with $n > \sqrt{n_i} > p$ is n-type, while a material with $p > \sqrt{n_i} > n$ is p-type. With Equations (2.10a) and (2.10b), we obtain the following expression:

$$n_i = n \cdot p = N_C N_V \mathrm{e}^{\frac{E_V - E_C}{k_B T}} = N_C N_V \mathrm{e}^{\frac{-E_G}{k_B T}} \tag{2.16}$$

As the product of n and p does not depend on the Fermi energy, an increase of n means that the concentration p of holes in the valence band must be decreased. If the semiconductor is doped with acceptors, the opposite can be observed: The Fermi level shifts towards the valence band, p increases and n decreases. For an undoped semiconductor, where electrons in the conduction band and holes in the valence band can only be generated simultaneously it holds: $n = p = \sqrt{n_i}$.

Doped Semiconductor with one Acceptor Level

Now we consider a semiconductor with only one acceptor level and a negligible density of electrons in the conduction band ($N_D = N_D^+ = 0$, $n \ll p$). Equation (2.11) then can be approximated as

$$p = N_A^- \tag{2.17}$$

With Eqns. (2.12), (2.10b) and (2.14), we obtain:

$$p = \frac{N_A}{g \cdot e^{\frac{E_A - E_F}{k_B T}} + 1} \tag{2.18}$$

$$= \frac{N_A}{g \cdot e^{\frac{E_A - E_V + E_V - E_F}{k_B T}} + 1} = \frac{N_A}{g \cdot e^{\frac{E_V - E_F}{k_B T}} e^{\frac{E_A - E_V}{k_B T}} + 1} \tag{2.19}$$

$$= \frac{N_A}{g \cdot \frac{p}{N_V} e^{\frac{E_a}{k_B T}} + 1} \tag{2.20}$$

This is a cubic equation in p that can be solved by

$$p = \frac{N_V}{2g} e^{-\frac{E_a}{k_B T}} \cdot \left(\sqrt{1 + \frac{4 N_A g}{N_V} e^{\frac{E_a}{k_B T}}} - 1 \right). \tag{2.21}$$

For $k_B T \ll E_a$ or $e^{\frac{E_a}{k_B T}} \gg 1$ we finally can write:

$$p = \sqrt{\frac{N_V N_A}{g}} e^{\frac{-E_a}{2 k_B T}} \tag{2.22}$$

For an n-type semiconductor with one donor level, a similar expression can be derived:

$$n = \sqrt{\frac{N_C N_D}{g}} e^{\frac{-E_d}{2 k_B T}} \tag{2.23}$$

2.1.3 Compensated Semiconductors

A semiconductor containing both acceptor and donor states in the band gap is called compensated. In general the densities of donors and acceptors will not be exactly the same so that the semiconductor is only partially compensated.

One Acceptor and One Donor

As an example, we calculate the equations for a compensated p-type semiconductor with $N_A > N_D$ and $p \gg n$. For a p-type semiconductor, E_F lies below the middle of the band gap so that

$$E_F - E_D \ll -1, \quad \text{and hence} \quad g e^{\frac{E_F - E_D}{k_B T}} \ll 1. \tag{2.24}$$

This means that all donors are ionised (see Eq. (2.13)): $N_D^+ = N_D$. In this case (2.11) can be approximated as

$$p + N_D = N_A^- \tag{2.25}$$

and can be solved similar to (2.18)-(2.20):

$$p + N_D = \frac{N_A}{g e^{\frac{E_A - E_F}{k_B T}} + 1} \tag{2.26}$$

$$= \frac{N_A}{g \cdot \frac{p}{N_V} e^{\frac{E_a}{k_B T}} + 1} \tag{2.27}$$

This term can again be solved by

$$p = -\frac{N_D + \frac{N_V}{g} e^{-\frac{E_a}{k_B T}}}{2} + \sqrt{\left(\frac{N_D + \frac{N_V}{g} e^{-\frac{E_a}{k_B T}}}{2}\right)^2 + (N_A N_V - N_D N_V)\frac{N_V}{g} e^{-\frac{E_a}{k_B T}}}. \tag{2.28}$$

For low temperatures, the free carrier density p can be neglected with respect to the donor concentration N_D, and Equation (2.25) can be rewritten as follows:

$$(2.25) \quad \overset{p \ll N_D}{\Longrightarrow} \quad N_D = N_A^- = \frac{N_A}{g e^{\frac{E_a}{k_B T}} \frac{p}{N_V} + 1} \tag{2.29}$$

$$\Longrightarrow \quad p = \frac{N_V (N_A - N_D)}{g N_D} e^{-\frac{E_a}{k_B T}} \tag{2.30}$$

A similar expression can be obtained for a compensated n-type semiconductor:

$$n = \frac{N_C (N_D - N_A) g}{N_A} e^{-\frac{E_a}{k_B T}} \tag{2.31}$$

Multiple Defect Levels

If more than two defect levels have to be taken into account, Equation (2.11) has to be enhanced by additional numbers of charged defects N_{Ai}^- and N_{Di}^+. This leads to a cubic or higher order equation that is not analytically solvable. Therefore, the solution has to be found numerically.

This is done by calculating the defect activations (Eqns. (2.12) and (2.13)) and the free carrier densities (2.10) with a random Fermi level, then check with Equation (2.11) if the resulting charge is positive or negative, and shift the Fermi level up or down respectively. An example program code can be found in chapter C.1.

However, this numerical solution can also be used for one and two band conduction.

2.1.4 Charge Carrier Transport

The Drude model gives a descriptive explanation for the charge transport in materials.

A free charge carrier with charge q in a semiconductor will be scattered randomly on lattice defects and phonons, which leads to an average velocity of $\langle v_{th} \rangle = 0$. In the presence of an electric field $\vec{E}$, the field force $\vec{F} = q\vec{E}$ accelerates the carrier during the relaxation time τ between two collisions to an additional velocity $\vec{v}$. After each collision the information on the additional velocity is lost, so that the carrier will adopt an average drift velocity v_d. This, however, is an approximation because the relaxation time depends on the energy of the carrier and moreover this energy dependence is different for each scattering process.

The equation of motion for a charge carrier in a solid is then [Kit06]

$$\vec{F} = q \cdot \vec{E} = m^* (\frac{d}{dt} + \frac{1}{\tau}) \vec{v} \tag{2.32}$$

If measurements are performed in a stationary state with $\frac{d\vec{v}}{dt} = 0$, the equation of motion is simplified to

$$q \cdot \vec{E} = m^* \frac{\vec{v}}{\tau} \tag{2.33}$$

Solving this expression to $\vec{v}$, leads to a linear relation between $\vec{v}$ and $\vec{E}$ with the mobility μ as the proportionality factor.

$$\Rightarrow \vec{v} = \frac{q\tau}{m^*}\vec{E} = \pm\mu\vec{E} \tag{2.34}$$

$$\mu = \frac{|q|\tau}{m^*} \tag{2.35}$$

The sign in 2.34 depends on the sign of the charge q. For electrons with $q = -e$ it is negative, for holes with $q = e$ it is positive. In presence of a magnetic field, the Lorentz force gives an additional contribution to the equation of motion:

$$q \cdot (\vec{E} + \vec{v} \times \vec{B}) = m^* \frac{\vec{v}}{\tau} \tag{2.36}$$

$$\Rightarrow \vec{v} = \pm\mu(\vec{E} + \vec{v} \times \vec{B}) \tag{2.37}$$

The current density $\vec{j}$ can be expressed as the product of charge q, density n and drift velocity $\vec{v}$ of the charge carrier:

$$\vec{j} = q\vec{v}n = \begin{cases} -e\vec{v}n = en\mu\vec{E} & \text{for electrons} \\ e\vec{v}p = ep\mu\vec{E} & \text{for holes} \end{cases} \tag{2.38}$$

With (2.37), one obtains:

$$\vec{j} = \pm qn\mu(\vec{E} + \frac{1}{qn}\vec{j} \times \vec{B}) = \pm qn\mu\vec{E} \pm \mu\vec{j} \times \vec{B} = en\mu\vec{E} \pm \mu\vec{j} \times \vec{B} \tag{2.39}$$

With the B-field in z-direction and $B_z = B$, the vector product $\vec{j} \times \vec{B}$ can be calculated to:

$$\vec{B} = \begin{pmatrix} 0 \\ 0 \\ B \end{pmatrix} \Rightarrow \vec{j} \times \vec{B} = \begin{pmatrix} j_y B \\ -j_x B \\ 0 \end{pmatrix} \tag{2.40}$$

If the E-field component in z-direction is zero, $E_z = 0$, the components of the current density are

$$j_x = ne\mu E_x \pm \mu j_y B \tag{2.41a}$$

$$j_y = ne\mu E_y \mp \mu j_x B \tag{2.41b}$$

$$j_z = 0 \tag{2.41c}$$

(2.41a) and (2.41b) inserted into each other lead to

$$j_x = ne\mu E_x \pm nq\mu^2 E_y B - \mu^2 B^2 j_x \tag{2.42a}$$

$$j_y = ne\mu E_y \mp nq\mu^2 E_x B - \mu^2 B^2 j_y, \tag{2.42b}$$

and thus

$$j_x = \frac{ne\mu E_x \pm nq\mu^2 E_y B}{1 + \mu^2 B^2} \tag{2.43a}$$

$$j_y = \frac{ne\mu E_y \mp nq\mu^2 E_x B}{1 + \mu^2 B^2} \tag{2.43b}$$

(2.43) can be written as:

$$\vec{j} = \frac{ne\mu}{1+\mu^2B^2} \begin{pmatrix} 1 & \pm\mu B \\ \mp\mu B & 1 \end{pmatrix} \cdot \vec{E} \tag{2.44}$$

$$= \underline{\sigma} \cdot \vec{E} \tag{2.45}$$

The proportionality factor is the conductivity tensor $\underline{\sigma}$. The sign in the non diagonal elements of the tensor depends on the charge. With

$$\sigma := ne\mu \tag{2.46a}$$

$$\gamma := \mu B \tag{2.46b}$$

the tensor can be written for electrons

$$\underline{\sigma_n} = \frac{ne\mu_n}{1+\mu_n^2B^2} \begin{pmatrix} 1 & -\mu_n B \\ \mu_n B & 1 \end{pmatrix} = \frac{\sigma_n}{1+\gamma_n^2} \begin{pmatrix} 1 & -\gamma_n \\ \gamma_n & 1 \end{pmatrix}, \tag{2.47}$$

and for holes

$$\underline{\sigma_p} = \frac{pe\mu_p}{1+\mu_p^2B^2} \begin{pmatrix} 1 & \mu_p B \\ -\mu_p B & 1 \end{pmatrix} = \frac{\sigma_p}{1+\gamma_p^2} \begin{pmatrix} 1 & \gamma_p \\ -\gamma_p & 1 \end{pmatrix}. \tag{2.48}$$

If more than one type of charge carriers is present in the semiconductor, the conductivity tensor is the sum of the individual tensors

$$\underline{\sigma} = \underline{\sigma_1} + \underline{\sigma_2} + \underline{\sigma_3} + \cdots \tag{2.49}$$

2.1.5 Charge Carrier Mobility

The different scattering processes of the charge carriers inside the crystal are responsible for the limitation of the carrier mobility in solids. An important parameter for the description of those processes is the scattering cross section σ_i of the different scattering centres. σ_i can be regarded as an area around the scattering centre and is a measure for the effectiveness of the interaction. The average time τ_i between two scattering processes can be calculated from σ_i, the density of centres N_i, and the thermal velocity[1] v_{th}.

$$\frac{1}{\tau_i} = v_{th} N_i \sigma_i \tag{2.50}$$

The cross sections σ_i can be theoretically calculated and converted into mobilities μ_i by Equations (2.35) and (2.50). The resulting expressions for the carrier mobilities are given in an overview following [See02], [Ris07] and [Sie05]:

- **Neutral Impurity Scattering:** The scattering of charge carriers on neutral impurities was described by [Erg50], similar to the scattering of low-energy electrons in a gas. The resulting mobility is independent of the temperature (for constant

[1] The time between two collisions is dominated by the thermal velocity v_{th} because the additional drift velocity v_d resulting from the electric field is significantly smaller. Thus, v_d is only an effective velocity resulting from averaging over the whole ensemble of carriers.

impurity density N_N) and directly proportional to the effective mass, being the only mechanism leading to higher mobilities for higher carrier effective masses.

$$\mu_N = \frac{e}{20 a_B \hbar N_N} \quad \text{, with} \tag{2.51a}$$

$$a_B = \frac{\epsilon_0 \epsilon_r \hbar^2}{m^* e^2} \tag{2.51b}$$

- **Ionised Impurity Scattering:** Scattering on ionised impurities with the density N_I can be described by the Brooks Herring model [Bro51]. The cross section is calculated under the assumption of a screened coulomb potential.

$$\mu_{BH} = \frac{2^{7/2}(4\pi\epsilon_r\epsilon_0)^2}{\pi^{3/2} e^3 N_I f(\beta)} \cdot \frac{(k_B T)^{3/2}}{\sqrt{m^*}} \quad \text{, with} \tag{2.52a}$$

$$\beta = \frac{2\sqrt{6} k_B T}{e\hbar} \sqrt{\frac{m^* \epsilon_r \epsilon_0}{p}} \quad \text{and} \tag{2.52b}$$

$$f(x) = \ln(1 + x^2) - \frac{x^2}{1 + x} \tag{2.52c}$$

- **Acoustic Phonon Scattering:** Acoustic phonons correspond to vibrations where all lattice atoms oscillate in the same phase. The deformation of the crystal causes a scattering potential [Bar50].

$$\mu_{AC} = \frac{2}{3} \cdot \sqrt{2\pi} \frac{e\hbar^4 \rho v_s^2}{E_{ac}^2} \cdot \frac{1}{m^{*5/2} (k_B T)^{3/2}}, \tag{2.53}$$

with E_{ac} the deformation potential constant, ρ the density of the material and v_s the velocity of sound.

- **Piezoelectric scattering:** Acoustic phonons cause a polarisation in crystals with ionic bonds and a non symmetric unit cell. Scattering on the resulting dipole moment is called piezoelectric scattering.

$$\mu_{PZ} = \frac{16\sqrt{2\pi}}{3} \frac{\hbar \epsilon_r \epsilon_0}{e K^2} \cdot \frac{1}{m^{*3/2} (k_B T)^{1/2}} \tag{2.54a}$$

$$\frac{K^2}{1 - K^2} = \frac{\frac{e_{pz}^2}{\rho v_s}}{\epsilon_r \epsilon_0 + \frac{e_{pz}^2}{\rho v_s^2}} \tag{2.54b}$$

with e_{pz} the piezoelectric constant.

- **Optical phonon scattering:** In compound crystals, the ions of the sublattices can oscillate with a phase shift. The corresponding phonons are called optical phonons.

$$\mu_{NPO} = \frac{4\sqrt{2\pi} e\hbar\rho (k_B \Theta)^{1/2}}{3 m^{*5/2} D^2} \cdot f\left(\frac{T}{\Theta}\right), \tag{2.55a}$$

with

$$f\left(\frac{T}{\Theta}\right) = (2z)^{5/2}(\mathrm{e}^{2z}-1)\int_0^\infty \frac{y^{3/2}\mathrm{e}^{-2zy}dy}{\sqrt{y+1}+\mathrm{e}^{2z}Re(\sqrt{y-1})} \tag{2.55b}$$

$$\approx \exp\left(5.44\left(\frac{1}{\sqrt{T/\Theta}}\right)-1\right) \tag{2.55c}$$

$$z = \frac{\Theta}{2T} \tag{2.55d}$$

$$y = \frac{E}{k_B\Theta} \tag{2.55e}$$

with D the optical deformation constant, Θ the typical temperature of the phonons and E the energy of the carriers within the band.

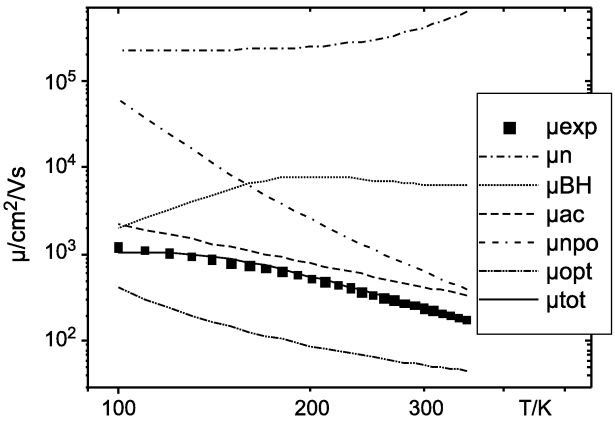

Figure 2.1: *Modelled partial mobilities for a $CuGaSe_2$ sample and the resulting total mobility μ_{tot} compared to the experimental mobility [Sie05]. The polar optical scattering μ_{opt} is not considered for the calculation of the total mobility.*

- **Polar optical phonon scattering:** Similar to the piezoelectric scattering, there is additionally a polarisation due to optical phonons.

$$\mu_{PO} = \frac{3\pi^{1/2}}{2^{5/2}}\frac{|e|}{m^*\alpha\omega_0}\frac{\sinh(z)}{z^{3/2}K_1(z)} \tag{2.56a}$$

$$\alpha = \frac{\hbar|e|E_0}{\sqrt{2m^*}(k_B\Theta)^{3/2}} \tag{2.56b}$$

$$E_0 = \frac{|e|m^*k_B\Theta}{4\pi\epsilon_0\hbar^2}\left(\epsilon_\infty^{-1}-\epsilon_r^{-1}\right) \tag{2.56c}$$

- **Grain boundaries:** High defect densities at grain boundaries form a space charge region an thus a barrier for the charge carriers. The effect on the mobility can be described by

$$\mu_{GB} = \mu_0\mathrm{e}^{\frac{\Phi}{k_BT}}, \tag{2.57}$$

with Φ the barrier height and μ_0 a quantity proportional to the grain size.

For the interpretation of experimental data, the dependencies of the measured carrier mobility on temperature and effective carrier mass give information on the dominating scattering mechanism. For example, one can clearly distinguish between impurity scattering and phonon scattering: All phonon related processes lead to a decreasing mobility with increasing temperature, while the impurity scattering processes show an increasing (ionised impurities) or constant (neutral impurities) mobility for increasing temperature. The total mobility μ_{tot} can be derived with Matthiessen's rule from the partial mobilities:

$$\frac{1}{\mu_{tot}} = \frac{1}{\mu_1} + \frac{1}{\mu_2} + \frac{1}{\mu_3} + ... \tag{2.58}$$

Figure 2.1 shows partial and total mobility fitted to experimental data from a $CuGaSe_2$ sample.

2.1.6 Hopping

At low temperatures, the free carriers in conduction band and valence band band freeze out and at the same time more and more defects are not occupied. Hence, a visible contribution to the transport can originate from carriers tunnelling from defect to defect. If the defect density is high enough, the wave functions of the defects overlap and form an additional band inside the band gap, the so called impurity band.

The conductivity of a semiconductor can then be expressed approximately as [Bla85]

$$\sigma = pe\mu_p + \sigma_2 exp(-\frac{\epsilon_2}{k_B T}) + \sigma_3 exp(-\frac{\epsilon_3}{k_B T}). \tag{2.59}$$

The first term describes conduction in the bands, while the second and third terms correspond to different types of impurity conduction. ϵ_2 corresponds to the energy needed to place a second electron on a neutral donor. The conduction of this type takes place in a band of negatively charged donors (D^--band). The third term describes the hopping of carriers from neutral to ionised defects.

In Hall measurements, high influence of impurity conduction leads to a maximum of the Hall coefficient and steeply decreasing mobility towards low temperatures.

2.2 Properties of $CuInSe_2$

2.2.1 Crystal and Electronic Band Structure

The chalcopyrite structure can be deduced from the zincblende[2] structure (II-IV semiconductor, e.g. ZnSe) by replacing the atoms of the cation lattice (group II element, Zn) alternately by a group I (e.g. Cu) and a group III (e.g. In, Ga) element. Doing this, the zincblende unit cell has to be doubled to form the chalcopyrite unit cell (Fig. 2.2).

Due to the different bond lengths R_{I-VI} and R_{III-VI} between selenium anions and the two different types of cations, the Se atoms are slightly moved from their position in the zincblende lattice. For $CuInSe_2$, the Se anions are shifted towards the Cu atoms [Pos04].

[2]The zincblende structure can be regarded as two face centred cubic (fcc) lattices with a translational displacement of $\frac{1}{4}$ along the cube diagonal. One of those lattices is occupied by the anions (e.g. Se) the other one by the cations (e.g. Zn) of the zincblende lattice.

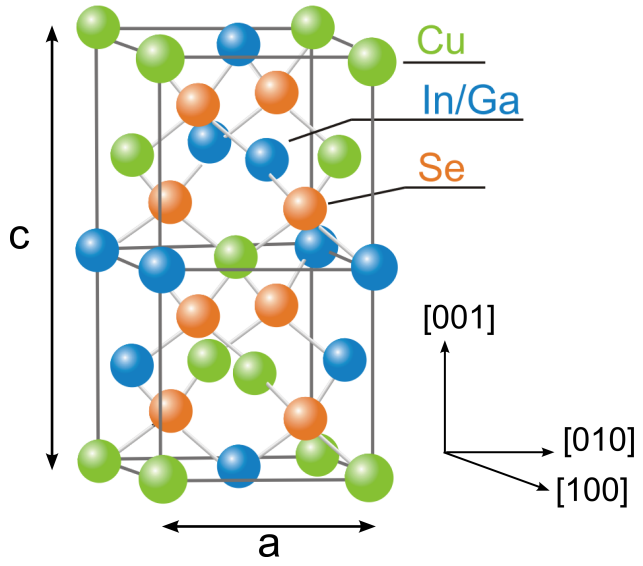

Figure 2.2: *Unit cell of Cu(In,Ga)Se$_2$ [Sha75]*

As a result of this displacement, the long edge c of the chalcopyrite unit cell is in general not exactly two times the lattice constant a: $c \neq 2a$.

By local density approximation (LDA) to density functional theory, Zhang et al. [Zhan98] have calculated a lattice constant of $a = 5.768$ and a tetragonal distortion of $\eta = \frac{c}{2a} = 1.008$, which means that the c axis is slightly stretched. Experimental results support this values. By X-ray diffraction, a value of $\eta = 1.006$ was found [Rab98].

The chalcopyrite structure forms in a wide range of temperatures and compositions. Figure 2.3 shows the phase diagram along the quasi-binary cut In_2Se_3-Cu_2Se. The chalcopyrite phase is denoted with α, the β-phase is the ordered defect compound $CuIn_5Se_8$ that can be explained by a periodical arrangement of one $(2V_{Cu} - In_{Cu})$ defect complex every 4 unit cells of $CuInSe_2$ [Zhan98] (see also Sec. 2.2.2). The diagram shows that it is possible to grow $CuInSe_2$ with a copper deficit, while providing a copper excess will lead to the formation of Cu_2Se in addition to the chalcopyrite phase. Already at a Cu content below the $CuInSe_2$ stoichiometry, the Cu_2Se phase begins to form. Hence, single phase $CuInSe_2$ can not be grown with copper excess and even stoichiometric $CuInSe_2$always contains a large number of copper vacancies V_{Cu}.

However, it can be assumed that providing more Cu during crystal growth not only leads to more Cu_2Se but also reduces the density of V_{Cu}. This does not visibly change the stoichiometry but indeed can influence the electronic properties.

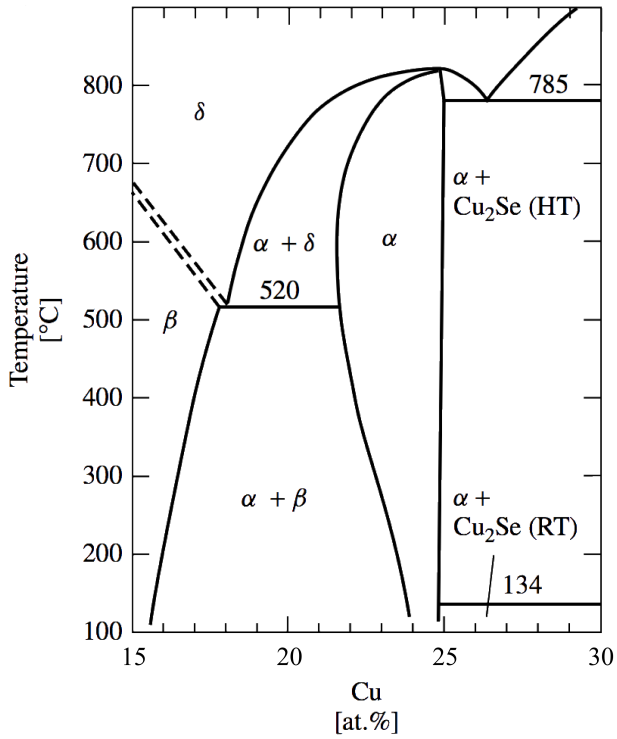

Figure 2.3: *Phase diagram of the Cu-In-Se system along the quasi-binary cut In_2Se_3-Cu_2Se. α: chalcopyrite; δ: zincblende; β: ODC (ordered defect compound, $CuIn_5Se_8$). For Cu_2Se, the authors distinguish between the high temperature (HT) and the room temperature (RT) phase [God00].*

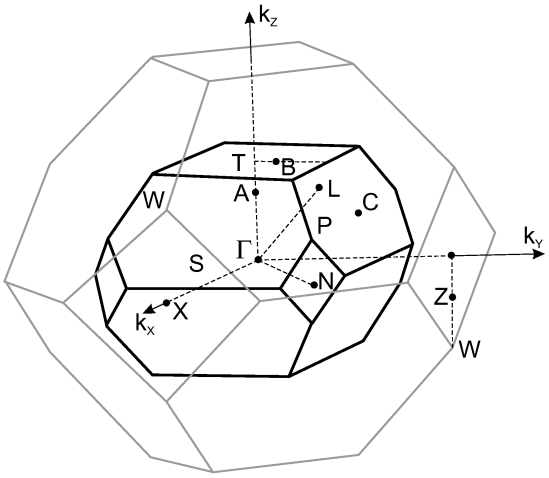

Figure 2.4: *Brillouin zone of chalcopyrite (black lines) and zincblende (grey lines) [Sha75].*

The theoretically calculated electronic band structure of $CuInSe_2$ is shown in Figure 2.5, comparing results from LDA and self consistent Coulomb hole plus screened exchange (sc-COHSEX) calculations followed by a perturbative GW (One-Particle Green Function with

Screened Coulomb Interaction) approach [Agu11]. The dispersion of the bands is very similar in both approaches, but the LDA calculations underestimate the band gap significantly, while the scGW approach comes to a correct band gap around 1 eV for $CuInSe_2$.

Valence band maximum (VBM) and conduction band minimum (CBM) are located at the Γ-point, the point of highest symmetry. The Γ-point is also the centre of the Brillouin zone that is shown in Figure 2.4. The end points of the k-axis in the band diagram are labelled T and N. T is the intersection point of k_z-axis and the outer surface of the Brillouin zone, N is the surface point in [011] direction. The band diagram shows a second valley in the conduction band at the N-point with a relatively high barrier of 0.74 eV to the CBM. This valley can give rise to a second electron contribution to the transport with the values of the effective mass and mobility different from the electrons at the Γ-point.

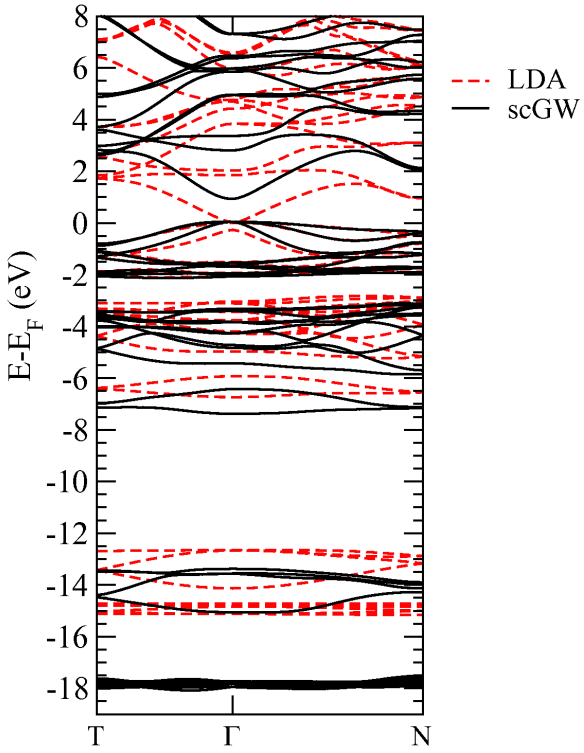

Figure 2.5: *Electronic band structure of $CuInSe_2$[Agu11]. The black solid lines give the results obtained with a self consistent GW approach. For comparison, the band structure derived with LDA is given in red dashed lines. The scGW results deliver the correct band gap, while the LDA calculations underestimate it. The structure inside the conduction and valence band is similar for both approaches.*

With Equation (2.4), the effective carrier mass m^* can be calculated from the band curvature. The effective mass tensor for chalcopyrites is anisotropic and has different values for transport along ($m^{\parallel}$) and perpendicular($m^{\perp}$) to the c-axis [Per08]. Table 2.1 compares results for the electron mass m_{c1} and the lightest hole mass m_{v1} at the Γ point and theoretical values for the electron mass m_N at the N-point in $CuInSe_2$. The values $m^{\parallel}$ and $m^{\perp}$ represent the effective mass exactly at the Γ point, because they are calculated

from the curvature at the extremal point. For a filled band (i.e. with carriers not only at the extremal point), they would only be valid in the case of parabolic bands, which is not the case for chalcopyrites. This explains the large difference to the experimental hole mass from [Bod82].

Source	Method	$m_{v1}^{\perp}$	$m_{v1}^{\parallel}$	m_v^{exp}	$m_{c1}^{\perp}$	$m_{c1}^{\parallel}$	m_c^{exp}	m_N
[Per08]	LDA	0.14	0.66		0.08	0.09		
[Bot12]	LDA				0.08	0.09		0.23
[Bot12]	scGW				0.08	0.12		0.16
[Bod82]	optical measurements			0.71			0.092	
[Wei77]	Faraday rotation						0.09	
[Aru92]	Shubnikov-de Haas oscill.						0.077	

Table 2.1: *Effective masses for $CuInSe_2$.*

2.2.2 Native Defects

The doping of the absorber in chalcopyrite solar cells is mainly done by native defects. In the ternary $CuInSe_2$ crystal, twelve different native point defects are possible. For $CuInSe_2$, these are: Three vacancies (V_{Cu}, V_{In}, V_{Se}), six antisites (In_{Cu}, Se_{Cu}, Cu_{In}, Se_{In}, Cu_{Se}, In_{Se}) and three interstitials (Cu_i, In_i, Se_i).

In addition to the point defects, there can also occur defect complexes (2 or more neighbouring point defects). Examples are the ($2V_{Cu} - In_{Cu}$) defect complex whose periodic occurrence is responsible for the formation of ordered defect compounds like $CuIn_5Se_8$, $CuIn_3Se_5$, $Cu_2In_4Se_7$, and $Cu_3In_5Se_9$ [Zhan98] or the metastable $V_{Se} - V_{Cu}$ divacancy which can act as donor or acceptor depending on its charge state [Lan06].

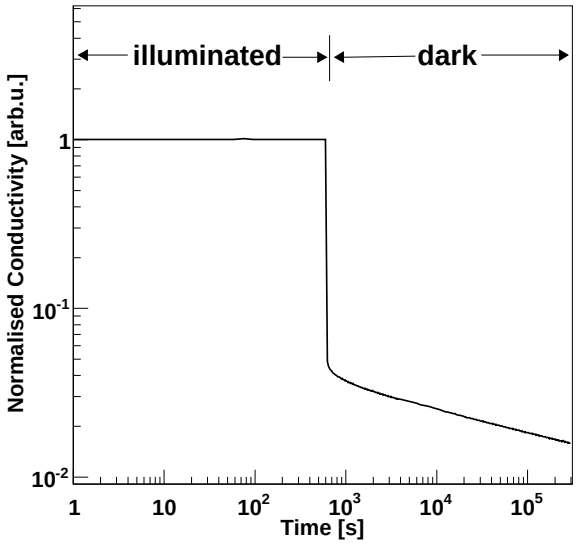

Figure 2.6: *Persistent photoconductivity observed in a p-type $CuInSe_2$sample.*

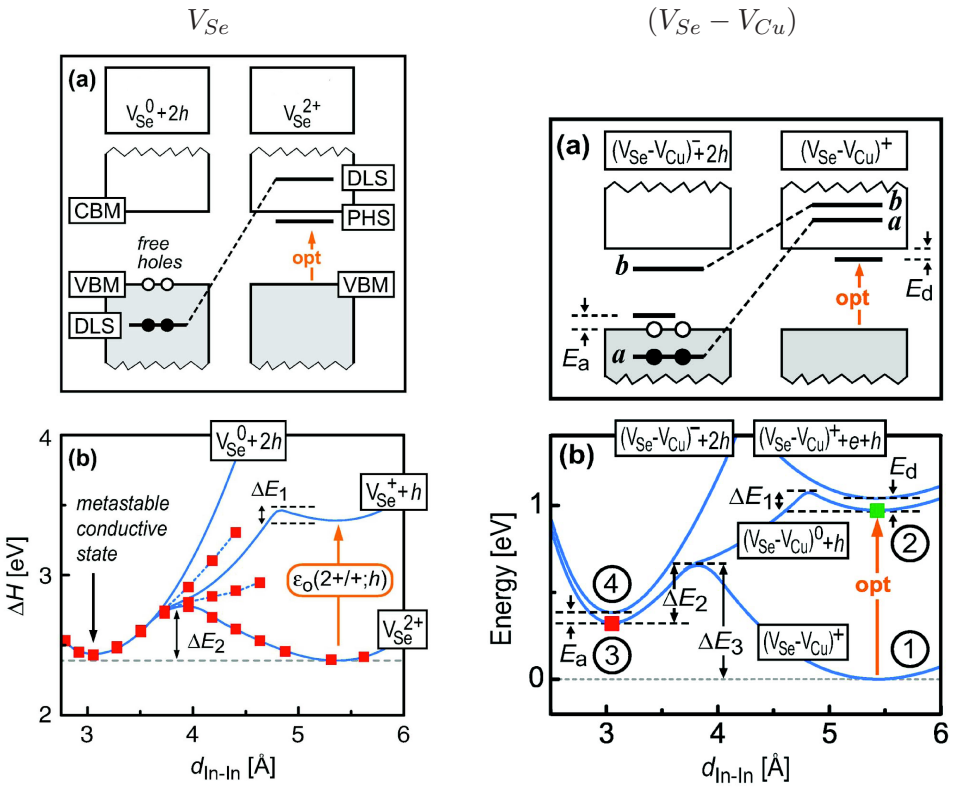

Figure 2.7: *Energy diagrams for V_{Se} [Lan05] and $(V_{Se} - V_{Cu})$ [Lan06] in $CuInSe_2$. (a) Position of the energy levels in the bands. (b) Energies of the different charge states. DLS: Defect localised state, PHS: Perturbed host state.*

Formation enthalpies depend on the Fermi level [Zhan98], which leads to a self compensation of chalcopyrite semiconductors. In general one can say that acceptor states form easier in n-type material while donors form easier in p-type material [Zhan98].

An example is the acceptor V_{Cu}. A shift of E_F up towards the conduction band decreases its formation energy $\Delta H_{V_{Cu}}$ until it reaches negative values. Any attempt to shift E_F further up would strongly increase the number of V_{Cu}. The increase of acceptor states would lead to a counteracting shift down towards the valence band. Hence, E_F will be pinned to the point where $\Delta H_{V_{Cu}}$ becomes negative.

For $CuGaSe_2$ the pinning energy lies below midgap and thus it cannot be doped n-type, while for $CuInSe_2$ it is closer to the conduction band, so that $CuInSe_2$ can be produced both p- and n-type [Zhao04].

Metastable defects that can act as acceptors and donors depending on their charge state, are possibly responsible for the effect of persistent photoconductivity. The conductivity of a semiconductor is increased under illumination due to photo induced electron hole pairs. It has been observed for chalcopyrites that it can take very long time after removing the light source until the conductivity decreases back to its original value. Figure 2.6 shows this behaviour for the $CuInSe_2$ sample p6 measured within this work (see Appx. A). The time the sample needs to relax to its equilibrium state is more than 10^5 s (several days).

An explanation can be the behaviour of the selenium vacancy V_{Se} [Lan05] and the $(V_{Se} - V_{Cu})$ divacancy [Lan06]. Figure 2.7 shows the energies of the different charge states depending on the bond length of the neighbouring In atoms. The energy levels a and b correspond to the bonding and antibonding In-In states respectively.

The equilibrium state of the Se vacancy in p-type $CuInSe_2$ is the positively charged V_{Se}^{2+} state. By capturing a photo induced electron, the defect reaches the V_{Se}^{+} state from where it only needs the relatively small energy of $\Delta E_1 \approx 0.1\,\text{eV}$ to overcome the barrier towards the metastable state. In the metastable state, the energy of the V_{Se}^{+} state is the same as for the V_{Se}^{0} state, so the defect can easily capture a second electron and thus provide in total two free holes. To relax from the V_{Se}^{0} state to equilibrium, two holes have to couple to the defect at the same time. The low probability of this event can possibly explain the long relaxation times observed for $CuInSe_2$ after illumination.

The $(V_{Se} - V_{Cu})$ divacancy behaves similar. In the metastable state, the energies of the neutral and the positively charged state are different. Thus, a shallow acceptor with the transition energy is created in the band gap.

The numerous possibilities of electrically active defects allow to produce chalcopyrites in a wide range of doping and charge carrier densities. Controlling the doping densities by adjusting the composition therefore is a crucial challenge in the production of chalcopyrite solar cells.

2.2.3 Effect of Composition on Electronic Properties

Different studies have been made to observe the dependence of electrical properties on the composition of $CuInSe_2$. It has been found that even small changes in the composition can have a large influence on the doping density and thus on the electronic properties of chalcopyrite. This becomes obvious by comparing the density of atoms with the typical doping densities: The density of copper atoms in $CuInSe_2$ is of the order of $10^{22}\,\text{cm}^{-3}$. If one now takes away 10^{17} copper atoms per cm^3, the composition will not visibly change, but the copper vacancies can create shallow acceptor states with a density of $10^{17}\,\text{cm}^{-3}$.

Experimental studies lead to results that make it possible to estimate the conduction type of $CuInSe_2$ from the composition. The different samples are grouped with help of the following parameters:

$$\Delta m = \frac{[Cu]}{[In]} - 1 \qquad \Delta s = \frac{2[Se]}{[Cu] + 3[In]} - 1 \qquad \Delta s' = \frac{[Se]}{[Cu] + [In]} - 1 \tag{2.60}$$

Table 2.2 shows results for vacuum deposited polycrystalline thin films [Nou84] and bulk single crystals grown with the Bridgman method [Neu90]. Both studies agree that material which is both copper and selenium rich is p-type. For both copper and selenium poor material, both studies find n-type conduction, Noufi et al. [Nou84] see also p-type layers. However, the p-type $CuInSe_2$ in that group shows high resistivity. This may result from a high density of compensating donors, so that one can assume that those layers are almost intrinsic and thus close to n-type conduction.

The differences in the other groups (copper rich and selenium poor; copper poor and selenium rich) partly result from the different definitions of Δs and $\Delta s'$. For example if one applies the definition of $\Delta s'$ for selenium excess or deficiency to the data of [Neu90] one finds both p- and n-type crystals in case of copper rich and selenium poor material.

	$\Delta s' < 0$	$\Delta s' > 0$
$\Delta m < 0$	p/n	p/n
$\Delta m > 0$	p	p

(a) Thin films [Nou84]

	$\Delta s < 0$	$\Delta s > 0$
$\Delta m < 0$	n	/
$\Delta m > 0$	n	p

(b) Bulk single crystals [Neu90]

Table 2.2: *Conduction type of $CuInSe_2$ polycrystalline thin films [Nou84] and bulk single crystals [Neu90] depending on the composition. The data from [Neu90] shown in this table only takes samples close to stoichiometry into account ($|\Delta m| < 0.08$ and $|\Delta s| < 0.06$). Within this range, no sample that was both copper poor ($\Delta m < 0$) and selenium rich ($\Delta s > 0$) was found. For samples with larger deviations from stoichiometry, [Neu90] found n-typ samples in this region as well as p-type samples in the copper rich and selenium poor region.*

An other reason for differences certainly are the different fabrication methods and structures of the samples in the different studies. In polycrystalline films, defects can accumulate at the grain boundaries and hence will not influence the bulk charge carrier statistics.

Summarising, one can say that the studies provide rules of thumb for the fabrication of $CuInSe_2$ with the desired properties, but in practise, the relationship between composition and electrical properties is rather complex. There is a strong interplay between defect densities, carrier densities, Fermi level, and defect formation enthalpies. For example it has been shown by first principle theoretical calculations, that the defect formation enthalpies change with the composition so that for different compositions different defects are more likely to form [Zhan98].

2.2.4 Experimentally Determined Transport and Doping Properties

In the following, a short overview on the properties of n-type and p-type $CuInSe_2$ determined by Hall measurements is given.

n-type $CuInSe_2$

$CuInSe_2$ bulk single crystals and epitaxial thin films with n-type conductivity were found with a wide range of electrical properties (see Tab. 2.3). The room temperature electron densities cover the range of $1.8 \cdot 10^{15}\, cm^{-3}$ to $1.8 \cdot 10^{20}\, cm^{-3}$.

The donor activation energies were summarised by Wasim [Was86] who identified from the measurements known to that date three different donor levels: $E_{d1} \approx 10\,\text{meV}$ dominating at temperatures below 250 K, $E_{d2} \approx 80\,\text{meV}$ dominating at $250\,\text{K} \lesssim T \lesssim 400\,\text{K}$ and $E_{d3} \approx 180\,\text{meV}$ dominating at $T \gtrsim 400\,\text{K}$.

Electron mobilities at room temperature were found in a range from $6\,\frac{\text{cm}^2}{\text{Vs}}$ to $900\,\frac{\text{cm}^2}{\text{Vs}}$. This can be explained by the domination of different scattering mechanisms limiting the mobility. The mobilities resulting from the different mechanisms can be calculated with the equations given in Section 2.1.5. Polar optical phonon scattering limits the mobility to $\mu_{PO;300K} \approx 10^3\,\frac{\text{cm}^2}{\text{Vs}}$ at room temperature. For samples with low charged defect densities, this is the lowest partial mobility and thus defines the actual total mobility. At high defect densities the limits resulting from defect scattering dominate, so that the total mobility

Source	n_{300K} [cm^{-3}]	μ_{300K} [cm^2/Vs]	E_d [meV]	Type
[Mig75]	$1 \cdot 10^{17}$	250		bulk cryst.
[Neu78]	$2.6 \cdot 10^{15} - 3.1 \cdot 10^{17}$	53 − 360	220	bulk cryst.
[Schum78]	$1 \cdot 10^{17} - 5 \cdot 10^{17}$	100	10	epi. films
[Irie79]	$1 \cdot 10^{16}$	900	12, 180	bulk cryst.
[Schum81]	$3.7 \cdot 10^{18} - 1.8 \cdot 10^{20}$	6 − 140		epi. films
[Was84]	$5.0 \cdot 10^{16} - 7.0 \cdot 10^{16}$	200 − 300		bulk cryst.
[Neu90]	$1.8 \cdot 10^{15} - 5.0 \cdot 10^{17}$	90 − 900	0 - 18	bulk cryst.
[Rin95]	$2.3 \cdot 10^{16} - 6.5 \cdot 10^{16}$		14 - 18	bulk cryst.

Table 2.3: *Experimentally measured properties of n-type $CuInSe_2$-Samples.*

decreases. With a charged defect density of 10^{19} cm^{-3} for example the mobility resulting from Brooks Herring scattering is $\mu_{BH;300K} \approx 100 \frac{\text{cm}^2}{\text{Vs}}$.

Typically, the electron mobility increases with temperature at low temperatures indicating a domination of scattering on charged impurities, until it reaches a maximum at $200 - 300$ K and decreases again towards higher temperatures, which is a sign for dominating phonon scattering .

p-type $CuInSe_2$

The room temperature hole densities of p-type $CuInSe_2$ cover a similar range as the electron densities in n-type crystals. Values between $1.2 \cdot 10^{16}$ cm^{-3} and $3.1 \cdot 10^{19}$ cm^{-3} were found.

The acceptor activation energies were summarised by Wasim [Was86] to be in the following ranges: $E_{a1} \approx 12 - 30$ meV , $E_{a2} \approx 65 - 98$ meV, and $E_{a3} \approx 400$ meV.

Source	p_{300K} [cm^{-3}]	μ_{300K} [cm^2/Vs]	E_a [meV]	Type
[Mig75]	$1 \cdot 10^{18}$	10		bulk cryst.
[Schum78]	$1.2 \cdot 10^{16} - 2.4 \cdot 10^{17}$	45 − 200	92, 400	epi. films
[Irie79]	$1.7 \cdot 10^{16} - 9.3 \cdot 10^{16}$	8 − 18	20 - 28	bulk cryst.
[Neu79]	$5 \cdot 10^{17}$	5	12	bulk cryst.
[Schum81]	$2.1 \cdot 10^{19} - 3.1 \cdot 10^{19}$	18 − 25	8, 105	epi. films
[Neu90]	$1.5 \cdot 10^{16} - 2.0 \cdot 10^{17}$	15 − 150	20 - 29	bulk cryst.
[Cham07]	$1.2 \cdot 10^{16} - 7.1 \cdot 10^{17}$	9 − 20		bulk cryst.

Table 2.4: *Experimentally measured properties of p-type $CuInSe_2$-Samples*

The observed hole mobilities are below the electron mobilities as expected due to the higher effective mass. Values between 5 $\frac{\text{cm}^2}{\text{Vs}}$ and 200 $\frac{\text{cm}^2}{\text{Vs}}$ were found at room temperature. Most samples show the same temperature dependency as described above for the n-type samples, but some authors found the mobility to be exclusively phonon dominated [Neu90] even at low temperatures.

2.3 Photon Absorption and Transmission in $CuInSe_2$

The transmission T of light through a material with thickness l can be described by the Beer-Lambert law:

$$T = \frac{I}{I_0} = e^{-\alpha(\lambda) \cdot l} \tag{2.61}$$

$\alpha(\lambda)$ is the wavelength dependent absorption coefficient. After [Sche11] it can be calculated from the semi-empirical expression

$$\alpha = \alpha_0 \sqrt{\frac{h\nu - E_G}{k_B T}} + \alpha_1 \exp\left(\frac{h\nu - E_1}{B_1}\right). \tag{2.62}$$

The parameters for $CuInSe_2$ and $CuGaSe_2$ were determined by [Org04] from fits to Equation (2.62) and are given in Table 2.5.

	α_0 [10^4 cm^{-1}]	E_g [eV]	α_1 [10^3 cm^{-1}]	B_1 [eV]	E_1 [eV]
$CuInSe_2$	0.89	1.025	6.01	0.363	1.574
$CuGaSe_2$	0.84	1.738	3.59	0.357	1.765

Table 2.5: *Parameters for calculation of the absorption coefficient α with Equation (2.62) [Org04].*

Chapter 3

Methods of the Hall Effect

3.1 The Hall Effect

The Hall effect was discovered and first described by Edwin Hall in 1879 [Hal1879] and today is a standard tool for characterisation of electrical transport properties. Basic equations used in this chapter can e.g. be found in [Put60].

In an electrical conductor through which an electric current I_x is flowing and which is situated in a magnetic field B_z perpendicular to the current, a voltage U_H perpendicular to B-field and current will be induced. This voltage depends on the used current and B-Field, on the shape of the sample and the material dependent Hall coefficient R_H which contains information on charge carrier densities and mobilities.

For a block-shaped sample with thickness d in direction of the B-Field, R_H can be expressed as follows:

$$R_H = \frac{E_y}{j_x B_z} = \frac{U_H d}{I_x B_z} \tag{3.1}$$

and thus can be directly calculated from the measured Hall voltage U_H.

3.1.1 Single Band Transport

In the following, the Hall coefficient for a p-type semiconductor with the transport exclusively in one band shall be calculated. We take the current densities j_x and j_y from the conductivity tensor (2.48) and (2.45):

$$j_x = \frac{\sigma_p}{1+\gamma_p^2} E_x + \frac{\sigma_p \gamma_p}{1+\gamma_p^2} E_y \tag{3.2}$$

$$j_y = \frac{-\sigma_p \gamma_p}{1+\gamma_p^2} E_x + \frac{\sigma_p}{1+\gamma_p^2} E_y \tag{3.3}$$

During a Hall measurement, the current density j_y in y-direction is zero.

$$j_y = 0 \tag{3.4}$$

$$\Rightarrow \sigma_p E_y = \sigma_p \gamma_p E_x \tag{3.5}$$

$$\Rightarrow E_y = \gamma_p E_x \tag{3.6}$$

Now, the Hall coefficient can be calculated:

$$R_H = \frac{E_y}{j_x B_z} \tag{3.7}$$

$$= \frac{\gamma_p E_x}{B \cdot (\frac{\sigma_p}{1+\gamma_p^2} E_x + \frac{\sigma_p \gamma_p}{1+\gamma_p^2} \gamma_p E_x)} \tag{3.8}$$

$$= \frac{\gamma_p (1+\gamma_p^2)}{B\sigma_p + \sigma_p \gamma_p^2} = \frac{\gamma_p}{B\sigma_p} \tag{3.9}$$

$$= \frac{\mu_p B}{pe\mu_p B} = \frac{1}{pe} \tag{3.10}$$

A similar derivation delivers for a n-type semiconductor

$$R_H = \frac{-1}{ne} \tag{3.11}$$

Thus in the case of one band conduction, R_H is proportional to the inverse of the charge carrier density and is independent of the magnetic field.

3.1.2 Two Band Transport

If both electrons and holes contribute to the conduction, the conductivity tensor is the sum of the individual tensors (2.47) and (2.48):

$$\underline{\sigma} = \underline{\sigma_n} + \underline{\sigma_p} = \begin{pmatrix} \frac{\sigma_n}{1+\gamma_n^2} + \frac{\sigma_p}{1+\gamma_p^2} & \frac{-\sigma_n \gamma_n}{1+\gamma_n^2} + \frac{\sigma_p \gamma_p}{1+\gamma_p^2} \\ \frac{\sigma_n \gamma_n}{1+\gamma_n^2} + \frac{-\sigma_p \gamma_p}{1+\gamma_p^2} & \frac{\sigma_n}{1+\gamma_n^2} + \frac{\sigma_p}{1+\gamma_p^2} \end{pmatrix} =: \begin{pmatrix} \sigma_{xx} & \sigma_{xy} \\ -\sigma_{xy} & \sigma_{xx} \end{pmatrix} \tag{3.12}$$

The current densities are:

$$j_x = \sigma_{xx} E_x + \sigma_{xy} E_y \tag{3.13}$$

$$j_y = -\sigma_{xy} E_x + \sigma_{xx} E_y \tag{3.14}$$

Again, we set $j_y = 0$, which leads to an expression for the y-component of the electric field E_y.

$$E_y = \sigma_{xy} \sigma_{xx}^{-1} E_x \tag{3.15}$$

Now, the Hall coefficient for two-band conduction with electrons and holes is

$$R_H = \frac{E_y}{B j_x} = \frac{\sigma_{xy} \sigma_{xx}^{-1} E_x}{B[\sigma_{xx} E_x + \sigma_{xy}(\sigma_{xy} \sigma_{xx}^{-1} E_x)]} \tag{3.16}$$

$$= \frac{\sigma_{xy}}{B\sigma_{xx}(\sigma_{xx} + \sigma_{xy}^2 \sigma_{xx}^{-1})} \tag{3.17}$$

$$= \frac{\sigma_{xy}}{B(\sigma_{xx}^2 + \sigma_{xy}^2)} \tag{3.18}$$

In the case of low magnetic fields ($\gamma = \mu B \ll 1$), the quadratic terms γ^2 in σ_{xx} and σ_{xy} can be neglected.

$$\sigma_{xx} = \frac{\sigma_n}{1+\gamma_n^2} + \frac{\sigma_p}{1+\gamma_p^2} \tag{3.19}$$

$$= \sigma_n + \sigma_p \tag{3.20}$$

$$\sigma_{xy} = \frac{-\sigma_n \gamma_n}{1+\gamma_n^2} + \frac{\sigma_p \gamma_p}{1+\gamma_p^2} \tag{3.21}$$

$$= -\sigma_n \gamma_n + \sigma_p \gamma_p \tag{3.22}$$

Thus with (3.18) and (2.46) the Hall coefficient can be written as

$$R_H = \frac{\sigma_{xy}}{B(\sigma_{xx}^2 + \sigma_{xy}^2)} \tag{3.23}$$

$$= \frac{-\sigma_n\gamma_n + \sigma_p\gamma_p}{B((\sigma_n + \sigma_p)^2 + (-\sigma_n\gamma_n + \sigma_p\gamma_p)^2)} \tag{3.24}$$

$$\overset{(2.46)}{=} \frac{pe\mu_p^2 B - ne\mu_n^2 B}{B((ne\mu_n + pe\mu_p)^2 + (pe\mu_p^2 B - ne\mu_n^2 B)^2)} \tag{3.25}$$

The second term in the denominator depends on the square of μB and thus can also be neglected for $\mu B \ll 1$ so that one finally receives for R_H in the weak B-field approximation:

$$R_H = \frac{p\mu_p^2 - n\mu_n^2}{e(p\mu_p + n\mu_n)^2} \tag{3.26}$$

Similarly, the Hall coefficient can be expressed in case of impurity band conduction:

$$R_H = \frac{p\mu_p^2 - p_d\mu_d^2}{e(p\mu_p + p_d\mu_d)^2} \tag{3.27}$$

p_d is the charge carrier density in the impurity states and μ_d the corresponding mobility.

The calculations above are made under the assumption of an energy and scattering process independent relaxation time τ (see sec. 2.1.4). To take the energy dependence into account, the Hall factor r is introduced, which is defined as the ratio between the ensemble average value of the relaxation time $\overline{\tau^2}$ and the square of the average relaxation time $\overline{\tau}^2$ of a particular carrier.

$$r = \frac{\overline{\tau^2}}{\overline{\tau}^2} \tag{3.28}$$

The Hall coefficient is then

$$R_H = r_p\frac{1}{pe} \qquad \text{p-type} \tag{3.29}$$

$$R_H = r_n\frac{-1}{ne} \qquad \text{n-type} \tag{3.30}$$

$$R_H = \frac{r_p p\mu_p^2 - r_n n\mu_n^2}{e(p\mu_p + n\mu_n)^2} \qquad \text{two band in weak field approximation} \tag{3.31}$$

Values of r are in the range between 1.18 for phonon scattering and 1.93 for scattering on charged defects [Sze81]. As the actual value of the Hall factor for a particular sample depends on the ratio of contributions of the different scattering mechanisms and also can depend on the temperature, it is difficult to determine. Therefore the Hall factor is set to $r = 1$ in the following. Thus, the charge carrier density will be slightly underestimated, while the mobility will be slightly overestimated.

The B-field dependence of R_H can immediately be seen in a non linear B-field dependence of the Hall voltage U_H. Figure 3.1 shows the room temperature B-field dependence of U_H for the $CuInSe_2$ sample p1B (see chapters 7 and 6) in the dark and under illumination respectively. The Voltages U_1 to U_8 are the voltages given in Table 4.2, the offset voltage U_{offset} results from deviations of the sample from the ideal square shape, asymmetric contacts, differences in the contact resistances and possible inhomogeneities of the layer.

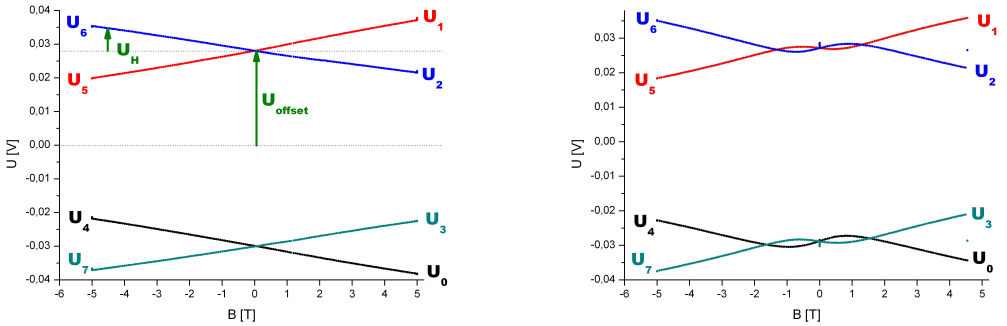

(a) (b)

Figure 3.1: *B-field dependence of the Hall voltage U_H at 300 K for the p-type $CuInSe_2$ sample p1B (a) in the dark (b) under illumination. Under illumination, the voltage does not depend linearly on the voltage so that the Hall coefficient depends on the B-field.*

For p-type semiconductors special consideration has to be given to electrons that are induced in the sample for example by illumination or thermal energy: Due to the in general higher mobility of the electrons, they might significantly contribute to the conduction, although the hole density still is much higher than the electron density.

A certain number of light induced electron-hole-pairs will increase the carrier densities by $n_{photo} = p_{photo}$. As those concentrations remain constant while temperature changes and the defect induced hole density decreases at low temperatures, a p-type semiconductor under illumination will always seem to switch to n-type conduction at sufficiently low temperatures. As the type of a semiconductor depends on the Fermi level which by itself only depends on the carrier densities and not on the mobilities, this means that a semiconductor can seem to be n-type in Hall measurements while in fact being p-type.

A special case is a semiconductor with an equal number of free holes and electrons. This situation occurs on one hand at very high temperatures, when thermal band to band excitation delivers significantly more carriers than excitation to or from defect states, and on the other hand at very low temperatures under illumination, when the defect induced free carriers freeze out and thus light induced band to band excitation is the dominating source of free carriers. With $p \approx n$ and $x = \mu_p/\mu_n$, the weak field approximation of the Hall coefficient for two band conduction (3.26) can be written as

$$R_H = \frac{x^2 - 1}{e \cdot n \cdot (x+1)^2} = \frac{x - 1}{e \cdot n \cdot (x+1)} = R_{H,1Band} \cdot \frac{x-1}{x+1}, \tag{3.32}$$

with $R_{H,1Band}$ the Hall coefficient for one band conduction (eq. (3.10)). Herewith, the error caused by neglecting the hole contribution can easily be calculated if the ratio x of the mobilities is known.

3.1.3 Multiple Band Transport

In principle, the conductivity tensor and Hall coefficient can be calculated for any number of contributing carriers. However, because of the large number of free parameters, an analytical approach only makes sense, if some of the parameters (i.e. mobilities and carrier

densities) are known. If this is not the case, it makes more sense to use a numerical method that determines the number and parameters of the contributing carriers directly from the measured data. This is done by the mobility spectrum analysis that is introduced in section 3.2.

3.1.4 The van der Pauw Method

For the determination of the conductivity of thin film samples of arbitrary geometry, the van der Pauw method [Pau58] is used. Four electrical contacts are needed for connecting the current source and voltmeter to the film. The following requirements on the sample geometry arise from the derivation of van der Pauw's equation:

- The thickness of the sample has to be homogeneous and small compared to the distance of the four contacts.
- The sample has to be simply connected, which means, that there are no holes or highly conductive areas.
- The four contacts have to be placed at the edge of the sample.
- The size of the contacts has to be small compared to the size of the sample.

To prove the correctness of van der Pauw's equation, we start with a particular geometry: a semi infinite half plane with four contacts P, Q, R and S at its boundary (Fig. 3.2) and a current entering at the contact P and leaving at the contact Q.

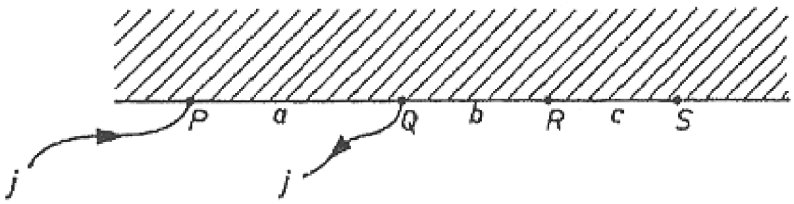

Figure 3.2: *Sample in form of half plane with four contacts [Pau58].*

For a homogeneous and simply connected layer, the lines of equal potential – referring to a current entering or leaving at a particular point – are half circles with radius r around this point. Hence, the Voltage between two points C and D of this sample can be calculated as

$$U = R \cdot I = I\rho\frac{l}{A} = I\rho\int_{r(C)}^{r(D)}\frac{dr}{\pi r d}, \tag{3.33}$$

with ρ the specific resistivity of the sample, l the length of the path of the current, A the cross section along the path, and d the thickness of the sample. Thus, we can determine the voltage between contacts R and S resulting from the current entering the sample at P to be

$$U_{P,RS} = V_{P,S} - V_{P,R} = \frac{\rho I}{\pi d}\int_{a+b+c}^{a+b}\frac{dr}{r} = \frac{\rho I}{\pi d}\ln\left(\frac{a+b}{a+b+c}\right) \tag{3.34}$$

And analogue for the current leaving at contact Q

$$U_{Q,RS} = V_{Q,S} - V_{Q,R} = \frac{\rho I}{\pi d} \int_b^{b+c} \frac{dr}{r} = \frac{\rho I}{\pi d} \ln\left(\frac{b+c}{b}\right) \tag{3.35}$$

The total Voltage between R and S is the sum of the two partial voltages (3.34) and (3.35):

$$V_S - V_R = \frac{\rho I}{\pi d} \ln \frac{(a+b)(b+c)}{b(a+b+c)} \tag{3.36}$$

$$\Rightarrow \quad R_{PQ,RS} = \frac{\rho}{\pi d} \ln \frac{(a+b)(b+c)}{b(a+b+c)} \tag{3.37}$$

In the same way, $R_{QR,SP}$ can be derived:

$$R_{QR,SP} = \frac{\rho}{\pi d} \ln \frac{(a+b)(b+c)}{ca} \tag{3.38}$$

With

$$b(a+b+c) + ca = (b+a)(b+c) \tag{3.39}$$

(3.37) and (3.38) lead to the van der Pauw-Equation:

$$e^{-\frac{\pi d}{\rho} R_{PQ,RS}} + e^{-\frac{\pi d}{\rho} R_{QR,SP}} = 1 \tag{3.40}$$

By the use of conformal mapping it is possible to map a semi infinite half plane to any shape that is simply connected. As $\frac{d}{\rho} R_{PQ,RS}$ and $\frac{d}{\rho} R_{QR,SP}$ are invariant under conformal transformations, equation (3.40) is of general validity for any sample holding the constraints given above (page 27).

For $R_{PQ,RS} = R_{QR,SP} := R$, (3.40) can be readily solved to:

$$\rho = \frac{\pi d}{\ln 2} R \tag{3.41}$$

For $R_{PQ,RS} \neq R_{QR,SP}$ one takes the arithmetic mean and multiplies by a correction factor $f\left(\frac{R_{PQ,RS}}{R_{QR,SP}}\right)$:

$$\rho = \frac{\pi d}{\ln 2} \frac{(R_{PQ,RS} + R_{QR,SP})}{2} f\left(\frac{R_{PQ,RS}}{R_{QR,SP}}\right), \tag{3.42}$$

The correction factor can only be determined numerically. In [Pau58], one can find the plot shown in Fig.3.3 and the following approximation:

$$f \approx 1 - \left(\frac{R_{PQ,RS} - R_{QR,SP}}{R_{PQ,RS} + R_{QR,SP}}\right)^2 \frac{\ln 2}{2} - \left(\frac{R_{PQ,RS} - R_{QR,SP}}{R_{PQ,RS} + R_{QR,SP}}\right)^4 \left\{\frac{\ln 2^2}{4} - \frac{\ln 2^3}{12}\right\} \tag{3.43}$$

For $\frac{R_{PQ,RS}}{R_{QR,SP}} < 2$, the correction factor can be shown to be less than 5%.

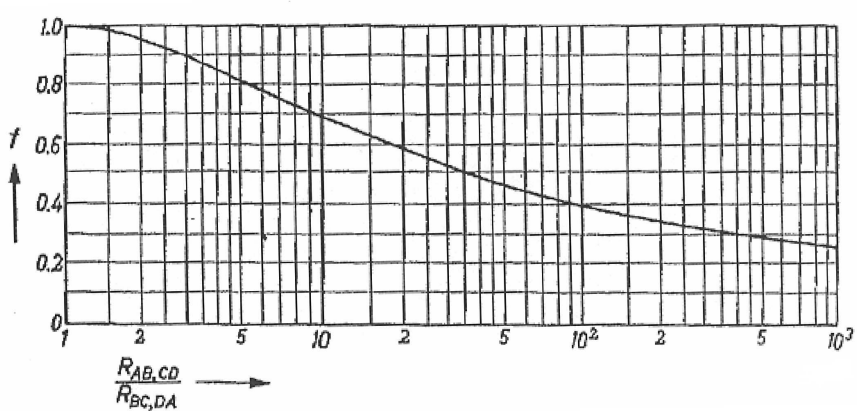

Figure 3.3: *The correction factor for the calculation of the specific resistancy ρ, dependent on the ratio $\frac{R_{PQ,RS}}{R_{QR,SP}}$.* [Pau58]

3.2 Mobility Spectrum Analysis

3.2.1 Background

As mentioned above, charge transport in a semiconductor with an arbitrary number of contributing charge carriers can in principle be described by summation of the partial conductivity tensors σ_{xx_i} and σ_{xy_i}.

$$\sigma_{xx_i}(B) = \frac{en_i\mu_i}{1+(\mu_i B)^2} \tag{3.44a}$$

$$\sigma_{xy_i}(B) = \frac{en_i\mu_i^2 B}{1+(\mu_i B)^2} \tag{3.44b}$$

Conductivity $\sigma(B)$ and Hall coefficient $R_H(B)$ can then directly be calculated:

$$\rho(B) = \frac{1}{\sigma(B)} = \frac{\sigma_{xx}}{\sigma_{xx}^2+\sigma_{xy}^2} \tag{3.45a}$$

$$R_H(B) = \frac{\sigma_{xy}}{B(\sigma_{xx}^2+\sigma_{xy}^2)} \tag{3.45b}$$

Those expressions become quite long for more than two carriers and moreover it is necessary to know the number of carriers in order to model a dataset correctly. The mobility spectrum analysis (MSA) describes the elements of the conductivity tensor as integrals over a continuous mobility spectrum $s(\mu)$ [Beck87] which is similar to a summation over an infinite number of contributing carriers. Equations (3.44) are then written as follows:

$$\sigma_{xx}(B) = \int_{-\infty}^{\infty} \frac{s(\mu)d\mu}{1+(\mu B)^2} \tag{3.46a}$$

$$\sigma_{xy}(B) = \int_{-\infty}^{\infty} \frac{\mu B s(\mu)d\mu}{1+(\mu B)^2} \tag{3.46b}$$

The validity of equations (3.46) is shown in Appendix D.

In practise, measurements reveal R_H and $\sigma = \frac{1}{\rho}$. In order to obtain the elements of the conductivity tensor, equations (3.45) have to be converted to:

$$\sigma_{xx}(B) = \frac{\rho}{\rho^2 + B^2 R_H^2} \tag{3.47a}$$

$$\sigma_{xy}(B) = \frac{-BR_H}{\rho^2 + B^2 R_H^2} \tag{3.47b}$$

With the resulting σ_{xx} and σ_{xy}, a mobility spectrum has to be found to solve Equations (3.46). This is done by numerical algorithms. For a numerical solution, however, the number of considered mobilities has to be reduced to a finite but large number.

There are different software packages available. In this work, the MEMSA[1] software is used. It was developed at the CEA Grenoble [Rot06], based on work done at the University of Warwick [Kia02]. Alternatively there are a commercial software using an algorithm named iQMSA[2] provided by Lakeshore [Vur98] and the HR-QMSA[3] algorithm recently developed at the University of Western Australia [Uma10].

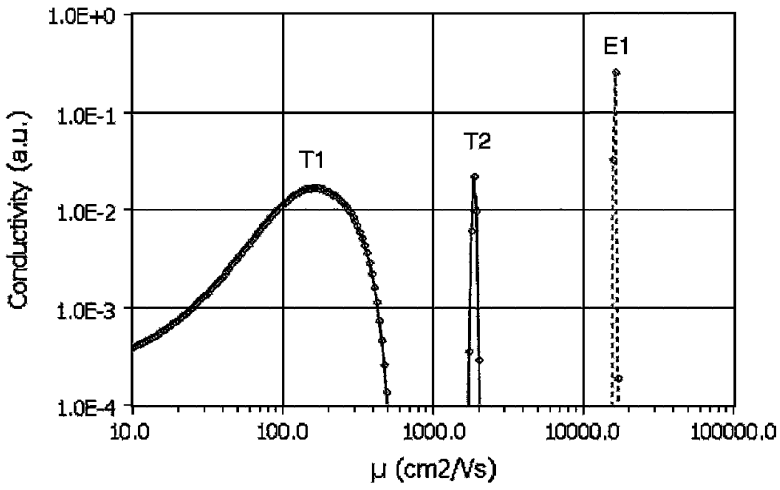

Figure 3.4: *Mobility spectrum of HgCdTe determined with the MEMSA algorithm [Rot06]. The holes are labelled T1 and T2, the electron E1.*

The advantage of the MSA approach is that no previous assumptions about the carriers have to be put into the algorithm. The solution of (3.46) will lead to a mobility spectrum $s(\mu)$ in which every carrier corresponds to a peak at a certain position on the mobility axis. The contribution of the charge carrier to the overall conductivity is determined by integrating over the peak.

Figure 3.4 shows an example of a mobility spectrum of HgCdTe determined with the MEMSA algorithm [Rot06]. Two hole peaks and one electron peak can be seen.

Effects like energy dependent relaxation times τ or non parabolic bands are implicitly considered and are expressed in the mobility peak shapes. Thus, the sometimes difficult

[1]Maximum Entropy Mobility Spectrum Analysis
[2]Improved Quantitative Mobility Spectrum Analysis
[3]High-Resolution Quantitative Mobility Spectrum Analysis

interpretation of those effects does not have to be done before the determination of the spectrum.

For this work, only the MEMSA software was used, but a representative dataset from sample p1B (see chap. 6) was sent to Lakeshore [Cie09] to be analysed with the iQMSA algorithm. The results from either approach are similar.

3.2.2 Interpretation of the Results

A first evaluation of the fit quality can be done by the threshold that is needed for convergence. This threshold allows to deal for example with noisy data.

Noisy data can lead to ghost peaks that do not originate from real effects but from fluctuations in the data. In the best case, the ghost peaks have neglectable contributions or occur at positions that can be excluded. A high mobility hole peak with a mobility far above all relevant scattering mechanisms can easily be identified as a ghost peak. A way to detect ghost peaks is to compare different datasets of the same sample under the same or – in case the ghost peak might results from systematic errors – slightly different conditions. For example it can be tried to follow the temperature dependence of a peak.

An other phenomenon are so called mirror peaks. Mirror peaks are peaks at the position of a real peak but with the opposite sign. Studies about the appearance in HgCdTe suggest that mirror peaks appear preferred for samples with larger contacts [Rot06], thus ignoring the requirements on the sample geometry for van der Pauw measurements (see Sec. 3.1.4). However, Rothmnn et al. [Rot06] found that the occurrence of a low mobility electron peak did not depend on the contact size, but could be attributed to the magnetic freezeout[4].

Important for the reliability of the quantitative results is also the covered magnetic field range. Especially for low mobility carriers, the high magnetic field data is very important [Rot10], because for low mobilities and low fields, it is more likely that the $\mu B \ll 1$ which cancels the B-field dependence of R_H. While other studies used maximum magnetic fields of up to 9 T [Rot06], the magnet used for this work can reach a maximum field of 5 T (see Sec. 4.2).

3.3 Photoluminescence

The samples were cooled to 10 K and illuminated by an argon ion laser (wavelength $\lambda = 514\,\text{nm}$). The emitted photoluminescence spectrum represents the transitions from and to the different defect levels and band edges [Pan75, Yu10]. For $CuInSe_2$, four different transition energies are observed at low temperatures: Three resulting from donor-acceptor transitions at 0.991 eV (DA1), 0.971 eV (DA2) and 0.945 eV (DA3) and one excitonic transition.

The spectra gives information on the copper excess or deficit during layer growth. By comparison to EDX[5] measurements, it has been found that the copper to indium ratio can be estimated by the ratio between the intensities of the DA1 and the DA2 transition [Reg04]. Photoluminescence spectra of very copper rich samples are dominated by the DA2

[4] Reduction of the carrier density with increasing B-field. This effect is caused by an increasing activation energy due to localisation of the impurity states.

[5] Energy Dispersive X-Ray Spectroscopy

transition, with decreasing copper content, the DA1 peak becomes stronger and dominates near stoichiometric growth conditions. For samples grown under copper poor conditions the DA1 peak broadens and becomes asymmetric.

As in most cases, layers grown under Copper rich[6] conditions are p-type while those grown under Copper poor conditions are n-type, this gives a first estimation of the conductivity type.

[6]Copper poor/rich describes the conditions during growth. The layer itself will never be Cu rich because all excess Copper will start to form Copper Selenides ($CuSe_x$) on top of the layer [God00].

Chapter 4

Equipment

4.1 Sample Preparation

4.1.1 Production by MOVPE

The epitaxial layers analysed in this work were produced by Metal Organic Vapour Phase Epitaxy (MOVPE) [Str99, Lar11]. Metal organic compounds of the elements are transported with an inert gas (e.g. N_2 or H_2) to a heated single crystalline Gallium Arsenide substrate. At the surface of the substrate, the metal organic compounds decompose due to the heat and the desired element stays at the substrate. The stoichiometry of the deposited material can be changed by controlling the partial pressures of any compound. Under the correct conditions [1], the atoms start to form a single crystal by adopting lattice constant and orientation of the substrate. Thus, the deposited layer starts to grow in a strained state[2]. When the thickness exceeds a certain critical thickness d_c, the layer relaxes by forming misfit dislocations and continues to grow with its own lattice constant. The critical thickness is approximately $d_c \approx 50\,\text{nm}$ for $CuInSe_2$ [Reg04].

All epitaxial layers analysed in this work were grown on Gallium Arsenide which has a lattice missmatch of $\approx 2\,\%$ to $CuInSe_2$. Both doped and undoped (semi insulating) wafers can be used for epitaxial growth. While for the production of solar cells with epitaxial absorbers it is necessary to use doped substrates to have a conducting back contact, measurements of the electrical properties require highly resistive undoped wafers to avoid any contribution from the conduction inside the GaAs substrate.

4.1.2 Preparation for van der Pauw Measurements

The samples for van der Pauw and Hall measurements were cut into squares of approximately 5 mm edge length. To remove Cu_xSe which forms on top of the epitaxial layer under Copper rich growth conditions, the samples were etched for 5 minutes[3] in a 5% solution of KCN.

[1] temperature, stoichiometry: see e.g. phase diagram fig. 2.3

[2] This will lead to a certain strain inside the deposited layer depending on the lattice mismatch. Due to the large difference between growth temperature and room temperature, different thermal expansions coefficients of layer and substrate also play a role.

[3] Early samples were etched for only 2 minutes.

For electrical measurements it is necessary to produce ohmic contacts to the layer. This was done by depositing a layer of $\approx 200\,\mathrm{nm}$ of Gold to the corners of the samples. For Copper rich samples, the resulting contacts were reliable ohmic over the whole temperature range for most samples, while for Copper poor samples the situation was more complex: In General, contacts were ohmic at room temperature, but for some samples they turned out to be not ohmic at lower temperatures (e.g. 250 K).

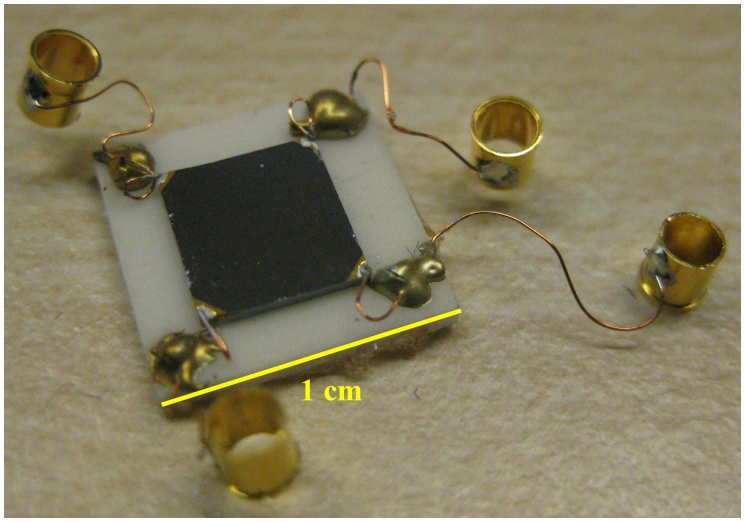

Figure 4.1: *A typical sample glued onto an Al_2O_3-plate.*

Figure 4.1 shows a $CuInSe_2$ sample ready to be mounted onto the sample holder of the Hall cryostat. The samples were glued to a small Al_2O_3 plate of 1 cm x 1 cm. Copper wires were glued to the contacts on the samples with conductive silver paint, to reduce forces to this bonding point, the wires were additionally glued to the corners of the Al_2O_3. The other end of the copper wires was soldered to small sleeves that can be plugged to the contacts of the sample holder so that a change of samples is easily possible.

4.2 Hall System

4.2.1 Hardware

The cryostat used for the Hall measurements is an Oxford Instruments Microstat®MO. The superconducting solenoid magnet can reach a magnetic field of 5 T below 6 K and is cooled by a continuous flow of liquid helium. A small amount of liquid helium stays in the core of the magnet to keep the temperature stable. A second branch of the helium cycle passes the heat exchanger of the sample chamber and in combination with a heater allows to control the sample temperature. Each of the helium cycle branches ends at a gas flow controller so that the helium flows of every cycle can be adjusted independently.

The sample temperature sensor is located in a metal block on which the sample holder is screwed, while the sample itself is kept in vacuum. Sample temperatures of 10 K to 300 K are possible. The low temperature range is limited by the ability of the temperature control to deliver a stable temperature, the high temperature region is limited by indium seals used inside the cryostat.

Two windows at the top and at the bottom of the sample vacuum chamber permit optical access to the sample. For illumination, a 100 W halogen lamp is used. Under illumination, the heat deposition in the sample leads to a slight temperature rise (see Sec. 4.2.5) due to the spatial distance between sample and temperature sensor.

The helium comes from a dewar containing 250 l of liquid helium, allowing three to four days of measurements at high magnetic field. The helium is pushed through the cryostat by a tunable overpressure inside the dewar, usually in the range between 0.2 and 0.6 bar. For lower pressures, the helium flow through the magnet core will not reach a sufficiently high value (20 l/min to 30 l/min of gas) for a high magnetic field at high sample temperature. Increasing the pressure does on one hand increase the possible flow rate, but on the other hand also increases the liquid helium temperature. Anyway, high fields can still be reached at the maximum overpressure of 1.5 bar although the resulting total pressure of 2.5 bar exceeds the critical pressure[4] of helium.

For electrical measurements there are twelve channels to the sample holder out of which four are used for the Hall measurements. As power supply, a Keithley 6220 was used, currents and voltages were measured by a Keithley 6485 picoammeter and a Keithley 2010 multimeter. The communication between sample, instruments, and PC was done by a Keithley 7001 switch system in combination with the Keithley Hall effect card 7065.

4.2.2 Software

The software was written at the University of Luxembourg. All hardware parts except the halogen lamp can be controlled via the software. Thus, remote control is possible, which is very important for runs with durations of 12-24 h.

The largest part of the data was taken in standard procedures that were defined for temperature dependent and magnetic field dependent runs. In the following, those procedures are described with the standard parameters. Virtually all parameters could be adjusted to the special needs of the actual sample or the status of the setup.

Data Acquisition: Temperature Dependent Runs

The standard procedure is to measure downwards from room temperature (300 K) to 150 K in steps of 10 K. After every change of temperature or B-field, the software waits 300 s to let the sample find an equilibrium state. The Hall voltage is measured first with a positive B-field at 300 K, then the resistivity is measured at $B = 0$ T and finally the negative field Hall voltage is taken. In order to reduce the time for magnet ramping, the measurements starts alternating with positive and negative field respectively at the different temperatures.

Data Acquisition: B-field Dependent Runs

For B-field dependent runs, two different procedures were used:

To save the time needed for magnet ramping, the positive fields were measured first, starting with 5 T and then decreasing to 0 T and afterwards continuing with increasing negative fields. This procedure is only suitable for highly relaxed and stable samples as between the positive and negative field measurements at high B-fields there can easily be a

[4] Critical point of ^{4}He: 2.27 bar, 5.19 K

time difference of 10 h or more. To check if the electrical properties of the sample remained stable, the run was started end ended with resistivity measurements at 0 T.

The alternative procedure started with high fields and for every B-field value the data at positive and negative field was taken successively. In between, a resistivity measurement was performed at 0 T. Similarly to the temperature dependent measurements, one point starts with positive, the next one with negative field. The 0 T resistivity data for every point makes it possible to detect changes of the sample and to correct the B-dependent resistivity values if necessary.

4.2.3 Calculation of the Resistivity

The resistivity is determined with the van der Pauw Method (see Chapter 3.1.4). To achieve higher reliability of the results and having a way to detect possible non ohmic contacts or inhomogenities of the sample, all possible combinations of current paths and voltages were measured. An overview is given in Table 4.1.

Name	I	U
R_0	$1 \to 2$	$3 \leftrightarrow 4$
R_1	$2 \to 1$	$3 \leftrightarrow 4$
R_2	$2 \to 3$	$4 \leftrightarrow 1$
R_3	$3 \to 2$	$4 \leftrightarrow 1$
R_4	$3 \to 4$	$1 \leftrightarrow 2$
R_5	$4 \to 3$	$1 \leftrightarrow 2$
R_6	$4 \to 1$	$2 \leftrightarrow 3$
R_7	$1 \to 4$	$2 \leftrightarrow 3$

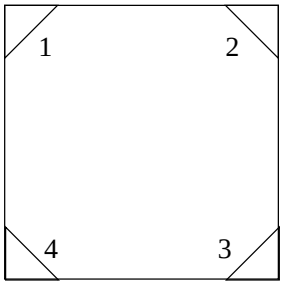

Table 4.1: *Combinations of current and voltage measurements necessary for the van der Pauw method. Each line states the contacts through which the current was applied and the contacts at which the voltage was measured. The sketch on the right side shows the numbering of the contacts.*

The calculation of the resistivity is done in two different ways:

- Mean: Two pseudo-resistivities r_a and r_b are calculated as follows:

$$r_a = R_0 - R_1 + R_5 - R_4 \tag{4.1}$$

$$r_b = R_3 - R_2 + R_7 - R_6 \tag{4.2}$$

  They correspond to $R_{PQ,RS}$ and $R_{QR,SP}$ respectively (see Chapter 3.1.4). Under the assumption of a homogeneous and symmetric sample, all measured resistivities should have the same value and the calculation can be done with equation 3.41, using the arithmetic mean: $R = \frac{r_a + r_b}{2}$.

- Numerically: r_a and r_b are calculated in the same way as for the "mean"-algorithm, but the sample is no longer expected to be symmetric and the calculation of ρ is done by a numerical solution of equation (3.40).

Thus, for homogeneous and symmetrical samples, it is sufficient to take the mean resistivity, while the numerically calculated value should be the more precise one if $r_a \neq r_b$.

4.2.4 Calculation of the Hall Coefficient

For the determination of the Hall coefficient, the Hall voltages U_i given in table 4.2 are measured.

Name	I	U	Contributions	B
U_0	$3 \to 1$	$4 \leftrightarrow 2$	$U_{\mathrm{HC}} + U_{\mathrm{offsetC}}$	+
U_1	$1 \to 3$	$4 \leftrightarrow 2$	$-U_{\mathrm{HC}} - U_{\mathrm{offsetC}}$	+
U_2	$4 \to 2$	$1 \leftrightarrow 3$	$U_{\mathrm{HD}} + U_{\mathrm{offsetD}}$	+
U_3	$2 \to 4$	$1 \leftrightarrow 3$	$-U_{\mathrm{HD}} - U_{\mathrm{offsetD}}$	+
U_4	$3 \to 1$	$4 \leftrightarrow 2$	$-U_{\mathrm{HC}} + U_{\mathrm{offsetC}}$	−
U_5	$1 \to 3$	$4 \leftrightarrow 2$	$U_{\mathrm{HC}} - U_{\mathrm{offsetC}}$	−
U_6	$4 \to 2$	$1 \leftrightarrow 3$	$-U_{\mathrm{HD}} + U_{\mathrm{offsetD}}$	−
U_7	$2 \to 4$	$1 \leftrightarrow 3$	$U_{\mathrm{HD}} - U_{\mathrm{offsetC}}$	−

Table 4.2: *Resistivities measured for Hall coefficient. The numbering of the contacts is depicted in the sketch in Table 4.1.*

The Hall coefficient can be calculated for two possible configurations:

$$R_{HC} = \frac{d}{B}\frac{1}{4}\left(\frac{U_1}{I_1} - \frac{U_0}{I_0} + \frac{U_4}{I_4} - \frac{U_5}{I_5}\right) \tag{4.3}$$

$$R_{HD} = \frac{d}{B}\frac{1}{4}\left(\frac{U_3}{I_3} - \frac{U_2}{I_2} + \frac{U_6}{I_6} - \frac{U_7}{I_7}\right) \tag{4.4}$$

By calculating R_H this way, offset voltages resulting for example from asymmetries are cancelled out, while the Hall voltages are summed up 4 times.

4.2.5 Sample Temperature

The sample holder temperature sensor is not located directly at the sample, but in a metal block on which the sample holder is screwed. This leads to a delayed temperature adjustment at the sample and to possible temperature differences between sensor and sample. Especially under illumination with a halogen lamp, the temperature of the sample rises as there is a direct source of heat to the sample. To measure those effects, tests with a PT100 temperature sensor were performed. The PID controller allows a certain overshoot when reaching the new temperature so that the maximum value of the first overshoot for temperature and PT100 resistance respectively can be taken as a measure for the delay[5].

First, the PT100 was glued directly on the sample holder. In this configuration, the delay between the overshoots, was 2 s to 8 s and the temperature increased by $0.75\,(\pm 0.25)\,\mathrm{K}$ under illumination.

Then the PT100 was glued onto a Al_2O_3 plate equal to those used for the samples. The effect of illumination did not change, but the delay between the overshoots increased drastically to $23\,(\pm 5)\,\mathrm{s}$. As this value still is more than a factor of ten below the standard

[5]This will certainly underestimate the time delay for reaching the equilibrium. It was decided to take this value because the relaxation time of the sample temperature can only be determined very roughly because of the resolution of only $\Delta T = 0.1\,\mathrm{K}$. The maximum of the overshoot in contrast can usually be seen very nicely for both values.

waiting time that was used after every change of temperature, it can be argued that this delay does not affect the data.

4.2.6 Limitations of the System

As mentioned above, the maximum sample temperature is limited to 300 K. This limits the temperature interval available for measurements severely. The results discussed in chapters 6 and 7 show that interesting effects such as the start of defect depletion zone or intrinsic conduction or the transition between domination of different scattering mechanisms would be visible only at higher temperatures for some of the samples.

Another challenge are the long times needed for taking a full B- or T-dependent dataset. Especially after a change of temperature, the sample has to relax to equilibrium again requiring a waiting time of several minutes. In addition, each voltage and current data point is averaged over an adjustable number of individual measurements to be able to detect instabilities in the samples or electronics. In the standard procedures, a full data set of resistivity and hall voltages at positive and negative field needs about 1 h and thus a full run over 16 different temperatures about 16 h.

Therefore a sample has to be as relaxed and stable as possible before starting a run. The relaxation time due to persistent photoconductivity after illumination can be several days.

At low sample temperatures, the measured Hall coefficient scatter strongly. For most of the $CuInSe_2$ layers, the lowest temperature allowing a determination of R_H was between 150 K and 200 K. The main reason for this is the low conductivity of the $CuInSe_2$ layers at those temperatures. Low conductivities lead to an increasing influence of the offset voltage so that small changes in U_{offset}, e.g. caused by a still ongoing relaxation process, can surpass the Hall voltage.

4.3 Illumination of the samples

4.3.1 Charge carrier generation in the $CuInSe_2$ layer

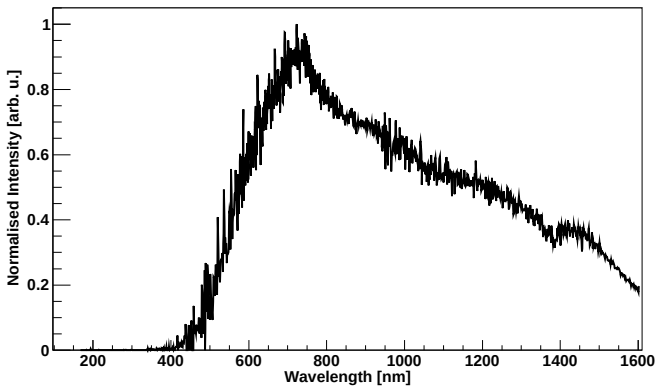

Figure 4.2: *Measured spectrum of the halogen lamp.*

For photo Hall measurements, the samples were illuminated with a 100 W halogen lamp. The lamp was placed in a distance of ≈ 50 cm to the magnet to avoid disturbances from

the magnetic field. For the determination of the photon fluxes in the relevant energy range, the spectrum was measured. Figure 4.2 shows the normalised spectrum of the lamp.

The photon flux of the lamp was estimated by comparing the short circuit current I_{SC} of a silicon reference solar cell with respect to the current I_{Sun} under illumination with an AM1.5 spectrum[6]. The ratio was $\frac{I_{SC}}{I_{Sun}} = 0.52$, so that the photon flux of the lamp above the silicon band gap is estimated to be about half of the AM1.5 photon flux. The spectrum was normalised to this value.

For the charge carrier generation, the flux of photons with energies above the band gap is important. The fluxes above the band gaps of $CuInSe_2$ (1.0 eV), GaAs (1.42 eV), and $CuGaSe_2$ (1.6 eV) and above the cutoff energy of a filter (1.77 eV) used for the measurements on $CuGaSe_2$ were derived by integrating over the spectrum and are given in Table 4.3. The table also contains the transmitted photon fluxes after the typical thickness of the $CuInSe_2$ (650 nm) and $CuGaSe_2$ (770 nm) layers described in this thesis (see Tab. A.1).

$E_{ph} >$	0 eV	1.0 eV	1.42 eV	1.6 eV	1.77 eV
Φ_0	$1.3 \cdot 10^{17}$	$6.7 \cdot 10^{16}$	$4.5 \cdot 10^{16}$	$1.7 \cdot 10^{16}$	$8.4 \cdot 10^{15}$
$\Phi_T(CuInSe_2)$	$7.4 \cdot 10^{16}$	$1.0 \cdot 10^{16}$	$1.1 \cdot 10^{15}$	$2.8 \cdot 10^{14}$	$7.3 \cdot 10^{13}$
$\Phi_T(CuGaSe_2)$	$1.2 \cdot 10^{17}$	$5.9 \cdot 10^{16}$	$2.9 \cdot 10^{16}$	$9.0 \cdot 10^{15}$	$1.2 \cdot 10^{15}$

Table 4.3: *Transmission for characteristic energies and layer thicknesses. The fluxes are integrals over the spectrum above photon energies E_{ph} for the columns respectively and are given in $cm^{-2}s^{-1}$. The transmission T can be calculated as the ratio of Φ_0 and the transmitted flux Φ_T after the corresponding layer. The energies correspond to the $CuInSe_2$ band gap, the GaAs band gap, the $CuGaSe_2$ band gap and the cutoff of the filter used for the measurements on a $CuGaSe_2$ layer in Section 7.1.*

The density n_{photo} of photo induced carriers in those layers can now be approximated by

$$n_{photo} = \frac{\Phi_0 \cdot A \cdot \tau_i}{l} \tag{4.5}$$

with A=1-T the absorption in the layer, τ_i the lifetime of the minority carriers, and l the thickness of the layer. A maximum value of $\tau_i = 18$ ns was found by time resolved photoluminescence measurements [Key03].

With $\Phi_0 \cdot A = \Phi_0 - \Phi_T$, the resulting photo induced carrier densities are $n_{CuInSe2} \approx 1.6 \cdot 10^{13}\,cm^{-3}$ and $n_{CuGaSe2} \approx 1.7 \cdot 10^{12}\,cm^{-3}$.

4.3.2 Charge carrier generation and conduction in the GaAs substrate

The epitaxial $CuInSe_2$ samples are grown on a, though undoped, semiconductor substrate. However, charge carrier diffusion or photo induced electron-hole-pair generation can lead to charge carrier transport in this substrate and diffusion of copper, indium or selenium to the GaAs could create a certain doping level.

The latter effect has been investigated at the Helmholtz Zentrum Berlin [Sie11] for the case of epitaxial growth of $CuGaSe_2$ on undoped GaAs. The subject of this study was a

[6]The AM1.5 spectrum is defined as the spectrum of the sunlight that reaches the earth after passing 1.5 times the atmosphere thickness.

GaAs substrate of which the $CuGaSe_2$ layer had peeled off. The GaAs substrate showed no change of the electrical properties.

Concerning the contribution of light induced carriers in the GaAs, the transmission of photons with energies above the GaAs band gap to the substrate was estimated above (Tab. 4.3). For 650 nm of $CuInSe_2$, the transmission is 2%. For measurements on $CuGaSe_2$, a 700 nm short pass filter was used that cuts away all photon energies below 1.77 eV. For energies above this value, the transmission after a 770 nm layer is 14%.

To make sure that the charge carriers generated by the transmitted photons in the GaAs do not disturb the transport measurements in the chalcopyrite layers, photo Hall measurements were done using a 850 nm long pass filter[7]. Thus, only photons with energies around and below the GaAs band gap were transmitted so that no band to band excitation was possible in GaAs. Comparing those measurements to measurements done with the full spectrum did not lead to significant differences of the electrical properties.

Finally, measurements on a typical undoped, 500 μm thick GaAs wafer showed a room temperature sheet conductivity of $\sigma_{\square dark} \approx 7.5 \cdot 10^{-10}\,\Omega^{-1}$ in the dark and $\sigma_{\square illum} \approx 6 \cdot 10^{-7}\,\Omega^{-1}$ under illumination (without filter). Those values are several orders of magnitude lower than the sheet resistivities of the $CuInSe_2$ and $CuGaSe_2$ layers.

[7] 850 nm= 1.459 eV, $E_G(GaAs) = 1.424$ eV. Note that there is still a small overlap, especially if one takes into account that the cutoff is not sharp.

Chapter 5

Simulations of Transport and Charge Carrier Statistics

In Section 3.1 the dependence of the Hall coefficient on the basic parameters of charge carrier statistics (carrier densities n, p), transport properties (mobilities μ_n, μ_p) and the magnetic field have been derived. Due to lack of knowledge of the type and number of contributing carriers, an apparent charge carrier density p_{app} or n_{app} is usually calculated in a first attempt after the simple relation

$$n_{app} = \frac{1}{R_H \cdot e} \tag{5.1}$$

under neglect of possibly contributing minority carriers. In case of transport in more than one band, this can lead to unexpected behaviour of n_{app}. Some examples are:

- Decreasing apparent carrier density with increasing temperature.
- Negative carrier densities – interpreted as n-type conduction – for p-type semiconductors.
- Sign changes of the Hall coefficient that lead to infinite carrier densities.

To be able to interpret those effects when they occur in the measurements, simulations of typical behaviours of Hall coefficient and apparent charge carrier densities for a compensated p-type semiconductor with one acceptor and one donor level are presented in this chapter.

Actual hole and electron densities are calculated with the numerical algorithm described in Appendix C.1 under use of the parameters given in Table 5.1. The density of the second acceptor N_{A2} is set to zero.

For Sections 5.1 and 5.2 it is assumed that the low B-field approximation

$$R_H = \frac{p\mu_p^2 - n\mu_n^2}{e(p\mu_p + n\mu_n)^2} \tag{5.2}$$

is valid, while for Section 5.3 the full expression (Eq. (3.18))

$$R_H = \frac{\sigma_{xy}}{B(\sigma_{xx}^2 + \sigma_{xy}^2)} \tag{5.3}$$

including B-field dependence is used.

The mobilities μ_p and μ_n result from the equations given in Section 2.1.5 under use of the parameters given in Table 5.1.

5.1 p-Type Semiconductor in the Dark

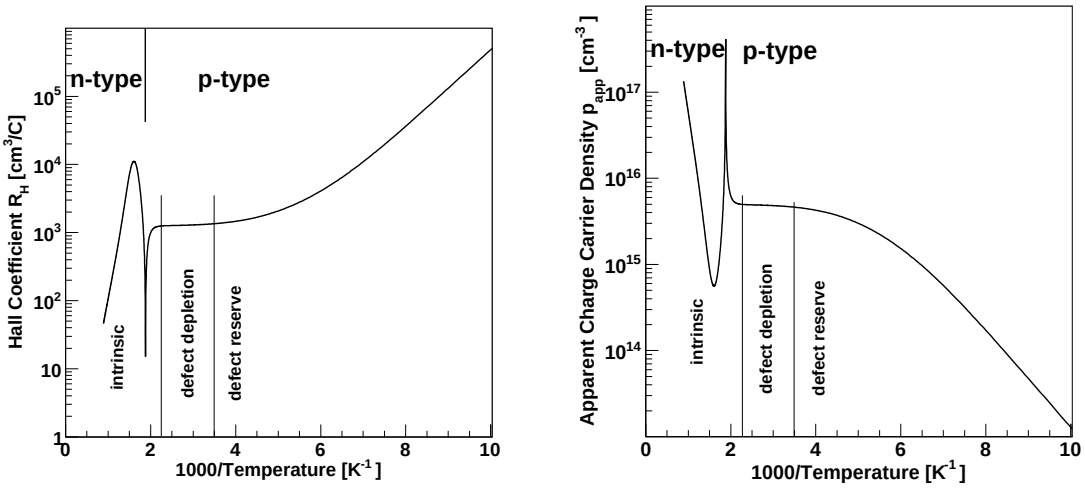

(a) (b)

Figure 5.1: *Simulated temperature dependence of (a) Hall coefficient and (b) apparent charge carrier density for a compensated p-type semiconductor. The plots show absolute values. The regions where R_H and p_{app} are negative are labelled "n-type". Fit parameters are given in Table 5.1*

For a semiconductor in the dark, the only available energy for excitation of charge carriers to the bands is the thermal energy. Two mechanisms are present in a doped semiconductor: defect to band excitation and band to band excitation. At low temperatures, defect induced excitation will be dominating because of the lower necessary energies. However, the number of defect induced charge carriers is limited by the defect density.

Excitation over the band gap takes over when the available energy increases at higher temperatures. It is limited by the effective densities of state in the valence and conduction band that grow with temperature following a $T^{3/2}$-law (see Eq. (2.9)).

The temperature dependence of Hall coefficient gives information on the dominating mechanism. Figure 5.1 shows the simulated behaviour of Hall coefficient R_H and the apparent charge carrier density p_{app}. For this simulation it is assumed that the low B-field approximation for R_H (Eq. 5.2) is valid. At low temperatures (i.e. high inverse temperatures) the temperature dependence of the charge carrier density is defined by the activation level of the defects (defect reserve) until it levels off to a constant value $N_A - N_D$ (defect depletion).

At higher temperatures, excitation over the band gap begins to have visible influence providing an equal number of free electrons and holes $p_{bb} = n_{bb}$. At sufficiently high

Charge carrier statistics:

E_G [meV]	m_e^* [m_e]	m_h^* [m_e]	E_a [meV]	N_A [cm^{-3}]	N_D [cm^{-3}]	n_{photo} [cm^{-3}]
1.0	0.09	0.7	100	$1 \cdot 10^{16}$	$5 \cdot 10^{15}$	$1 \cdot 10^{11}$

Scattering mechanisms:

E_{AC} [eV]	D [eV/cm]	Θ [K]	ϵ_r	ϵ_∞	ρ [g/cm^3]	v_s [m/s]
6.5	$6.8 \cdot 10^8$	395	13.6	8.1	5.77	$2.18 \cdot 10^3$

Table 5.1: *Parameters used for the simulations in this chapter.*

temperatures, the number of electron-hole pairs generated by the band to band excitation is much larger than the number of defect generated holes p_d so that $p = p_{bb} + p_d \approx p_{bb}$ and hence $p \approx n$.

Therefore, p-type semiconductors pass through a change to n-type conduction at high temperatures because in general electrons have higher mobility than holes because of their lower mass and thus dominate the transport if the product of electron density and square of the mobility is higher than the same product for the hole contributions $\mu_n^2 n > \mu_p^2 p$. This results immediately from Equation (5.2). The Hall coefficient crosses the zero line and thus the apparent charge carrier density forms a pole, changing the sign.

5.2 p-Type Semiconductor under Illumination

Under illumination, light induced excitation of electrons is an additional charge carrier generating effect and photo generated electron hole pairs are a second source of minority carriers in addition to thermal band to band excitation. As the absorption of photons does in first approximation not depend on the temperature, the density of photo induced charge carriers $p_{photo} = n_{photo}$ is constant for all temperatures and thus dominates the electric transport at low temperatures when the defect induced charge carriers p_d freeze out. Similar to the band to band excitation ($p_{bb} = n_{bb}$), this leads to a change of conduction type for p-type semiconductors[1], but now at low temperatures:

$$T \to 0 \Rightarrow p_{bb} = n_{bb} \to 0 \tag{5.4a}$$

$$p_d \to 0 \tag{5.4b}$$

$$\Rightarrow p = n = p_{photo} = n_{photo} \tag{5.4c}$$

Figure 5.2 shows the effect of illumination simulated by a constant density of photo induced holes and electrons being added to the free carrier concentrations, while the other parameters stay the same as in Section 5.1. Still the low B-field approximation is assumed to be valid. The photo induced carriers do not affect the high temperature (or low inverse temperature) behaviour, because there the density of defect and intrisically induced electrons are significantly higher so that photo induced carriers can be neglected.

[1] Again, it is assumed that electrons have higher mobility and thus dominate the transport if p=n.

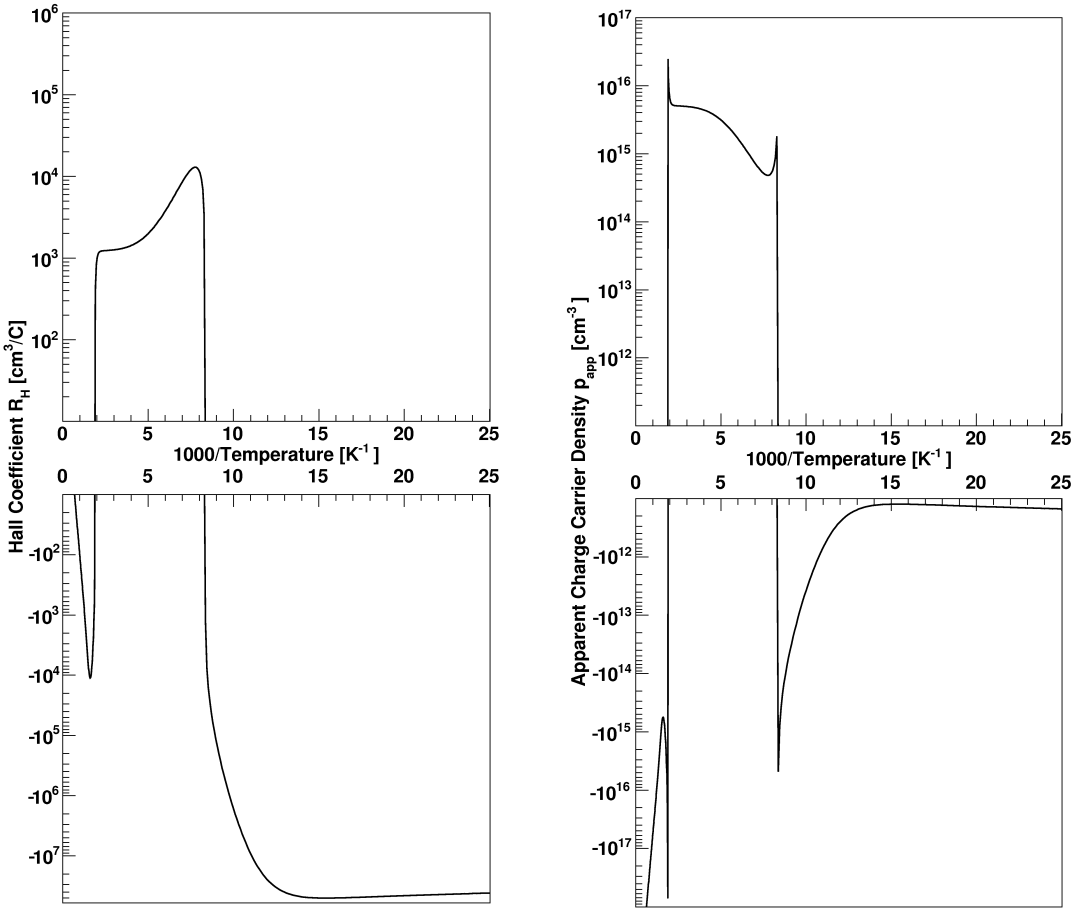

(a) (b)

Figure 5.2: *Simulated temperature dependence of Hall coefficient (a) and apparent charge carrier density (b) for a compensated p-type semiconductor under illumination. The photo induced charge carrier densities are* $n_{photo} = p_{photo} = 1 \cdot 10^{11}\ cm^{-3}$. *All other parameters are identical to Figure 5.1. In the low inverse temperature region* $(1000/T \leq 7\ K^{-1})$, *the photo induced carriers have no effect, so that* R_H *and* p_{app} *are the same as in Figure 5.1. At higher inverse temperatures the influence of electrons increases, consequently the Hall coefficient and apparent charge carrier density become negative.*

The maximum of R_H around $1000/T = 15$ results from the changes in the electron mobility. The transport is dominated by electrons due to higher mobility with respect to the holes, but the holes lower the Hall coefficient. Starting from 20 K, the electron mobility increases towards higher temperatures, while the hole mobility remains constant or even decreases. Consequently, the influence of holes to the Hall coefficient decreases and R_H increases. With growing hole density, the influence of holes increases, leading to a decreasing absolute value of the Hall coefficient and finally to the change of the sign.

The actual hole density p under illumination is shown in Figure 5.3 (a). In the intermediate temperature range ($1.5\,\mathrm{K}^{-1}$<1000/T<$15\,\mathrm{K}^{-1}$) where the defect induced holes dominate the apparent charge carrier density, p and p_{app} are equal. At lower temperatures, the photo induced holes dominate and thus the hole density stays constant at the value of

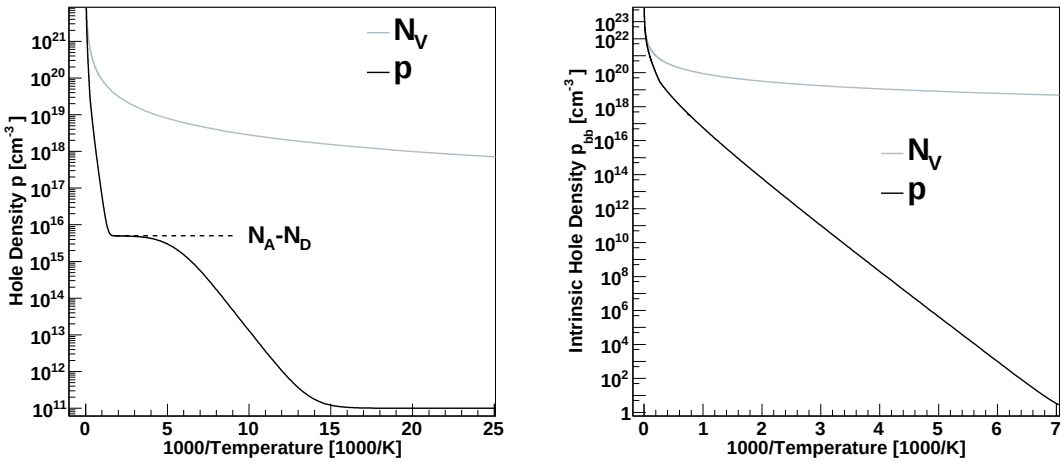

(a) (b)

Figure 5.3: *(a) Simulated actual free hole density p under illumination and density of states N_V. At low temperatures p equals the photo induced carrier density $p_{photo} = 1 \cdot 10^{11}$ cm^{-3}. In the intermediate temperature range (1.5 K^{-1}<1000/T<15 K^{-1}), p shows the regimes of defect reserve and defect depletion. In the high temperature range, the holes resulting from band to band excitation dominate the free hole density. The limitation of p by the density of states N_V is visible at the highest temperatures. (b) Simulated intrinsic hole density p_{bb} for $CuInSe_2$ ($E_G = 1.0$ eV). At 300 K, p_{bb} is in the order of 10^{10} cm^{-3}.*

$p_{photo} = 1 \cdot 10^{11}$ used for the simulation. Towards higher temperatures p approaches the density of states N_V.

The parameters for the simulation are chosen in a way that makes all effects visible starting from the regime of photo induced conduction over defect dominated conduction (defect reserve and defect depletion) to intrinsic conduction. However in the experiment it is possible that a part of the effects are not visible. For example layers with high defect activation energies do not reach the depletion zone before the onset of intrinsic conduction.

5.3 B-field Dependence of the Hall coefficient

The simulations above were all done under assumption of weak B-fields with $\mu B \ll 1$. This assumption leads to a B-field independent Hall coefficient. A typical B-field for the Hall measurements done in this work is 3 T. Hence, the mobilities must be significantly smaller than the inverse B-field of $B^{-1} \approx 3.3 \cdot 10^3\,\mathrm{cm^2(Vs)^{-1}}$ to make the low field approximation valid. Figure 5.4 shows the simulated hole and electron mobilities with the parameters given in Table 5.1. One can see that the electron mobilities are already in the order of magnitude of B^{-1} at room temperature and become even larger towards lower temperatures.

Consequently, the B-field dependence has to be taken into account by using equation (5.3).

Figure 5.5 shows simulations of the Hall coefficient and the apparent charge carrier density at different B-fields in the range from 0.1 T to 9 T. The parameters are again given

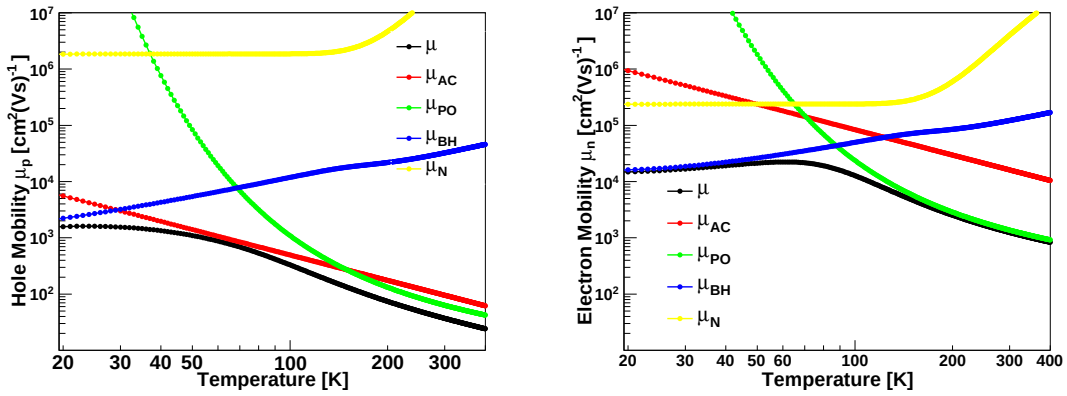

(a) (b)

Figure 5.4: *Simulated mobilities for (a) holes and (b) electrons.*

in Table 5.1. The figures show only the temperature range where a significant B-field dependence can be seen as at other temperatures the curves are identical to Figure 5.2. In Section 3.1 it has been shown that the B-field dependence disappears if one of the following two situations occurs:

- **Single Band Conduction:** Only one type of carrier is present or the domination of the majority carrier is so strong that the contribution of the minority carrier to the transport can be neglected (Sec. 3.1.1).

$$\mu_1^2 n_1 \gg \mu_2^2 n_2 \tag{5.5}$$

- **Low Magnetic Fields**: The low B-field approximation $1 + \mu^2 B^2 \approx 1$ is valid (Sec. 3.1.2).

The latter is true for the lowest B-field (0.1 T, black curves) over the whole temperature range. A comparison with the data shown in Figure 5.2 leads to the results that both curves are almost identical. The maximum electron mobility of $\mu_{n,max} = 9.2 \cdot 10^3\,\mathrm{cm}^2/\mathrm{Vs}$ at 93 K leads to a value of $\mu B = 0.092 \Rightarrow 1 + \mu^2 B^2 = 1.008 \approx 1$.

For higher B-fields, the Hall coefficient changes with the B-field in the temperature range between 60 K and 150 K. Below 60 K, transport properties are governed by the photo induced carriers because the thermal activation of the acceptor still is too weak. Hence the number of free electrons and holes is equal as was shown in Equation (5.4c). Due to the comparably high mobilities of both electrons and holes, the weak field approximation here does not hold for high B-fields. The reason why R_H anyway does not depend on the B-field is the higher mobility of the electrons leading to (Eq. (5.5)): $\mu_n^2 n \gg \mu_p^2 p$.

Around 60 K, the hole density and thus the influence of hole conduction increases to the same order of magnitude as the electron contribution, while at the same time μB stays for both carriers around or above one. Consequently, the Hall coefficient starts to change with the B-field.

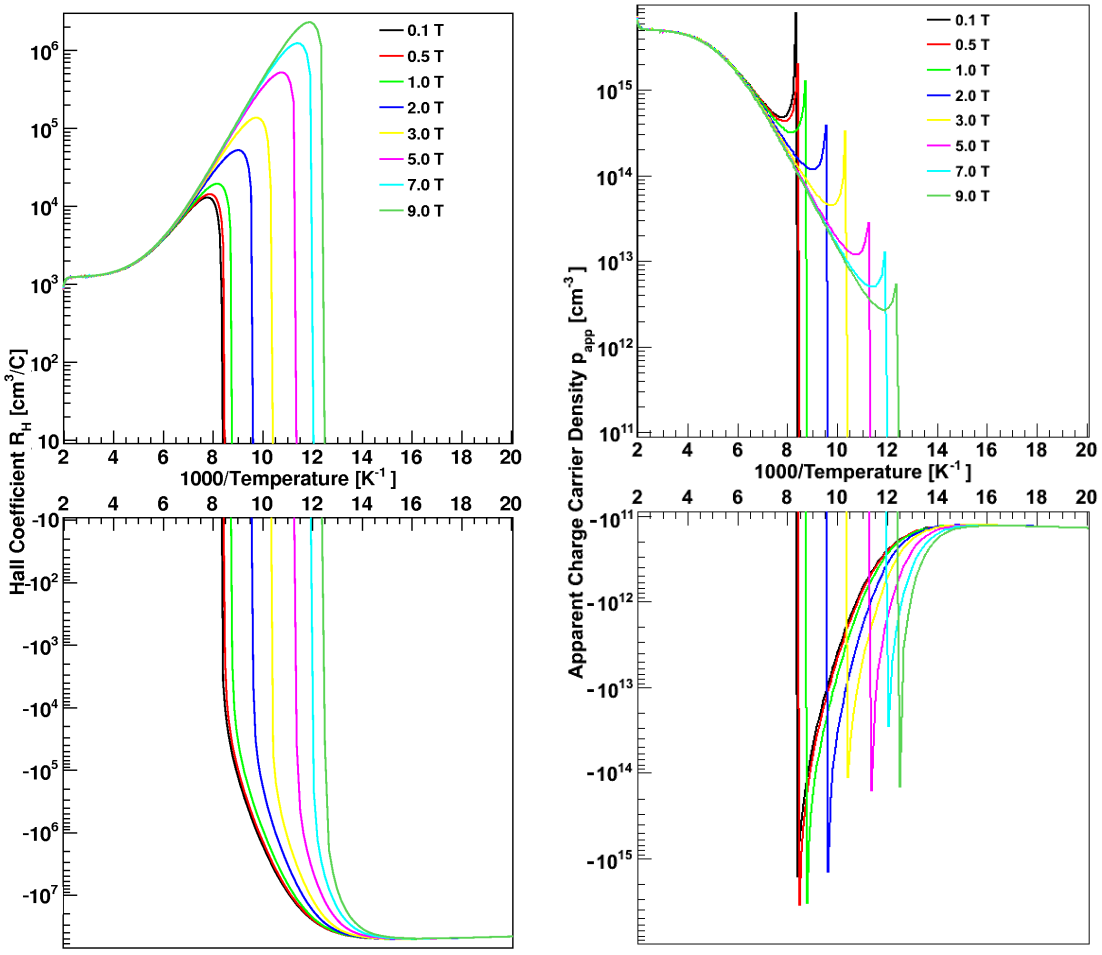

Figure 5.5: *Simulated temperature dependence (a) of Hall coefficient and (b) apparent charge carrier density for a compensated p-type semiconductor under illumination at different magnetic fields under consideration of the B-field dependence of the Hall coefficient. The parameters are the same as in Figure 5.2. At the lowest field (0.1 T, black curves), the low field approximation is still valid over the whole temperature range and hence R_H and p_{app} are identical with the values in Figure 5.2.*

Towards higher temperatures, the density of holes increases due to the acceptor and thus, hole conduction begins to dominate the transport. Around 150 K, the domination is strong enough to neglect the minority electrons. The transport can now effectively be described by one band conduction and hence, the B-field dependence disappears.

In the regime of intrinsic conduction at very high temperatures, electrons are again the dominating carriers when the density of carriers excited over the band gap becomes much larger than the defect induced hole density.

Around the onset of intrinsic conduction, one would also expect to see a B-field dependence, when the dominating carrier changes again. In the present case, this is not visible because both mobilities decrease towards higher temperatures, so that the small B-field approximation is valid.

Chapter 6

Hall Measurements in the Dark

The electric properties of all samples were first measured in the dark to determine defect induced charge carrier densities and defect activation energies.

All of the samples are epitaxially grown by MOVPE on a (100) oriented GaAs substrate. One sample, named p1B, was grown at the Helmholtz Zentrum Berlin in 2003. The other samples are grown at the University of Luxembourg in 2010 and 2011. p-type samples from Luxembourg are named p2-p7, n-type samples n1-n3. An overview over all samples can be found in Table 6.1, important properties are summarised in Appendix A. The thickness of the layers is in the order of 650 nm.

Name	Type	Remark	Chapter dark	Chapter illuminated
p1B	p	Low E_a	6.2.1	7.2
p2	p	High E_a, single band	6.2.2	7.3.1
p3	p	High E_a, single band	6.2.2	7.3.1
p4	p	High E_a, single band	6.2.2	7.3.1
p5	p	High E_a, intrinsic	6.2.2	-
p6	p	High E_a, intrinsic	6.2.2	-
p7	p	High E_a, intrinsic	6.2.2	-
n1	n	High E_a, single band	6.3	7.3.2
n2	n	High E_a, single band	6.3	7.3.2
n3	n	High E_a, single band	6.3	7.3.2
CGS	p	$CuGaSe_2$, single band	7.1	7.1

Table 6.1: *Overview of the samples described in this work.*

As discussed in Section 5.1, only thermally induced defect activation and intrinsic band to band excitation are expected to be present as source of charge carriers. The densities $n_{bb} = p_{bb}$ resulting from band to band excitation for $CuInSe_2$ are shown in Figure 5.3. Around room temperature – which is the highest sample temperature that can be achieved with the experimental setup – the intrinsic carrier density is in the order of $10^{10}\,cm^{-3}$. This value is several orders of magnitude below the expected defect induced carrier densities. Therfore it can be expected that electrical transport in the dark can be described by single band conduction.

As will be shown, this assumption is valid for the p-type samples p1B-p4 and all n-type samples, but for three of the p-type samples, p5-p7, intrinsic electrons already contribute visibly to the transport at and even below room temperature (see Figs. 6.9 and 6.11).

6.1 Estimation of the Cu/In Ratio by Optical Measurements

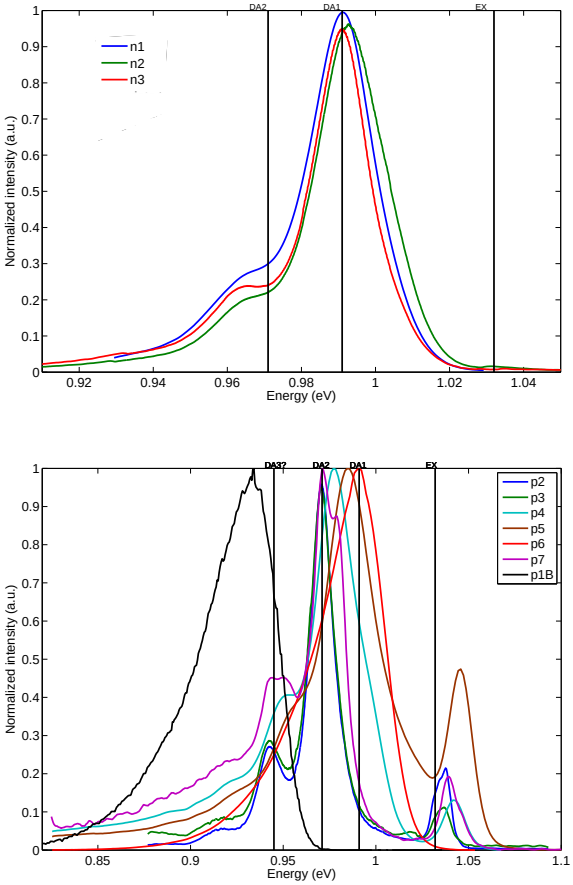

Figure 6.1: *Photoluminescence spectra of the samples described in this chapter. The intensity is given in arbitrary units. Samples n1, n2, n3 and p6 show domination of the DA1 transition which indicates growth conditions near stoichiometry. For p2 and p3, the DA2 transition is stronger so that these samples are expected to be grown under high copper excess* $\left(\frac{[Cu]}{[In]} \gtrsim 1.2\right)$*. p4 and p5 are still copper rich but shifted due to strain. Note that the range of the x-axis is larger for the p-type samples (lower plot) to avoid cutting the peaks.*

Photoluminescence spectra (see Sec. 3.3) were taken before the electrical measurements in order to determine the copper to indium ratio and thus give a first idea of the expected conduction type. In general, samples grown under copper rich conditions are rather p-type, while stoichiometric or copper poor layers often are n-type. This however, is not a general rule as discussed in Section 2.2.3. Especially under near stoichiometric growth conditions both conduction types can appear. Figure 6.1 shows the photoluminescence spectra of all samples.

The PL spectrum of the three n-type samples is dominated by the DA1 transition, indicating nearness to stoichiometric growth conditions. For the p-type samples, different shapes of the spectra occur. p2 and p3 are clearly DA2 dominated and thus are expected to be grown under very copper rich conditions ($\frac{[Cu]}{[In]} \gtrsim 1.2$), while p7 shows a small DA1 contribution, indicating less copper excess.

For the samples p4 and p5, the peak maximum shifts towards the DA1 position. As also the excitonic contribution shifts in the same direction, this can be attributed to strain in the layer, leading to a change in the band gap and thus a shift of the whole spectrum. In addition, a broadening and a small indication of a DA1 shoulder are visible which can be interpreted as signs of a decreasing copper content.

A further explanation is possible for p5: The thickness of this sample shows large fluctuations down to 200 nm as can be seen in the SEM crossection in Table A.1. Therefore, it is possible that the PL reaches the interface to the GaAs substrate or areas in which some gallium has diffused, which would increase the band gap and thus lead to a shift to higher energies.

The PL signal of sample p6 has a shape similar to the n-type samples and thus probably is grown under conditions close to stoichiometry.

The PL signal of sample p1B does not show peaks related to the DA transitions. The broad peak at an energy below the expected DA peaks probably is the deep luminescence peak [Lar11] being attributed to 2-dimensional defects in the layer.

6.2 p-type $CuInSe_2$

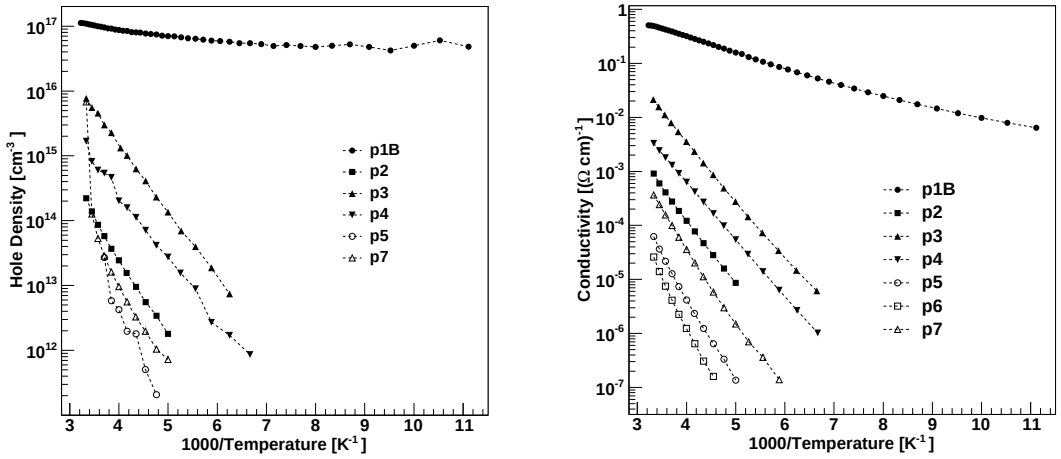

(a) (b)

Figure 6.2: *Measured temperature dependence of the hole density and conductivity of all p-type samples.*

An overview of the hole densities and conductivities of all p-type samples is shown in the arrhenius plots in Figure 6.2. Sample p1B has significantly higher carrier densities and conductivities and a shallower slope in the temperature dependence. It will therefore

be described separately in Section 6.2.1, while the other samples are discussed in Section 6.2.2.

6.2.1 Low Activation Energy

Data for sample p1B was taken in a temperature range between 90 K and 310 K. Below 140 K, the measured Hall coefficients start to scatter strongly (see sec. 4.2.6), consequently this part of the data was omitted in the analysis.

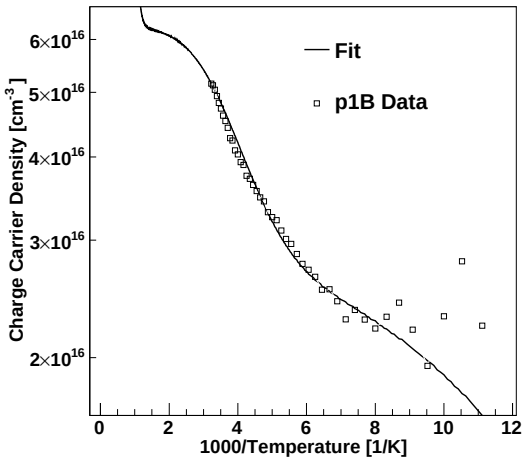

Figure 6.3: *Charge carrier density of sample p1B. The fit is done with the parameters given in Table 6.2*

As shown in Figure 6.3, the charge carrier density does not follow a simple exponential law but the slope becomes steeper towards lower inverse temperatures. This behaviour cannot be explained under the assumption of one acceptor. In case of one acceptor, one would expect the slope to decrease towards lower inverse temperatures when the activation approaches depletion as can be seen in Figure 5.1. The measured curve can be explained by a shallow acceptor dominating charge carrier statistics at low temperatures and a deeper acceptor taking over at higher temperatures.

When using the numerical solution for a semiconductor with two acceptors and one donor (Sec. 2.1.3, Appx. C.1), the data can be modelled by assuming acceptors with activation energies $E_{a1} = 110\,\text{meV}$ and $E_{a2} = 18\,\text{meV}$. The used defect densities are given in Table 6.2.

E_{a1} [meV]	N_{A1} [cm^{-3}]	E_{a2} [meV]	N_{A2} [cm^{-3}]	N_D [cm^{-3}]	$N_D/(N_{A1}+N_{A2})$
110	$3.5 \cdot 10^{16}$	18	$9.5 \cdot 10^{16}$	$6.7 \cdot 10^{16}$	0.52

Table 6.2: *Parameters for modelling the temperature dependence of the charge carrier density of sample p1B.*

The expected hole mobility can be calculated from the partial mobilities given in Section 2.1.5 with the densities of the defects taken from the numerical solution for the charge carrier density and the material parameters for scattering on phonons taken from the

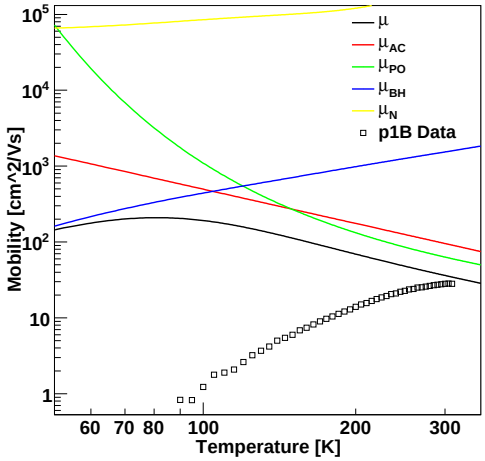

Figure 6.4: *Temperature dependence of the mobility of sample p1B. The total mobility (black line) is calculated from the partial mobilities with Matthiessen's rule. Only mechanisms expected for band conduction in epitaxial material are included for this fit. At the highest measured temperatures, the model appears to adapt to the data. The decreasing mobilities towards lower temperatures can not be explained by charged impurity scattering as the density of charged impurities is too low.*

literature (see Appx. B.3). Figure 6.4 shows the calculated and measured mobilities in dependence of the temperature.

The experimental mobilities lie significantly below the calculated. It can be expected, that the experimental data reaches a maximum at 300 K and follows the limit given by scattering on acoustical (μ_{AC}) and polar optical (μ_{PO}) phonons at higher temperatures. This can not be confirmed because measurements above room temperature were not possible due to the limitations of the cryostat. Towards lower temperatures, the mobility decreases much earlier and faster than indicated by the limit due to charged impurity scattering μ_{BH}.

Three mechanisms shall be discussed that could explain the temperature dependence below room temperature:

- Scattering on charged defects: This mechanism is already considered in the simulation. To decrease μ_{BH} to the measured values, a significantly higher amount of charged defects would be necessary. This was not possible under consideration of two acceptors and one donor. Moreover, the Brooks Herring formalism leads to a $T^{3/2}$ law, while the data rather can be described by a T^3 dependence (Fig. 6.5 (a)).

- Hopping: The steep slope of the mobility support this explanation. However, in the case of impurity band conduction, one would also expect a flattening of hole density towards lower temperatures. This behaviour might be visible at the lowest temperatures (see fig. 6.3), but the measured densities scatter strongly so that this is not evident.

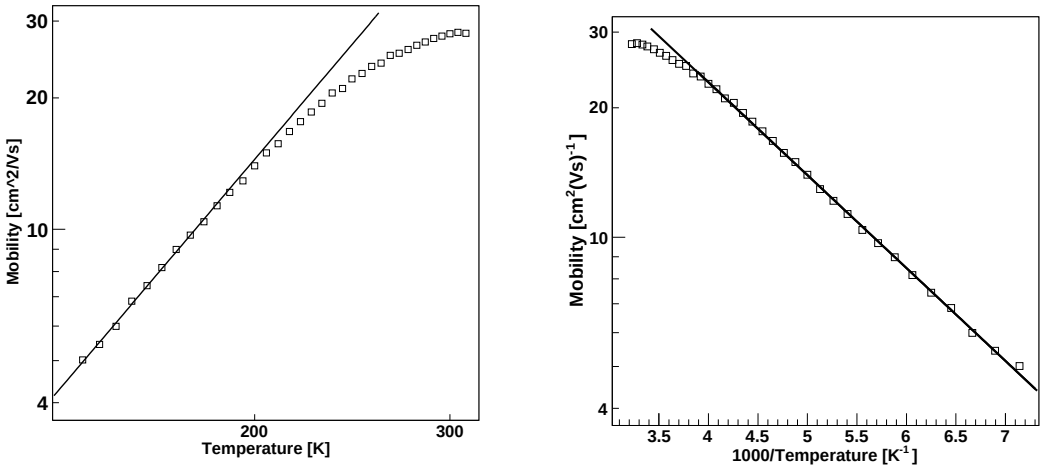

(a) (b)

Figure 6.5: *Temperature dependence of the mobility of sample p1B. Two different interpretations of the data are possible: (a) The solid black line has a T^3 dependence. At low temperatures the measured mobilities seem to follow this slope. The slope is too steep to be explained by scattering on charged impurities which would require a $T^{3/2}$ dependence. A steeper slope could be explained by impurity band conduction. (b) Arrhenius plot of the mobility. The solid black line is a fit to the data below 260 K and has a slope of 42.9±1.8 meV. A thermally activated mobility would be expected in the presence of 2-dimensional defects.*

- 2-dimensional defects: Barriers at 2-dimensional defects lead to thermally activated mobilities (see Sec. 2.1.5). In [Schul02], barrier heights of 60 meV to 120 meV were found for polycrystalline $CuGaSe_2$. [Sie07] presents a twin boundary[1] in an epitaxial $CuGaSe_2$ layer with an activation energy of 32 meV . Figure 6.5 (b) shows an exponential fit with the corresponding Equation (2.57) to the low temperature region ($T < 260$ K) of the data, resulting in a barrier height of 42.9 ± 1.8 meV.

From those three possibilities, only scattering on charged impurities was taken into account for the fit in Figure 6.4, because the others are not expected to be present in an epitaxial material if the conduction takes place in the bands. The model leading to the best accordance with the low temperature data is the thermally activated behaviour at 2-dimensional defects. This is surprising because it is mainly observed in polycrystalline material due to the grain boundaries. Nevertheless, it is possible that 2-dimensional defects, e.g. twin boundaries, have formed in the epitaxial layer over time[2]. Also in the SEM cross section of the layer in Figure A.1, one can see structures that can be interpreted as 2-dimensional defects.

[1] The virtual continuation of the grain lattices meeting at a boundary leads to the so called coincidence site lattice (CSL) as the lattice points where both lattices coincide. Grain boundaries are classified by the ratio Σ of the CSL unit cell volume and the bulk lattice unit cell volume. Twin boundaries have a Σ value of 3 being the lowest possible value. Low Σ values indicate a high coincidence of the two grains and hence contain comparably few defects and show a low activation energy.

[2] The sample was about six years old when the data was taken.

6.2.2 High Activation Energy

The p-type samples grown at the University of Luxembourg, p2-p7, show significantly lower conductivities and also steeper slopes in the arrhenius plot of the charge carrier density.

Single Band Conduction: Sample p2-p4

For three of them (p2-p4), the slope is constant over the whole measured temperature range (Fig. 6.6 (a)), so that it can be assumed that the temperature dependence is dominated by the activation of one acceptor. In this case, the acceptor activation energy can directly be calculated from the slope with the low temperature approximation for a compensated semiconductor (Eq. (2.30)).

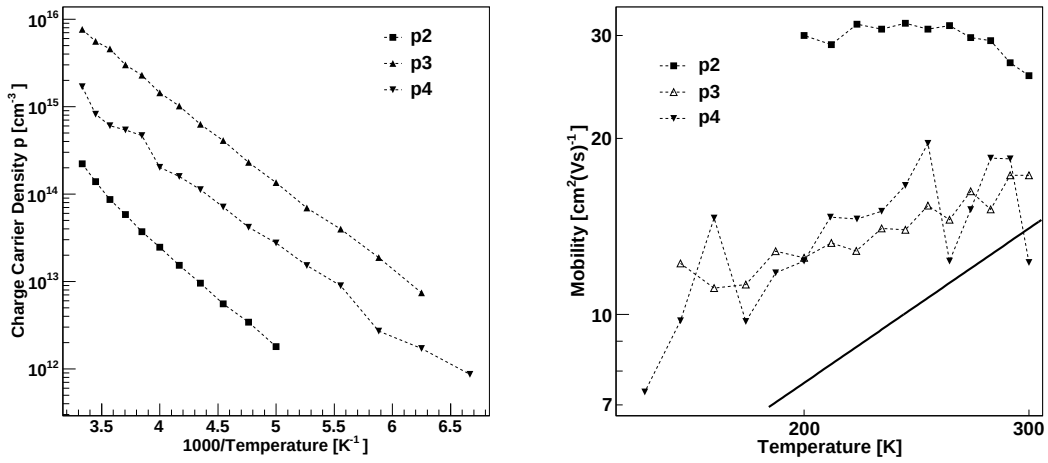

(a) (b)

Figure 6.6: *(a) Measured charge carrier densities of samples p2-p4. One acceptor is dominating over the whole temperature range. (b) Double logarithmic plots of the mobilities of the p-type samples depending on the temperature. The black solid line follows a $T^{3/2}$ dependence representing the temperature dependence of mobility limited by charged impurity scattering.*

Sample Name	p_{300K} [cm^{-3}]	μ_{300K} [cm^2/Vs]	E_a [meV]
p2	$2.2 \cdot 10^{14}$	26	$232 \pm 2^*$
p3	$7.6 \cdot 10^{15}$	17	209 ± 4
p4	$1.7 \cdot 10^{15}$	12	184 ± 21

* fit for Region 200K-260K

Table 6.3: *Room temperature properties of the samples* p2−p4. *The activation energies were determined by a fit to the slope in the Arrhenius plot with Equation* (2.30)*, thus assuming a semiconductor with one acceptor and one compensating donor.*

Table 6.3 gives an overview over the measured properties of samples p2-p4 at room temperature. The charge carrier densities of the p-type samples cover a range from

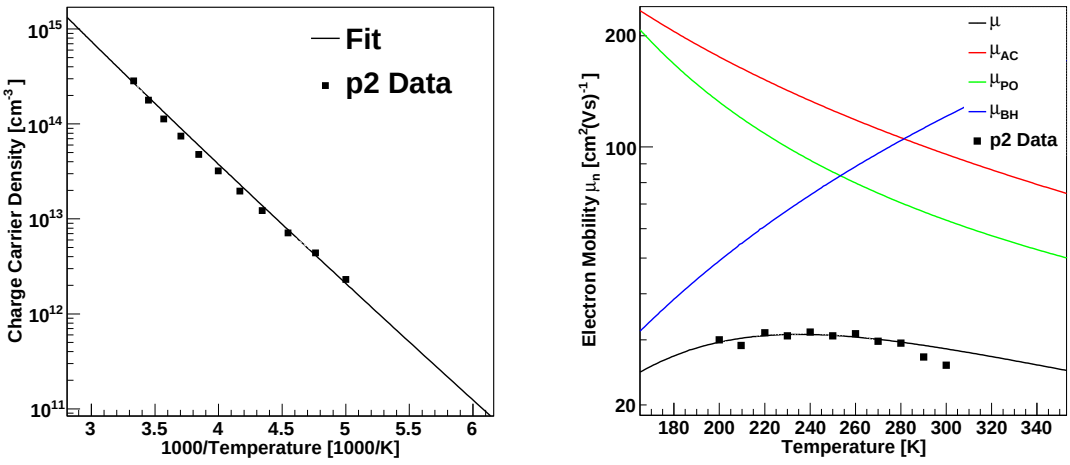

(a) (b)

Figure 6.7: *Fit to the temperature dependent charge carrier density (a) and mobility (b) data of sample p2 with the parameters given in Table 6.4.*

$2.2 \cdot 10^{14}\,\mathrm{cm}^{-3}$ to $7.6 \cdot 10^{15}\,\mathrm{cm}^{-3}$, which is lower then what was reported by other authors (see Tab. 2.4), while the room temperature mobilities $12\,\frac{cm^2}{Vs}$ to $26\,\frac{cm^2}{Vs}$ are in the lower part of the expected range. The acceptor activation energies E_a are located between the levels of $E_{a2} \approx 80\,\mathrm{meV}$ and $E_{a3} \approx 400\,\mathrm{meV}$ as presented in [Was86].

Mobilities: The temperature dependences of the mobilities are shown in Figure 6.6 (b). For sample p2, the transition from impurity to phonon dominated scattering is visible with the characteristic maximum (see Fig. 2.1 and Sec. 2.1.5). At low temperatures the mobility increases with increasing temperature, suggesting a domination of scattering on charged defects, while at higher temperatures the mobility decreases with increasing temperature which is expected to originate from scattering on acoustical and polar optical phonons.

The mobilities of samples p3 and p4 increase with temperature over the whole measured temperature range, indicating domination of charged defect scattering. This assumption is supported by the fact that the mobilities are lower than for p2. As the effect of phonon scattering does not change for different $CuInSe_2$ layers[3], a lower mobility is most likely caused by higher defect densities. This can also explain the hole densities being higher than those measured for sample p2.

The solid black line in Figure 6.6 (b) follows the expected $T^{3/2}$ dependence of the Brooks Herring formalism for scattering on charged carriers, Equation (2.52a). Sample p4 follows this temperature dependence in the interval from 180 K to 250 K, while sample p3 shows a significantly shallower ($T^{3/4}$) but constant slope over the whole measured temperature interval.

[3]Phonon scattering depends on basic material constants like the acoustical respectively optical deformation potential constants, the material density or the velocity of sound.

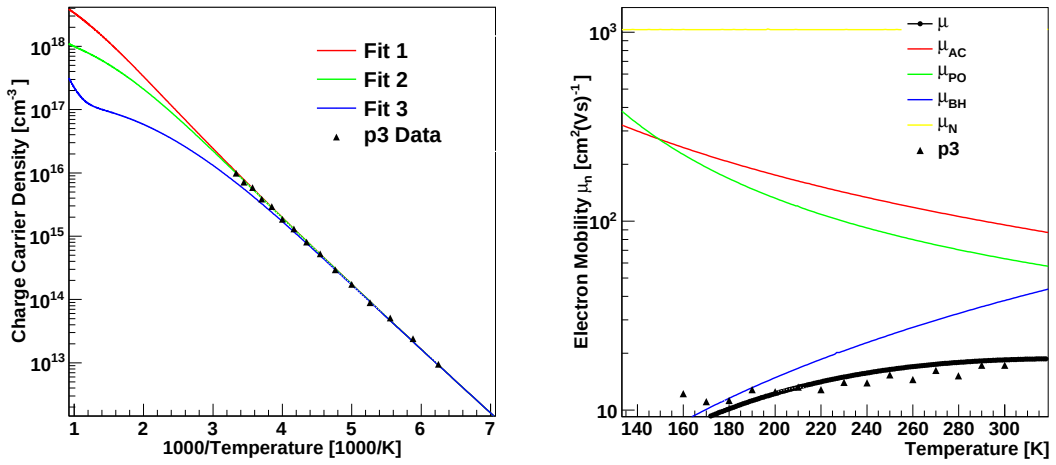

(a) (b)

Figure 6.8: *Fits to the temperature dependent data of sample p3. The parameters are given in Table 6.4. (a) Three different fits to the charge carrier density. (b) Fit1 (see Table 6.4) to the mobility.*

Defect Activation Energies: It is conspicuous that none of the samples shows indications of a shallow acceptor. This is in contradiction to the results from other authors and also to the sample p1B. Although it is not easy to say which defect energy level is created by which crystal defect, it can be assumed that the responsible defect and thus the shallow acceptor level also is present in the samples p2-p4. The fact that it can not be observed can be explained by a high compensation level. If the density of the compensating donor is higher than the density of the shallow acceptor, the acceptor will be completely compensated and thus becomes inaccessible for electrical measurements.

A high compensation level also is in accordance with the comparably low free hole densities of the samples.

	$N_{A1}[\mathrm{cm}^{-3}]$	E_{a1}[meV]	$N_{A2}[\mathrm{cm}^{-3}]$	E_{a2}[meV]	$N_D[\mathrm{cm}^{-3}]$	$N_D/N_{A1}+N_{A2}$
p2	$1.5 \cdot 10^{18}$	220	0	-	$1.31 \cdot 10^{18}$	0.87
p3 Fit 1	$1.5 \cdot 10^{19}$	180	0	-	$6 \cdot 10^{18}$	0.40
p3 Fit 2	$2.5 \cdot 10^{18}$	180	$5 \cdot 10^{18}$	30	$6 \cdot 10^{18}$	0.8
p3 Fit 3	$2.5 \cdot 10^{17}$	180	$5.9 \cdot 10^{18}$	30	$6 \cdot 10^{18}$	0.98

Table 6.4: *Fit parameters for samples* p2 *and* p3*. For all samples in this table, we have* $m_h^* = 0.7m_e$*,* $E_{ac} = 6.5$eV*,* $\epsilon_r = 13.6$*, and* $\epsilon_\infty = 8.1$*.*

Modelling p2 and p3: To determine the defect densities of the samples, the charge carrier densities and mobilities were modelled with the algorithm described in Section 2.1.3 that calculates the densities of carriers and charged and neutral defects from a given set of defect densities and activation energies. The densities of the charged defects then can

be used to calculate the mobilities μ_{BH} and μ_N due to scattering on charged and neutral defects respectively.

Figures 6.7 and 6.8 show fits to the experimental mobilities and hole densities of sample p2 and p3 with the parameters given in Table 6.4. The three main contributing mechanisms limiting the mobilities are scattering on charged impurities, acoustical phonons, and polar optical phonons. The mobilities due to non polar optical phonon scattering and neutral impurities are significantly higher and therefore do not limit the total mobility.

The parameters necessary for modelling phonon scattering – acoustic deformation potential constant E_{ac}, the low and high frequency dielectric constants ϵ_r and ϵ_∞ – and the effective hole mass m_h^* were taken from literature [Was86].

In Figure 6.8 (a) it can be seen that a shallow defect with a concentration below the compensating defect can not be identified by Hall measurements. For Fit 2 and 3, an acceptor of 30 meV was added. To make the simulation fit to the measured free hole densities, the density of the deep acceptor has to be reduced (see parameters in Tab. 6.4). In total, this leads to a significantly higher compensation of 0.80 or even 0.98 instead of 0.40. Those changes affect the charged defect density only slightly and thus do not change the mobility. The density of neutral defects in contrast is changed significantly. Figure 6.8 (b) shows the mobilities resulting from Fit 1 that delivers the highest neutral defect density and thus the lowest limit for scattering on neutral defects. The limit is still far above the limits due to charged defect and phonon scattering.

In the range covered by the experimental data, all three curves follow the measured free hole density. To define a unique solution, it would be necessary to proceed the measurement up to higher temperatures, because the three solutions reach the depletion zone at different temperatures.

Intrinsic Conduction: Sample p5-p7

For samples p5 and p7 the slope in the Arrhenius plot does not follow a simple exponential law, which can be explained by the influence of intrinsic conduction: At high temperatures, intrinsic electrons have a visible influence to the conduction which leads to a lower Hall coefficient and thus to an increase of the apparent hole density as discussed above (see e.g. Fig. 5.1), the apparent charge carrier density of sample p5 becomes negative above 270 K.

Sample Name	$p_{app,300K}$ [cm^{-3}]	$\mu_{app,300K}$ [cm^2/Vs]	σ [(Ωcm)$^{-1}$]
p5	$-3.2 \cdot 10^{13}$	48	$2.5 \cdot 10^{-4}$
p6	$-2.2 \cdot 10^{11}$	840	$3.0 \cdot 10^{-5}$
p7	$6.9 \cdot 10^{15}$	0.3	$3.7 \cdot 10^{-4}$

Table 6.5: *Room temperature properties of the samples* p5−p7.

The data taken for p6 is completely in the negative part of the apparent carrier density. Surprisingly, the apparent electron density decreases with increasing temperature. At the same time, the conductivity decreases towards lower temperatures, following the expected behaviour of semiconductors. This shows that the material originally is p-type, but in the region of intrinsic conduction (see e.g. Fig. 5.1), close to the minimum of the apparent electron density.

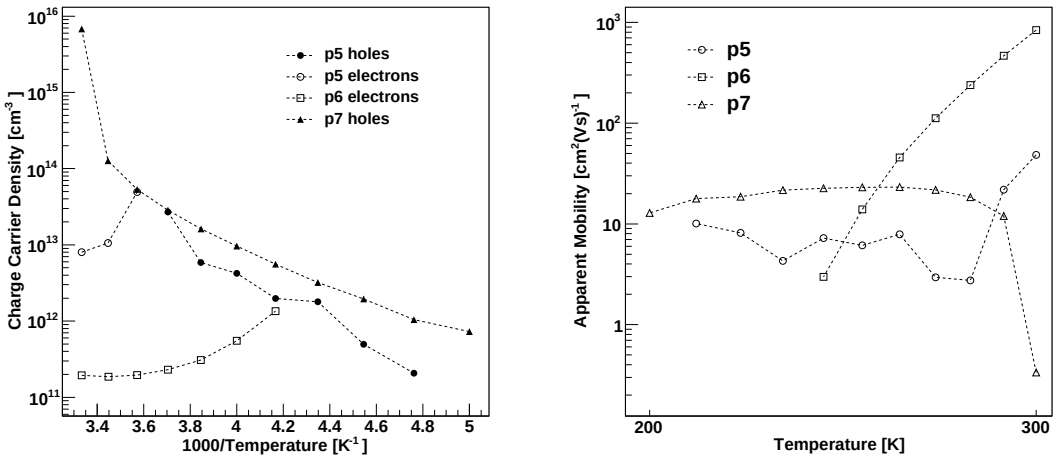

(a) (b)

Figure 6.9: *(a) Measured charge carrier densities of the samples p5-p7. The influence of intrinsic electron conduction is visible so that the shown values are the apparent charge carrier density and have to be separated into hole and electron contributions. (b) Double logarithmic plots of the mobilities of samples p5-p7 depending on the temperature. The mobilities contain (similarly to the charge carrier densities in (a)) both hole and electron contributions and thus are apparent mobilities.*

B-Field Dependence of R_H: Consequently, as both carrier types are involved, the Hall coefficient should depend on the B-field and the Hall voltage should not depend linearly on the B-field. As an example, Figure 6.10 shows the B-field dependence of the Hall voltage for sample p7 at 300 K in the dark. The offset voltage $U_{\text{offset}=}0.0197\,\text{V}$ is already subtracted. The dependence is clearly nonlinear and around 3 T, the Hall voltage even changes its sign, so that the sample would seem p- or n-type, depending on the magnetic field used for the Hall measurement.

Mobility Spectrum Analysis: A MEMSA analysis of the B-field dependent Hall coefficient and conductivity delivers the mobility spectrum shown in Figure 6.11. The main contribution to the conductivity originates from a hole with a mobility of $109\,\text{cm}^2/\text{Vs}$ and

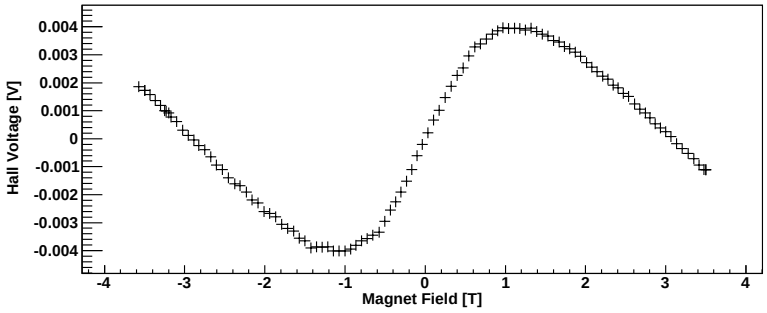

Figure 6.10: *Sample p7: Dependence of the Hall Voltage on the B-field at 300K in the dark.*

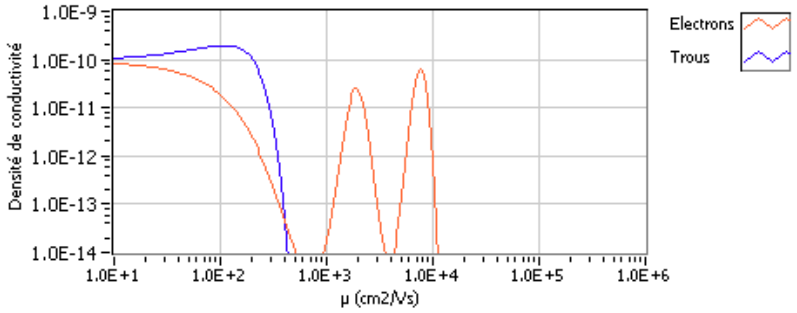

Figure 6.11: *Sample p7: Mobility spectrum at 300 K. red: electrons, blue: holes.*

a density of $2.7 \cdot 10^{13}\,\mathrm{cm}^{-3}$ (see tab. 6.6). Additionally there are contributions from two electrons with mobilities of $1.9 \cdot 10^3\,\mathrm{cm}^2/\mathrm{Vs}$ and $7.7 \cdot 10^3\,\mathrm{cm}^2/\mathrm{Vs}$. With $n_1 = 9.1 \cdot 10^9\,\mathrm{cm}^{-3}$ and $n_2 = 4.2 \cdot 10^9\,\mathrm{cm}^{-3}$, respectively, the electrons provide only 0.049% of the total number of free carriers but due to the significantly higher mobility contribute with 4.7% to the total conductivity.

The second electron can originate from a second valley in the conduction band. As can be seen in the band diagram shown in Figure 2.5, there is a second valley at the N-point. In order to reach the conduction band minimum at the Γ-point, the electron would have to come over a barrier of 0.74 eV. Thus, it is not unlikely, that electrons can stay long enough in this valley to contribute visibly to the transport.

Mobility $[\mathrm{cm}^2/\mathrm{Vs}]$	$\sigma\,[(\Omega\mathrm{cm})^{-1}]$	Density $[\mathrm{cm}^{-3}]$
$-7.7 \cdot 10^3$	$5.0 \cdot 10^{-6}$	$4.2 \cdot 10^9$
$-1.9 \cdot 10^3$	$2.8 \cdot 10^{-6}$	$9.1 \cdot 10^9$
$1.1 \cdot 10^2$	$1.6 \cdot 10^{-4}$	$2.7 \cdot 10^{13}$

Table 6.6: *Overview of the observed charge carriers in sample* p7. *For every peak in the mobility spectrum, the position, the contribution to the sheet conductivity and the carrier density is given.*

Mobilities: For the interpretation of the mobilities measured for the intrinsic samples p5-p7, one has to keep in mind that the mobility is calculated from the Hall coefficient: $\mu = R_H \cdot \sigma$. In case of contributions from both holes and electrons to the Hall coefficient, the mobility is – similar to the carrier densities – an apparent mobility.

Competing electron and hole contributions to the Hall coefficient lower the absolute value of R_H and thus lead to lowered apparent mobilities. Nevertheless, parts of the behaviour can be explained.

At high temperatures, the fraction and thus the influence of electrons is higher than at rather low temperatures.

This certainly explains the drop of the mobility of p7 at 300 K. It corresponds to the Hall coefficient crossing zero: Here the apparent type of the sample is about to change and Hall coefficient and thus the apparent mobility are close to zero. For p5, this drop is not visible as the zero crossing takes place between the points at 270 K and 280 K (see

Fig. 6.9). From 280 K to 300 K, the electron contribution becomes stronger, so that the apparent mobility increases towards the expected electron mobility.

In sample p6, electrons dominate over the whole measured range, but at low temperatures, the influence from holes still leads to a very low apparent mobility ($3.0\,cm^2(Vs)^{-1}$ at 240 K). Towards higher temperatures the apparent mobility again increases strongly as the hole contribution goes down.

6.3 n-type $CuInSe_2$

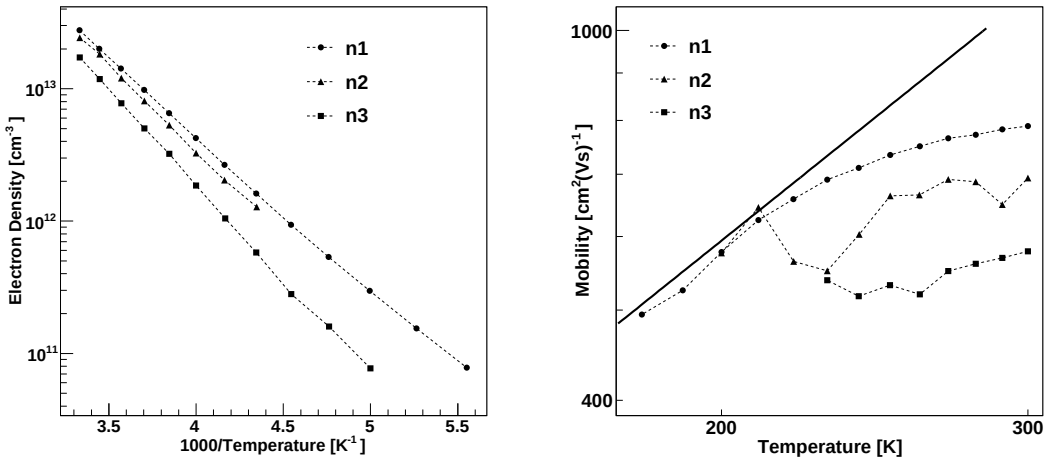

Figure 6.12: *Electron densities and mobilities of the n-type samples. The black solid line in the plot of the mobilities follows a $T^{3/2}$ dependence that would be expected for domination of charged impurity scattering.*

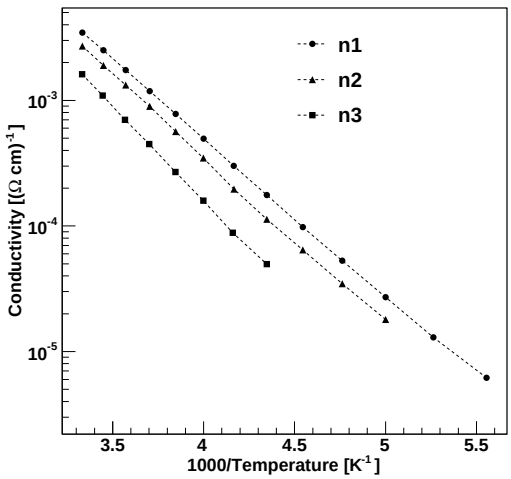

Figure 6.13: *Conductivity of the n-type samples.*

The three n-type samples n1, n2 and n3 show room temperature charge carrier densities of 1.7 to $2.7 \cdot 10^{-13}\,\mathrm{cm}^{-3}$ and mobilities between 580 $\frac{cm^2}{Vs}$ and 790 $\frac{cm^2}{Vs}$ (see Fig. 6.12). In the Arrhenius plot one can see that the electron density is thermally activated with a constant slope for the whole measured range. For a compensated semiconductor, the activation energy E_d of the donor is the slope of the Arrhenius plot (2.31). This leads to activation energies E_d of 210 meV to 250 meV (see Table 6.7) which is close to the deepest donor E_{d3} found in bulk single crystals (see chapter 2.2.4).

Sample Name	$n_{300K}\,[\mathrm{cm}^{-3}]$	$\mu_{300K}\,[\mathrm{cm}^2/\mathrm{Vs}]$	$E_d\,[\mathrm{meV}]$
n1	$2.7 \cdot 10^{13}$	790	210
n2	$2.4 \cdot 10^{13}$	700	230
n3	$1.7 \cdot 10^{13}$	580	250

Table 6.7: *n-type CISe-Samples*

The electron mobility (see Fig. 6.12) of sample n1 increases with the temperature, which leads to the conclusion that the mobilities are dominated by scattering on charged defects (see chapter 2.1.5). In the low temperature range, it roughly follows a $T^{3/2}$ law (see solid black line in Fig. 6.12) as expected from the Brooks Herring formalism (Sec. 2.1.5). At higher temperatures, the transition to domination of phonon scattering begins and the slope becomes shallower. For the other two samples, a clear trend is not visible because the values scatter too strongly.

6.4 Summary

The temperature dependence of the hole densities show, that in the examined temperature range the electrical transport of sample p1B is clearly dominated by shallower acceptors than the other p-type samples p2-p7.

The difference between p1B and p2-p7 can be explained by a higher donor density that leads to a complete compensation of the shallower acceptors. The other possible solution, a significantly lower defect density, would lead to higher hole mobilities, which is not supported by observation.

Samples p2-p4 can be described by single band conduction. Over the whole measured temperature range, the charge carrier density follows an exponential law which can be explained by the thermal activation of one deep acceptor. Free hole densities and conductivity are lower than for p1B already at room temperature. In combination with the steeper slope this leads to very low values at lower temperatures which made it impossible to measure the Hall coefficient below 150 K.

For samples p5-p7, the compensation becomes even larger and thus the number of free carriers decreases such that the electric properties finally are influenced by intrinsic band to band excitation.

With mobility spectrum analysis, the carriers contributing to the electrical transport of sample p7 are identified. In addition to the contributions resulting from the valence band maximum and the conduction band minimum at the Γ point, there is a second electron

peak. The band diagram for $CuInSe_2$ shows a second valley at the n-Point that could be the origin of this electron.

An EDX[4] study leads to a slightly higher copper to indium ratio for p1B than for the samples produced at the University of Luxembourg (see Table A.2). The Cu and In contents of p1B separately are within the errors of the copper and indium contents of the other samples, so that the deviation in the ratio can not be regarded as significant. However, slight changes in the composition can have large influence on the defect distribution. For the electrical transport it makes a significant difference whether the density of Cu vacancies is $10^{16}\,cm^{-3}$ or $10^{17}\,cm^{-3}$, but this difference will not be measurable by EDX or any other available technique.

[4]Energy Dispersive X-Ray Spectroscopy

Chapter 7

Photo Hall Measurements

Photo Hall measurements were performed under illumination from a halogen lamp (see Sec. 4.3.1). In Section 7.1 the effect of illumination of a $CuGaSe_2$ layer is examined and compared to an earlier study [Ris07, Sie08].

In Section 7.2, the behaviour of the $CuInSe_2$ sample p1B which is dominated by a shallow acceptor will be presented. Section 7.3 discusses the effect of illumination on the samples p2-p4 and n1-n3 that show a higher acceptor activation energy.

7.1 Photo Hall Measurements on $CuGaSe_2$

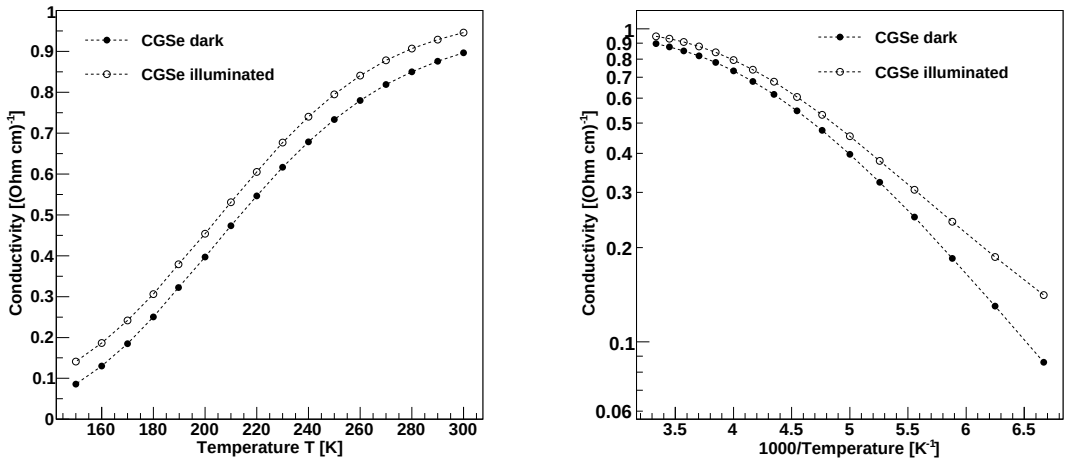

Figure 7.1: *Temperature dependence of the conductivity of the $CuGaSe_2$ sample CGS in the dark and under illumination. The linear plot on the left shows that the conductivity increases by a constant value for all temperatures.*

Photo Hall measurements on epitaxial $CuGaSe_2$ grown on GaAs were reported before by [Ris07, Sie08] who assumed that electrical transport properties of $CuGaSe_2$ under illumination can still be described by single band conduction down to temperatures below 100 K, but observed a deactivation of the compensating donors. To verify these results and compare them to the data from $CuInSe_2$ samples, a $CuGaSe_2$ layer was also examined for

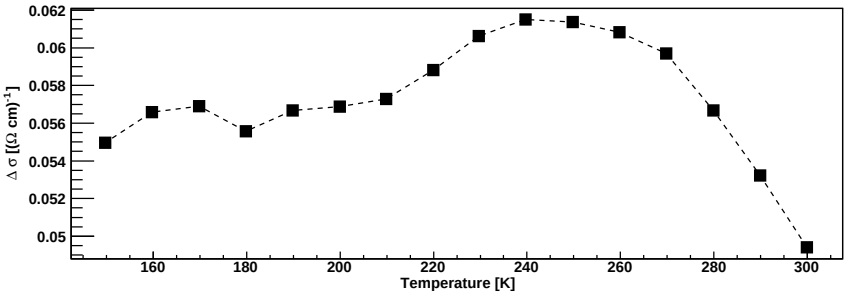

Figure 7.2: *Difference between conductivity under illumination and in the dark for sample CGS:* $\Delta\sigma = \sigma_{illum} - \sigma_{dark}$. *The curve follows the typical temperature dependence of the carrier mobility.*

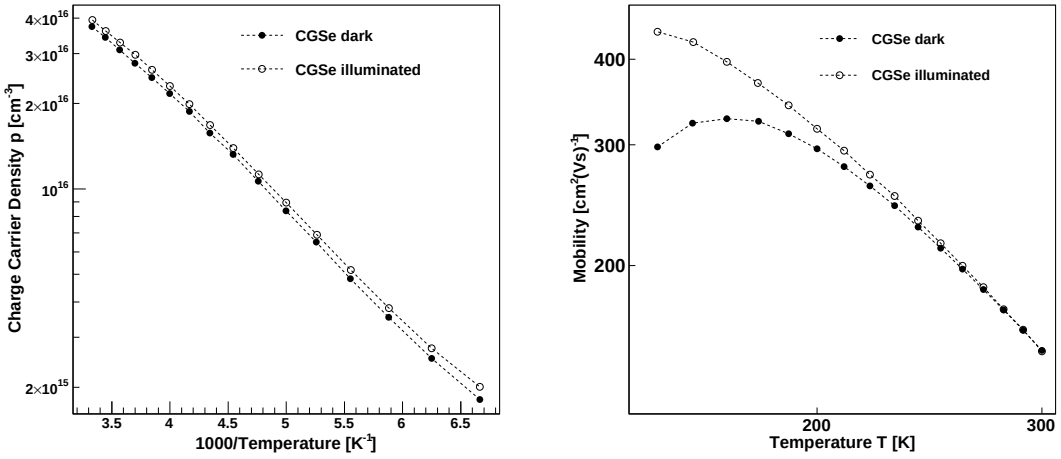

(a) (b)

Figure 7.3: *Temperature dependence of the hole density and mobility of the* $CuGaSe_2$ *sample CGS in the dark and under illumination.*

this work. The sample CGS was grown at the University of Luxembourg similarly to the $CuInSe_2$ samples by MOVPE on a (100) oriented GaAs substrate.

For photo hall measurements on $CuGaSe_2$, one has to take into account, that the band gap of $CuGaSe_2$ (1.6 eV) is larger than the bandgap of GaAs (1.4 eV) and thus, light in the energy range between the band gaps is not absorbed in the $CuGaSe_2$ layer, but can induce charge carriers in the GaAs. Therefore a filter is necessary when using white light. For the measurements described here, a 700 nm ($\widehat{=}$ 1.77 eV) short pass filter was used.

The density of photo generated charge carriers was estimated in Section 4.3.1 to a value of $n_{CuGaSe2} \approx 1.7 \cdot 10^{12}\,\mathrm{cm}^{-3}$, which is one and two orders of magnitude below the densities of $1.3 \cdot 10^{13}\,\mathrm{cm}^{-3}$ and $2.5 \cdot 10^{14}\,\mathrm{cm}^{-3}$ in [Ris07] respectively.

With $p_{300\,K} = 3.7 \cdot 10^{16}\,\mathrm{cm}^{-3}$, the room temperature charge carrier density of CGS in the dark is similar to the sample CGS379a used for the photo hall measurements in [Ris07] and lies between the $CuInSe_2$ samples p1B and p2 described in chapter 6.

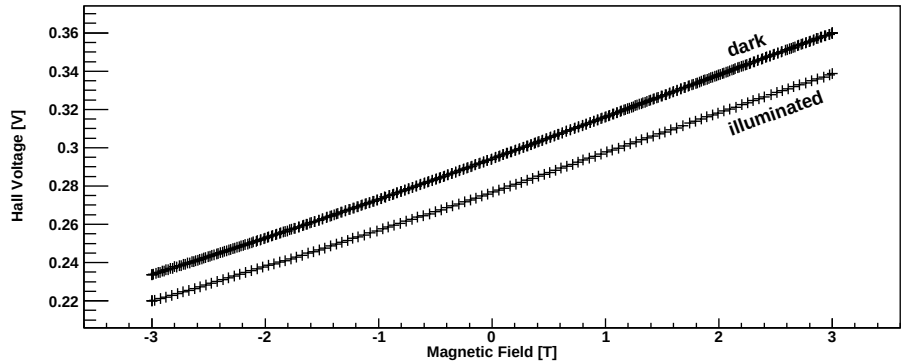

Figure 7.4: *Comparison of the B-field dependence of the Hall voltage U_H for sample CGS at room temperature (300 K) in the dark and under illumination. The shown values are the sum of offset voltage U_{offset} and Hall voltage U_H with $U_{offset} = 0.277$ V in the dark and 0.294 V under illumination. The fact that U_H depends linearly on the magnetic field shows, that electrical transport can be described by single band conduction.*

Conductivity: The conductivity at each temperature grows by a constant value of $\Delta\sigma = 0.057 \pm 0.003\,\Omega^{-1}\text{cm}^{-1}$ (see Fig. 7.1), which corresponds to the assumption of a constant density of charge carriers $n_{photo} = p_{photo}$. With $\Delta\sigma = \sigma_{photo} = \Delta n \cdot \mu \cdot e$, a constant $\Delta\sigma$ can only be expected with a constant μ. As shown in Figure7.2, the $\Delta\sigma(T)$ are indeed not distributed randomly around the mean value but seem to follow a curve similar to the expected temperature dependency of the mobility with a maximum at 240 K and decreasing values towards both higher and lower temperatures. Due to the higher mobility of electrons, the curve is expected to follow the electron mobility so that the difference to the shape of the hole mobility is not a contradiction.

Also for $CuGaSe_2$ it can be expected that the electron contribution for $n = p$ is stronger than the hole contribution, but only the hole mobility is known from the measurement. Thus, an interpretation of $\Delta\sigma(T)$ under consideration of the mobilities is not possible. On the other hand, an estimation for the order of magnitude of the electron mobility is possible. With the measured hole mobility around 250 K, $\mu_p = 200\,\text{cm}^2(\text{Vs})^{-1}$ and the estimated density of electron hole pairs $n = 1.7 \cdot 10^{12}\,\text{cm}^{-3}$, the electron mobility can be calculated as follows:

$$\Delta\sigma = \Delta n \cdot (\mu_n + \mu_p) \cdot e \tag{7.1}$$

$$\Rightarrow \mu_n = \frac{\Delta\sigma}{\Delta n \cdot e} - \mu_p = 2.1 \cdot 10^5\,\text{cm}^2(\text{Vs})^{-1}, \tag{7.2}$$

This value seems to be very high, but with a ratio of $\mu_n/\mu_p = 690$ based on the effective masses an the predominant scattering mechanism [Ger00], the resulting electron mobility is in the same order of magnitude:

$$\mu_n = \mu_p \cdot 690 = 1.4 \cdot 10^5\,\text{cm}^2(\text{Vs})^{-1}, \tag{7.3}$$

Effects on Hall coefficient and Hall voltage: In the Arrhenius plot of the apparent hole density, Figure 7.3 (a), one can see that the density does not change significantly

under illumination, but is at all temperatures slightly higher than in the dark. This can be explained by a small influence of both photoinduced holes and electrons: While the holes increase the actual free hole density, the electrons decrease the Hall coefficient and thus lead to a higher apparent density.

Figure 7.4 compares the B field dependence of the Hall voltage U_H in the dark and under illumination. The offset voltages U_{offset} are 0.277 V under illumination and 0.294 V in the dark. In both cases, U_H is proportional to the field, so that single band conduction can be assumed, approving the assumptions of [Ris07]. The second possible reason for a B-field independent Hall coefficient – the low field approximation $\mu B \ll 1$ – can also be excluded due to the high electron mobility (compare to estimation for $CuInSe_2$ in Section 5.3).

Differences to earlier Study: In contrast to the results of [Ris07], the compensating donors stay active under illumination. In [Ris07], the disappearance of the donor was explained by the metastable behaviour of the selenium vacancy, which was predicted by [Lan06].

A reason for the absence of this effect might be the different conditions of the illumination: While [Ris07] used a 514 nm laser, sample CGS was illuminated with white light in combination with a 700 nm short pass filter, resulting in a photon flux which is one order of magnitude lower. It is possible that the illumination intensity was too low to change the type of a sufficient number of donors. A second explanation could be that the compensating donors might originate from a different crystal defect that is not metastable.

7.2 Low Activation Energy $CuInSe_2$

Under illumination, sample p1B clearly shows multiple band conduction as can be concluded from the nonlinear B-field dependence of the Hall voltage U_H in Figure 3.1. In the following, temperature and B-field dependent measurements performed on this sample will be discussed.

7.2.1 Temperature dependent measurements

Figure 7.5 shows the temperature dependence of the Hall coefficient at different B-fields. In all cases, R_H is positive (p-type) at 300 K and becomes negative (n-type) at low temperatures, but the change of sign of the Hall coefficient happens at different temperatures due to its B-field dependence.

Only the data taken with a B-Field of 5 T shows domination of hole conduction over a sufficiently large temperature interval to allow the determination of an activation energy from the charge carrier density (Fig. 7.6). Under the assumption of a compensated material, the determined acceptor activation energy is 36 meV.

It was tried to model the data with Equation (3.26):

$$R_H(B) = \frac{p\mu_p^2 - n\mu_n^2}{e(p\mu_p + n\mu_n)^2} \tag{7.4}$$

The hole mobility and thermally induced hole density $p_{thermal}$ can be taken from the measurements in the dark (see chapter 6.2.1) and the photo induced carrier density $n_{photo} =$

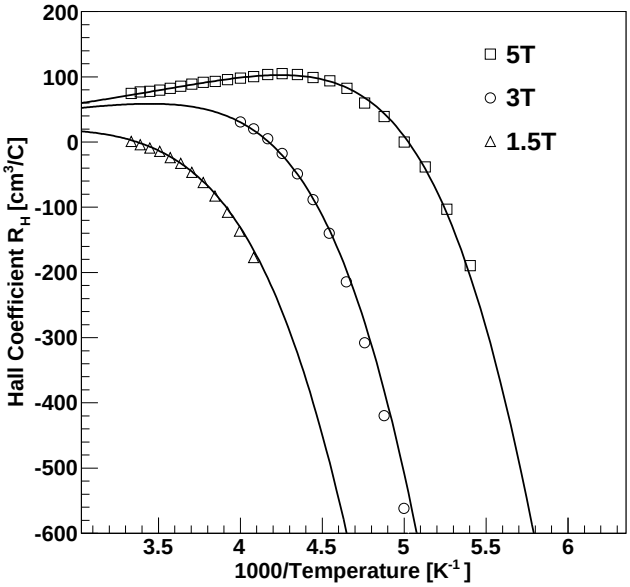

Figure 7.5: *Three temperature dependent runs at different B-fields. The Hall coefficient depends strongly on the B-field which is a proof for multiple band conduction. At low temperatures, R_H becomes negative in all cases. The black lines are attempts to fit the data under use of the low B-field approximation Equation* (3.26).

p_{photo} is estimated as shown in chapter 4.3.1. The free carrier densities are calculated as follows:

$$n = n_{photo} \tag{7.5}$$

$$p = p_{thermal} + p_{photo} \tag{7.6}$$

While the hole mobility increases with temperature, the data can only be described under the assumption of an electron mobility that decreases with temperature. The dominating scattering mechanism for this temperature behaviour of the mobility is most likely phonon scattering. The temperature dependence of phonon scattering can be described by a T^{-x} law with $x \approx \frac{3}{2}$ (see Sec. 2.1.5). Thus, the last free parameter is the room temperature electron mobility $\mu_{300\,K}(B)$.

The solid black lines in Figure 7.5 are fits of equation (7.4) to the three measured curves under those assumptions. The electron mobilities at room temperature are fitted to be $\mu_{300\,K}(5\,\mathrm{T}) = 31\,\mathrm{cm}^2/\mathrm{Vs}$, $\mu_{300\,K}(3\,\mathrm{T}) = 83\,\mathrm{cm}^2/\mathrm{Vs}$ and $\mu_{300\,K}(1.5\,\mathrm{T}) = 241\,\mathrm{cm}^2/\mathrm{Vs}$.

Although it is possible to describe each of the datasets separately with the low B-field approximation of R_H, the B-field dependence of the Hall coefficient shows, that this approximation is not valid. Therefore, the mobility spectrum analysis was used to differentiate between the contributions of electron and hole mobilities.

7.2.2 Mobility Spectrum Analysis

By analysing the B-Field dependence of hall mobility and conductivity at a given temperature, the mobility spectrum analysis method described in chapter 3.2 is able to detect

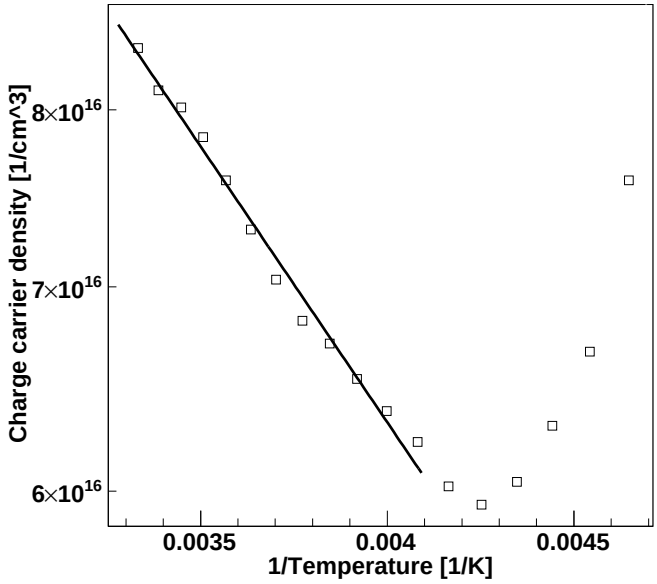

Figure 7.6: *Arrhenius plot of the charge carrier concentration, measured under illumination at 5T. The fit is done using equation* (2.30) *in the temperature interval 245 K to 300 K and leads to an activation energy of 36 meV*

contributions from any number of holes and electrons. Figure 7.7 shows the resulting charge carrier mobility spectra for sample p1B at different temperatures, Table 7.1 gives an overview over the peak positions, the contributions to the sheet conductivity and the carrier density.

The number and range of magnetic fields covered during the measurements vary from temperature to temperature because of performance instabilities of the cooling system for the superconducting magnet (see Sec. 4.2.6). At 280 K for example, the highest field is 2 T.

Contribution to Conductivity: In Table 7.1, the main contribution at every temperature is given in bold print. Peaks with contributions more than two orders of magnitude below the main contribution are put in parentheses. These are most likely ghost peaks that originate from small fluctuations in the data (see Sec. 3.2.2). The high mobility hole ($3.4 \cdot 10^4\,\mathrm{cm}^2/\mathrm{Vs}$) at 180 K contributes more than 1% to the total conductivity but probably also is a ghost peak because at no other temperature, a significant high mobility hole contribution was observed.

Another effect of bad quality data is visible at 260 K: The $261\,\mathrm{cm}^2/\mathrm{Vs}$ electron is a mirror peak of the $251\,\mathrm{cm}^2/\mathrm{Vs}$ hole. The mirror peak influences the original peak so that peak positions and carrier densities for this dataset are not reliable.

For all temperatures except 260 K, the main contributing carrier is a hole with a mobility between $24\,\mathrm{cm}^2/\mathrm{Vs}$ (at 220 K) and $76\,\mathrm{cm}^2/\mathrm{Vs}$ (at 280 K). The other contributions result from one or two electrons with mobilities between $4.4 \cdot 10^3\,\mathrm{cm}^2/\mathrm{Vs}$ and $2.2 \cdot 10^4\,\mathrm{cm}^2/\mathrm{Vs}$. The conductivity resulting from the holes is growing with temperature, because the sample is in the regime of acceptor reserve. The contribution of electron conduction seems to

peaks separately				electrons vs. holes	
T [K]	μ [cm^2/Vs]	σ [(Ωcm)$^{-1}$]	n [cm^{-3}]	σ [(Ωcm)$^{-1}$]	σ/σ_{tot}
180	$\mathbf{6.8 \cdot 10^1}$	$\mathbf{1.9 \cdot 10^{-1}}$	$\mathbf{3.8 \cdot 10^{16}}$	$\sigma_{\mathbf{tot}} = \mathbf{2.4 \cdot 10^{-1}}$	
	$(3.4 \cdot 10^4$	$4.0 \cdot 10^{-3}$	$7.6 \cdot 10^{11})$	$\sigma_p = 1.9 \cdot 10^{-1}$	80.5%
	$-8.0 \cdot 10^3$	$3.1 \cdot 10^{-2}$	$2.4 \cdot 10^{13}$	$\sigma_n = 4.7 \cdot 10^{-2}$	19.5%
	$-2.3 \cdot 10^4$	$1.6 \cdot 10^{-2}$	$4.3 \cdot 10^{12}$	.	
200	$\mathbf{4.7 \cdot 10^1}$	$\mathbf{2.5 \cdot 10^{-1}}$	$\mathbf{4.9 \cdot 10^{16}}$	$\sigma_{\mathbf{tot}} = \mathbf{2.8 \cdot 10^{-1}}$	
	$-4.4 \cdot 10^3$	$8.7 \cdot 10^{-3}$	$1.2 \cdot 10^{13}$	$\sigma_p = 2.5 \cdot 10^{-1}$	90.7%
	$-1.3 \cdot 10^4$	$1.7 \cdot 10^{-2}$	$8.2 \cdot 10^{12}$	$\sigma_n = 2.6 \cdot 10^{-2}$	9.3%
	$(-1.3 \cdot 10^5$	$1.57 \cdot 10^{-5}$	$7.4 \cdot 10^8)$	.	
220	$\mathbf{2.4 \cdot 10^1}$	$\mathbf{3.2 \cdot 10^{-1}}$	$\mathbf{9.8 \cdot 10^{16}}$	$\sigma_{tot} = 3.3 \cdot 10^{-1}$	
	$-8.8 \cdot 10^3$	$8.0 \cdot 10^{-3}$	$5.7 \cdot 10^{12}$	$\sigma_p = 3.2 \cdot 10^{-1}$	97.6%
				$\sigma_n = 8.0 \cdot 10^{-3}$	2.4%
240	$\mathbf{2.7 \cdot 10^1}$	$\mathbf{3.7 \cdot 10^{-1}}$	$\mathbf{1.1 \cdot 10^{17}}$	$\sigma_{tot} = 3.8 \cdot 10^{-1}$	
	$-1.4 \cdot 10^4$	$5.0 \cdot 10^{-3}$	$2.2 \cdot 10^{12}$	$\sigma_p = 3.7 \cdot 10^{-1}$	98.7%
				$\sigma_n = 5.0 \cdot 10^{-3}$	1.3%
260	$(\ 1.8 \cdot 10^4$	$5.3 \cdot 10^{-4}$	$1.9 \cdot 10^{11})$	$\sigma_{tot} = 4.6 \cdot 10^{-1}$	
	$\mathbf{2.5 \cdot 10^2}$	$\mathbf{3.3 \cdot 10^{-1}}$	$\mathbf{4.9 \cdot 10^{16}}$	$\sigma_p = 3.3 \cdot 10^{-1}$	71.1%
	$-2.6 \cdot 10^2$	$1.3 \cdot 10^{-1}$	$5.1 \cdot 10^{15}$	$\sigma_n = 1.3 \cdot 10^{-1}$	28.9%
	$-9.2 \cdot 10^3$	$4.3 \cdot 10^{-3}$	$2.9 \cdot 10^{12}$		
	$(-2.7 \cdot 10^4$	$8.7 \cdot 10^{-5}$	$2.0 \cdot 10^{10})$		
280	$\mathbf{7.6 \cdot 10^1}$	$\mathbf{3.7 \cdot 10^{-1}}$	$\mathbf{6.8 \cdot 10^{16}}$	$\sigma_{tot} = 3.8 \cdot 10^{-1}$	
	$-8.3 \cdot 10^3$	$5.0 \cdot 10^{-3}$	$3.8 \cdot 10^{12}$	$\sigma_p = 3.3 \cdot 10^{-1}$	98.7%
				$\sigma_n = 5.0 \cdot 10^{-3}$	1.3%

Table 7.1: *Overview of the observed charge carriers. For every peak in the mobility spectrum, the position, the corresponding conductivity and the carrier density is given. The main contribution for each temperature is highlighted. In the last two columns, the electron and hole contributions are summed up.*

decrease for higher temperatures. As the density of electrons stays constant for all temperatures, this can only be explained by a decreasing electron mobility and thus a domination of phonon scattering for the electrons.

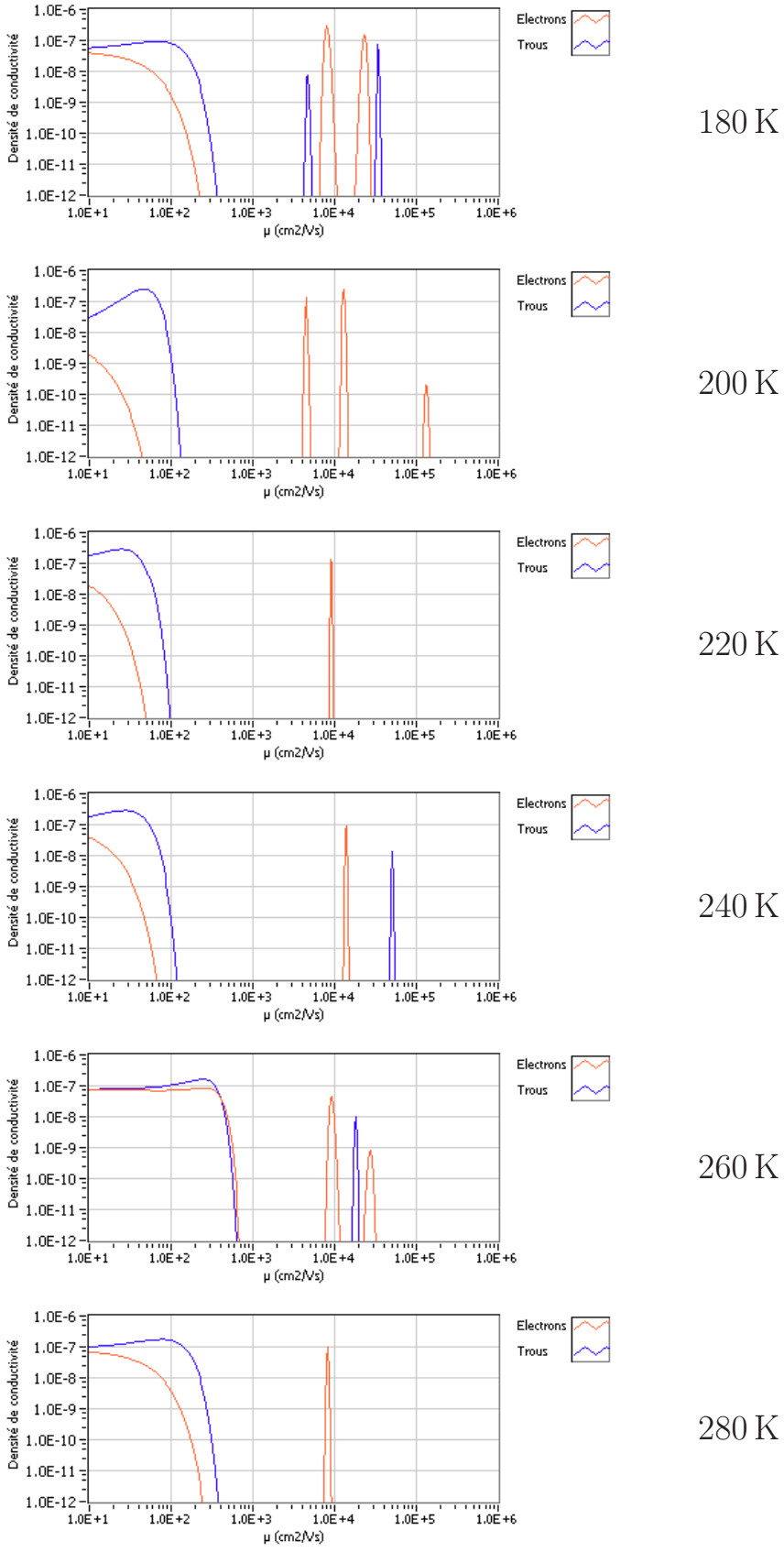

Figure 7.7: *Mobility spectra of sample p1B at different temperatures: 180 K, 200 K, 220 K, 240 K, 260 K and 280 K (from top to bottom). red: electrons, blue: holes*

Peak number and position: At most temperatures the hole mobility is significantly higher than the values determined for single band conduction in the dark (see figs. 6.4 and 6.5) and the temperature dependence does not follow a clear trend. The reason for this might be that the maximum field that could be achieved during the measurements was not sufficiently high for a good resolution of low mobility carriers (see Sec. 3.2.2).

Number, position, and conductivity of detected electron peaks vary from temperature to temperature, therefore it is not possible to confidently identify the same electron at different temperatures. The mobilities of the strongest electrons at every temperature lie around $10^4\,\mathrm{cm}^2/\mathrm{Vs}$. At 180 K and 200 K, the conductivity attributed to the second electron is only about a factor of 2 below the strongest one, at higher temperatures, one of the electrons is clearly dominating.

Second electron: The fact that two electrons are visible in sample p1B at the lowest temperatures where the influence of electron conduction is stronger than at high temperatures as well as in sample p7 in the dark (see Fig. 6.11) supports the assumption that those peaks may originate from conduction in different valleys of the conduction band and not from fluctuations in the data. Comparing the electron mobilities at 180 K and 200 K, the electron mobilities decrease towards the higher temperature. This could explain the disappearance of the second electron: If the mobility of the slower electron decreases further, its relatively low contribution with respect to the hole cannot be resolved in the given B-field range and thus is not visible any more.

Botti [Bot12] has derived an effective mass of 0.16 m_e or 0.23 m_e, depending on the approach (see Tab. 2.1) for the second electron. This is a factor of approximately 2 higher than for the electron at the Γ-point so that one can guess, that the higher mobility electron corresponds to the conduction band minimum, while the lower mobility electron originates from the N-point.

Summary: In total, one can say that the MEMSA analysis qualitatively gives conclusive results but the quantitative interpretation does not lead to reliable numbers. Reasons for this can be found in the data quality, for example due to differing numbers of data points, the relatively low maximum field strength or the long measuring times[1].

7.3 High Activation Energy $CuInSe_2$

The samples p2-p4 and n1-n3 which can be described by single band conduction in the dark were also measured under illumination. For both p- and n-type samples the influence of the photo induced carriers is clearly visible.

7.3.1 p-Type $CuInSe_2$

For all samples, the influence of electron conduction increases under illumination, as was already seen for the low activation energy sample p1B in Section 7.2.

[1] Especially at low magnetic fields and thereby small Hall voltages, small changes in the sample, for example due to a not entirely terminated relaxation, will influence the results significantly. The long measuring times needed for every point increase this problem.

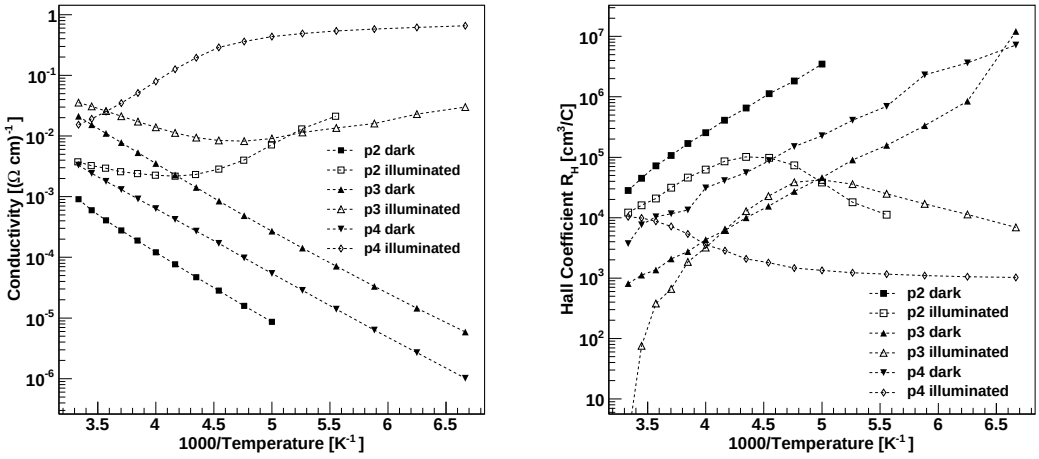

Figure 7.8: *Comparison of conductivity and Hall coefficient of 3 p-type $CuInSe_2$ samples in the dark and under illumination. In order to allow logarithmic plotting, the plot shows the absolute values. Almost all Hall coefficients measured under illumination are negative, only for sample p3, R_H becomes positive at 300 K*

Conductivities: The conductivities of the samples increase because photo induced excitation is an additional source of free charge carriers. Hence the total conductivity σ_{tot} can be expressed as the sum of thermally induced σ_{therm} and light induced $\sigma_{photo} = \Delta\sigma$ conductivity:

$$\sigma_{tot} = \sigma_{therm} + \Delta\sigma \tag{7.7}$$

$$\Delta\sigma = n_{photo} \cdot e \cdot (\mu_n + \mu_p) \tag{7.8}$$

As can be seen in Figure 7.10, the gain of conductivity is $\Delta\sigma \approx 0.002\,(\Omega \cdot \mathrm{cm})^{-1}$ for sample p2 and $\Delta\sigma \approx 0.01\,(\Omega \cdot \mathrm{cm})^{-1}$ for sample p3 in the high temperature range between 200 K and 300 K. At lower temperatures, $\Delta\sigma$ becomes larger and the conductivity of the samples start to increase with decreasing temperature.

Towards low temperatures, the defect induced charge carriers freeze out so that the charge carrier density converges to n_{photo} as was show in Section 5.2. Therefore, changes in the conductivity that were previously dominated by the carrier densities are now proportional to the mobility. The increasing conductivity towards lower temperatures consequently is caused by an increasing hole mobility, indicating phonon dominated electron scattering. This effect is not visible in the measured mobilities of those samples (Fig. 7.9), because they are again apparent mobilities and still in the transition from the hole to the electron mobility.

Hall Coefficient: A comparison of the Hall coefficient in the dark and under illumination for the samples is shown in Figure 7.8. Under illumination it is negative over almost the whole measured temperature range and only becomes positive for sample p3 at 300 K. Its absolute value increases with temperature at low temperatures until it reaches a maximum

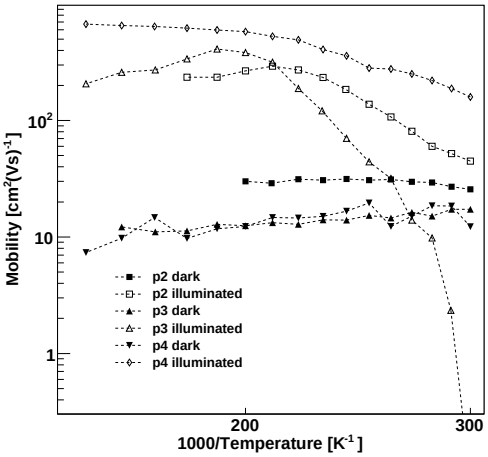

Figure 7.9: *Comparison of the carrier mobilities of 3 p-type $CuInSe_2$ samples in the dark and under illumination.*

around 200 K. This maximum is also observed in the simulation in Figure 5.2 and can be explained by the growing electron mobilities and thus domination of charged defect scattering for the electrons.

This effect is visible for samples p2 and p3. At higher temperatures the absolute value decreases again and as mentioned above, the Hall coefficient becomes positive for sample p3. For the other samples the sign change is not visible, but can be expected for higher temperatures if the domination of intrinsic conduction does not start before the domination of defect induced conduction (see Fig. 5.2).

Sample p4 seems to show a completely different behaviour: First, the conductivity decreases with temperature over the whole measured temperature interval from 150 K to 300 K and second, the absolute value of the Hall coefficient increases with the temperature. By assuming that the extremal point of conductivity and Hall coefficient is not around 200 K but above 300 K for this sample the temperature dependent behaviour is still consistent with the behaviour of the other samples.

This could be explained by a lower contribution of the holes to the transport, caused for example by higher compensation, which would also fit to the domination of charged impurity scattering that was found for the holes in this sample (see Sec. 6.2.2).

Interesting is the low temperature part of sample p4. Here, the Hall coefficient seems to level off to a constant value, which is expected for a situation with the acceptor generated hole density $p_{thermal} = 0$ and a temperature independent light induced electron and hole density $p_{photo} = n_{photo}$. Still, the resulting Hall coefficient has to be calculated from equation (3.26) to take both electron and hole contributions into account, but in the case of $\mu_n \gg \mu_p$, the contribution of the holes can be neglected and equation (3.26) transforms into equation (3.10). The apparent mobility of 670 cm^2/Vs should then be close[2] to the actual electron mobility at 150 K. The photo induced free electron density then is $6.1 \cdot 10^{15}\,cm^{-3}$.

[2]With the hole mobility measured in the dark $mu_p \approx 10\,cm^2/Vs \Rightarrow \frac{\mu_p}{\mu_n} = 0.015$ in equation (3.32), the error of R_H is 3%.

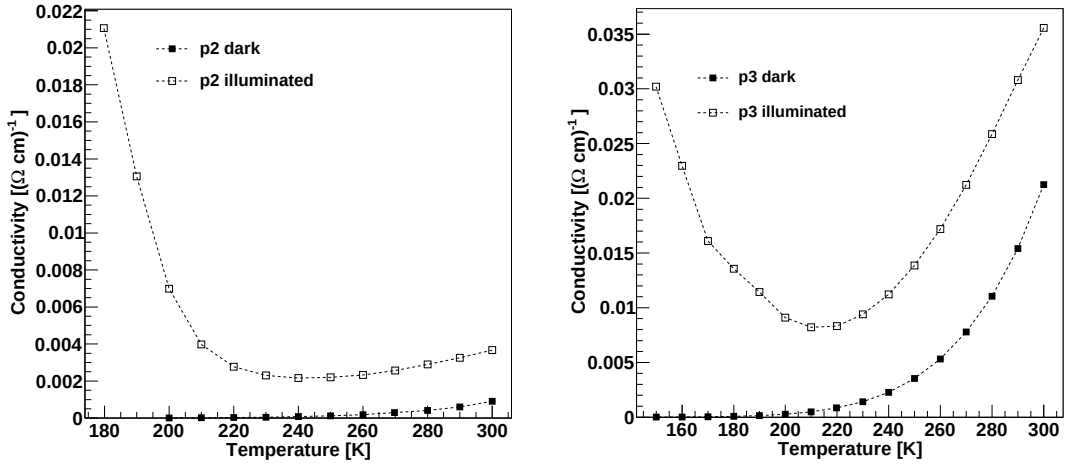

Figure 7.10: *Conductivity of samples p2 and p3 under illumination. At high temperatures, the photo induced carriers lead to a constant increase. At lower temperatures the conductivity grows due to growing mobility at a constant carrier density.*

Mobilities: Figure 7.9 gives an overview over the apparent mobilities. There is a maximum for p2 and p3 around 200K while, in contradiction to the assumption made above, the temperature dependence of the mobility values of p4 does not follow the behaviour of the other samples.

7.3.2 n-type $CuInSe_2$

Due to the significantly lower mobility of the holes compared to the electrons, the contribution of holes can be neglected, so that the equations for one path conduction are still valid. Comparing the electron densities and conductivity of the photo hall data to the measurements in the dark (figs. 7.11 and 7.12), one can clearly see that both increase by orders of magnitude so that the main contribution to the electrical transport comes from photo induced electrons. Consequently no temperature dependence is visible as the number of photo generated carriers in the $CuInSe_2$ layer is in first approximation independent of the temperature.

A look to the mobilities gives a more heterogeneous picture: For n2, the illumination does not significantly change the mobility. In both cases a clear trend in the temperature dependence cannot be observed. For n1 and n3 in contrast, the mobilities decrease with increasing temperature under illumination.

The behaviour of the mobility of sample n1 in the dark can be explained by limitation of the mobility by charged impurity scattering. Under illumination, the value of the mobilities is in the same order of magnitude, but from the temperature dependence one can conclude that now phonon scattering is dominating. This is astonishing as the parameters of phonon scattering are basic material parameters and should not be changed by the illumination. A change from charged impurity scattering to phonon scattering is therefore only possible by reducing the number of charged impurities and thus should go along with an increase of the mobility.

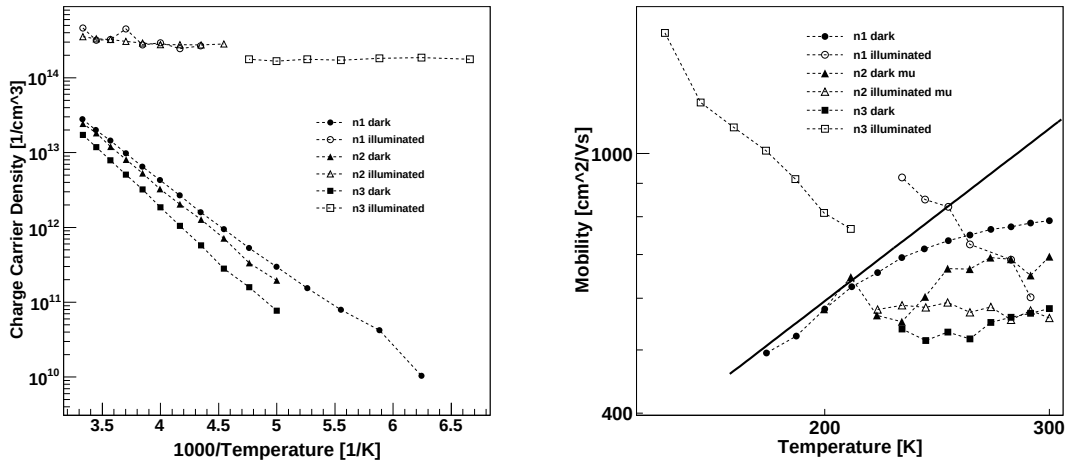

Figure 7.11: *Electron densities and mobilities of the n-type samples. The black solid line in the mobilities plot follows a $T^{3/2}$ dependence that would be expected for domination of charged impurity scattering.*

For sample n3, the mobility becomes significantly higher under illumination, supporting the theory of a reduction of charged defects. As the defect induced carriers under illumination only represent a small fraction of the total number of carriers, the data from charge carrier density or conductivity of the sample cannot be used to confirm this theory.

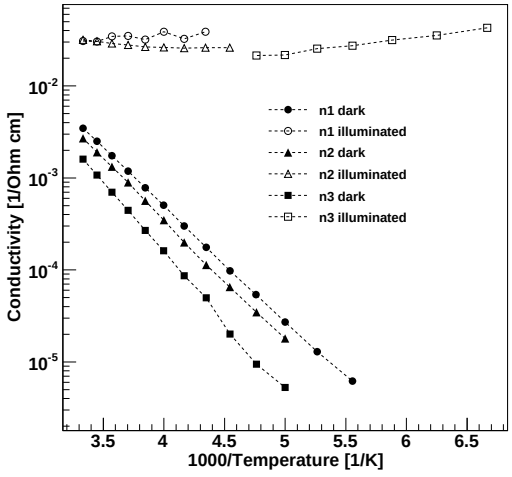

Figure 7.12: *Conductivity of the n-type samples.*

7.3.3 Mobility Spectra

In order to prove the existence of electrons in two different bands that resulted from the mobility spectra of p1B under illumination and p7 in the dark, B-field dependent measurements under illumination were also performed on the samples p2, p3, and n3. As already found for sample p1B, the quantitative results are not reliable. For example the

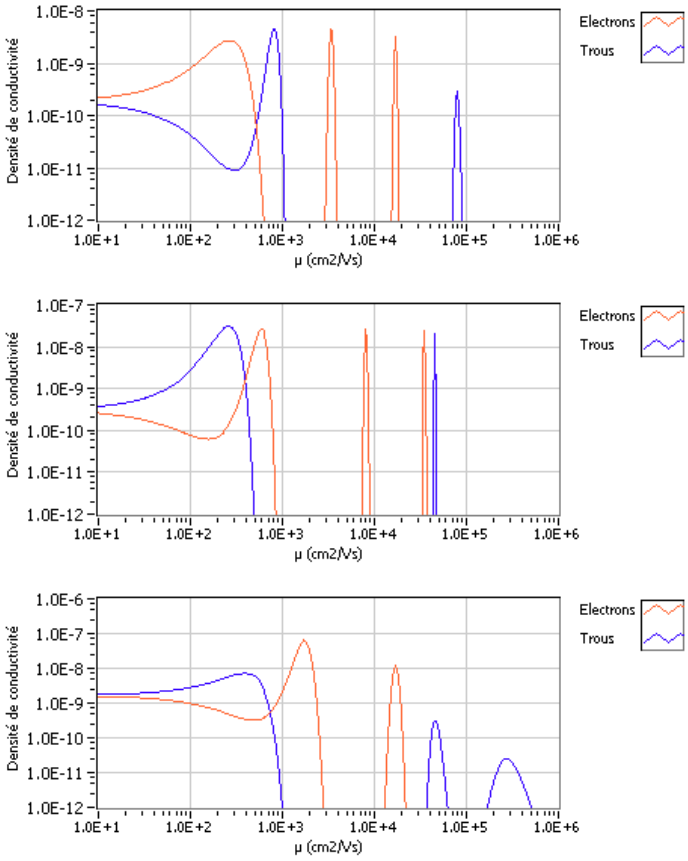

Figure 7.13: *Mobility spectra of the samples p2, p3 and n3 determined with MEMSA. The B-field dependent measurements were performed at 250 K.*

hole mobilities are again rather high compared to the values found in the dark. On the other hand, the qualitative results, especially the occurrence of one low mobility hole and two high mobility electrons are consistent for all samples and therefore can be expected to be a general property of $CuInSe_2$.

The data were taken at 250 K. An overview of the mobility spectra is shown in Figure 7.13, the mobilities, densities, and contributions to the conductivity are given in Table 7.2.

In contrast to the results of sample p1B, the contributions of the strongest hole and the strongest electron are in the same order of magnitude respectively for the three high activation energy samples. The reason can be found in the highly different defect induced carrier densities (see Chap. 6). For a sample with a higher defect induced carrier density, one can expect a lower contribution of the photo generated carriers to the total transport.

While the defect induced hole densities of p1B are around $1 \cdot 10^{17}\,\mathrm{cm}^{-3}$, sample p3 shows a hole density of $1.4 \cdot 10^{15}\,\mathrm{cm}^{-3}$ in the dark. The hole density in the dark of sample p2 is with $2.5 \cdot 10^{13}\,\mathrm{cm}^{-3}$ even lower. Consequently, the contribution of the defect induced carriers also is lower and the transport is dominated by the light induced carriers. Due to its higher mobility with respect to the hole, one of the light induced electrons delivers the strongest contribution.

	peaks separately			electrons vs. holes	
	$\mu\,[\mathrm{cm}^2/\mathrm{Vs}]$	$\sigma\,[(\Omega\mathrm{cm})^{-1}]$	n $[\mathrm{cm}^{-3}]$	$\sigma\,[(\Omega\mathrm{cm})^{-1}]$	σ/σ_{tot}
p2	$\mathbf{-2.6\cdot10^2}$	$\mathbf{8.9\cdot10^{-8}}$	$\mathbf{7.8\cdot10^{13}}$	$\sigma_{tot}=1.3\cdot10^{-7}$	
	$-3.3\cdot10^3$	$1.2\cdot10^{-8}$	$2.7\cdot10^{11}$	$\sigma_p=2.9\cdot10^{-8}$	21.3%
	$-1.7\cdot10^4$	$5.2\cdot10^{-9}$	$2.4\cdot10^{10}$	$\sigma_n=1.1\cdot10^{-7}$	78,7%
	$8.3\cdot10^2$	$2.8\cdot10^{-8}$	$2.8\cdot10^{12}$		
	$8.0\cdot10^4$	$7.0\cdot10^{-10}$	$6.9\cdot10^8$		
p3	$\mathbf{2.6\cdot10^2}$	$\mathbf{6.0\cdot10^{-7}}$	$\mathbf{3.1\cdot10^{14}}$	$\sigma_{tot}=8.7\cdot10^{-7}$	
	$-6.0\cdot10^2$	$2.3\cdot10^{-7}$	$3.3\cdot10^{13}$	$\sigma_p=6.0\cdot10^{-7}$	68.8%
	$-8.0\cdot10^3$	$4.2\cdot10^{-8}$	$3.3\cdot10^{11}$	$\sigma_n=2.7\cdot10^{-7}$	31.2%
n3	$\mathbf{-1.7\cdot10^3}$	$\mathbf{6.4\cdot10^{-7}}$		$\sigma_{tot}=1.1\cdot10^{-6}$	
	$-1.7\cdot10^4$	$4.7\cdot10^{-8}$		$\sigma_p=3.9\cdot10^{-7}$	36.6%
	$3.9\cdot10^2$	$3.9\cdot10^{-7}$		$\sigma_n=6.9\cdot10^{-7}$	63.7%
	$4.6\cdot10^4$	$1.5\cdot10^{-9}$			
	$2.7\cdot10^5$	$3.6\cdot10^{-10}$			

Table 7.2: *Overview of the observed charge carriers in p2, p3 and n3. For every peak in the mobility spectrum, the position, the corresponding conductivity and the carrier density is given. The main contribution for each temperature is highlighted. In the last two columns, the electron and hole contributions are summed up.*

Also for sample n3, the defect induced carrier density $n_{dark} = 1.9\cdot10^{12}\,\mathrm{cm}^{-3}$ is very low, so that the conductivity is dominated by the light induced electrons.

7.4 Summary

The change of the Hall coefficient to a negative value during photo Hall measurements shows that under illumination the influence of photo induced electrons is strong enough to require describing the electrical transport in $CuInSe_2$ by two or multiple band conduction. This makes it necessary to determine the B-field dependence of the Hall coefficient to be able to separate the contributions of the carriers from the different bands.

This result is in contradiction to the results for $CuGaSe_2$ ([Ris07] and Sec. 7.1). An explanation could be the different behaviour of light induced metastabilities in both materials. The (V_{Cu}−V_{Se}) divacancy for example is expected to switch immediately from a donor to an acceptor state for $CuGaSe_2$ under illumination. For $CuInSe_2$, an additional energy barrier keeps the defect in the donor state [Lan06]. The height of this barrier is, though, with approximately 0.1 eV so small that at room temperature it should not play a role.

An other explanation might be differences in the properties of the conduction band that could make conduction in the n-valley more favourable for $CuInSe_2$ than for $CuGaSe_2$. According to calculations from [Bot12], the effective electron masses are very similar. The LDA approach delivers masses of 0.23 m_e for both compounds, while the scGW approach leads to 0.13 m_e for $CuGaSe_2$and 0.16 m_e for $CuInSe_2$. The height of the barrier towards the conduction band minimum is 0.88 eV for $CuGaSe_2$and 0.74 eV for $CuInSe_2$. The differences

between both compounds are rather small and would not explain that the effect occurs in $CuInSe_2$ while it does not in $CuGaSe_2$.

Further investigations on the second electron, especially a more precise determination of the mobility and the temperature dependence is necessary to understand this effect.

The quantitative interpretation of mobility spectrum analysis turned out to be difficult so that neither precise values for mobilities and carrier densities nor temperature dependencies can be given. Nevertheless, it showed qualitatively, that one low mobility hole and two high mobility electrons contribute to electrical transport in $CuInSe_2$. The second electron contribution probably originates from a second valley in the conduction band at the N-point. The barrier between this local minimum and the conduction band minimum is 0.74 eV and recombination to the valence band maximum would also require a large transition in k space from the N- to the Γ-point. Recombination to the N-point of the valence band are also possible but suppressed due to the lower density of free states in the valence band.

The temperature dependence of the Hall coefficients can be explained qualitatively. For performing a conclusive fit, the data does not cover a sufficient temperature range. At low temperatures, sample p4 is in a state where transport is dominated by photo induced carriers (the curve becomes nearly level), but just reaches the beginning of the transition to defect dominated behaviour. Samples p2 and p3 are inside this transition and reach neither state.

Chapter 8

Conclusions and Outlook

The aim of this thesis was to bring some more light into the electrical properties of $CuInSe_2$ thin films. As the focus was on the bulk properties, exclusively epitaxially grown layers were analysed. Photo Hall measurements on $CuInSe_2$ were the first time performed within this thesis. One of the observed p-type samples originates from the Helmholtz Zentrum Berlin, all other samples – six other p-type, three n-type and one $CuGaSe_2$ sample – were grown at the University of Luxembourg.

Measuring the magnetic field dependence of the Hall voltage was found to be a fast and convincing technique to distinguish between single band (linear B-field dependence of U_H, constant R_H) and multiple band conduction (nonlinear B-field dependence of U_H, B-field dependent R_H).

Measurements on $CuGaSe_2$

The results of a previous study [Ris07, Sie08] lead to the assumption, that transport in epitaxial $CuGaSe_2$ thin film layers under illumination can be described by one band conduction. Changes in the free hole density were explained by light induced changes in the behaviour of a metastable compensating donor. Within this thesis it could be shown that the assumption of single band conduction is valid under typical experimental conditions.

Measurements on $CuInSe_2$

In contrast to $CuGaSe_2$, $CuInSe_2$ can be doped both p- and n-type. Consequently, the production of highly compensated samples with $N_A \approx N_D$ also is possible. Three samples of this type, showing low defect induced carrier densities and thus comparably low conductivities (samples p5-p7) were studied in this work. Free charge carriers in those samples mainly originate from band to band excitation and hence electrons and holes both are present. In that case, a description by single band conduction is not valid even without illumination.

A proof for the presence of different carrier types is the magnetic field dependence of the Hall coefficient in measurements in the dark, which could be shown for those samples. On the other hand, the magnetic field dependence disappears not only in case of single band conduction but also for the low B-field approximation $\mu B \ll 1$. Thus, in case of

magnetic field dependent Hall coefficients, one can estimate a minimum mobility for the highest mobility carriers in the material: The highest B-field used for the measurements was 5 T= $5 \cdot 10^{-4}$ Vs/cm^2. Therefore one can conclude that carriers with a mobility of at least the order of magnitude of $\frac{1}{B} = 2 \cdot 10^3$ cm^2/Vs are present.

Measurements on samples with higher defect induced carrier densities grown in Luxembourg revealed acceptor activation energies around $E_a = 200$ meV for the p-type samples and donor activation energies around $E_d = 230$ meV for n-type $CuInSe_2$.

Shallower acceptor levels of 18 meV and 110 meV could be found in sample p1B which was not produced in Luxembourg.

The large differences in the free carrier densities and activation energies in the dark between the sample p1B (high hole density, low acceptor activation energy) on one side and the samples grown in Luxembourg (lower defect densities, high defect activation energy) on the other side can most likely be attributed to different compensation levels: The samples from Luxembourg are strongly compensated so that all shallow defect states are already occupied due to the compensation and thus can not provide free charge carriers. This also leads to a lower total free hole density.

A correlation of the transport properties and composition or growth conditions could not clearly be found. From the photoluminescence spectra one can see a trend of lower copper to indium ratios during layer growth in the intrinsic samples. An EDX study of the bulk properties of the samples (Tab. A.2) could not confirm this because the deviations did not follow a clear trend and were all inside the error of the device.

The photo Hall experiments on $CuInSe_2$ showed, that under illumination, p-type $CuInSe_2$ thin film layers experience strong contributions of electrons to the electrical transport. This was observed in all of the p-type samples although the defect induced hole densities of the samples varied over several orders of magnitude.

From the magnetic field dependence of the Hall coefficient one can get information on the charge carriers contributing to the electrical transport. A tool for this is the mobility spectrum analysis, a method that delivers charge carrier mobilities and densities of the different carrier types without the need of providing previous assumptions (e.g. on the number of different carrier types) for the analysis.

The resulting mobility spectra show one low mobility hole contribution and two high mobility electron contributions. The second electron contribution probably originates from electrons in a second valley in the conduction band of $CuInSe_2$, located at the N-point of the Brillouin zone.

Outlook

The experimental data taken in the dark could be modelled theoretically, while the results from photo Hall measurements could be described qualitatively but not quantitatively. It certainly would be a large step ahead to adapt the model to those data. In order to do so, an extended temperature range for the measurements would be helpful. The low temperature data could for example help to determine the photo induced carrier density, while at high temperatures, data from the defect depletion range or from larger ranges with one dominating activation energy would give more detailed information on activation energies or defect densities. Thus the number of free parameters could be reduced.

This work aimed at investigating properties of different sample types with a large range of electronic properties. This made it necessary to define standard parameters for the data acquisition. It is possible that the temperature range of the measurements could be extended to low temperatures, if more attention is paid to the special needs of the particular sample, like relaxation times at low temperatures.

Thus, a closer investigation of the second electron contribution would be possible. It would be very interesting to find precise values for the mobility and to see how they react to changes of the temperature.

The study showed significant differences between the behaviour of $CuGaSe_2$ and $CuInSe_2$. Therefore, conclusions on the behaviour of $Cu(In,Ga)Se_2$ are hardly possible, which makes it necessary to perform photo Hall measurements on $Cu(In,Ga)Se_2$ with different gallium to indium ratios. Measurements on $Cu(In,Ga)Se_2$ certainly will be even more challenging than on the ternary compounds $CuInSe_2$ and $CuGaSe_2$ because of possible local fluctuations in the Ga to In ratio. However, the fact that the best chalcopyrite solar cells have a $Cu(In,Ga)Se_2$ absorber, makes it desirable to understand the properties of this material better.

Appendix A

Samples

This work contains data from measurements on eleven samples. An overview is given in Table A.1. The original name is the name of the MOVPE process. If more than one sample for Hall measurements was cut from the wafer, this name is enhanced by a lowercase letter.

Name	Origin	Original Name	T	Run		Thickness
			[°C]	dark	illum.	[nm]
p1B	HZB	CISe055c	500	365	269	650
p2	UL	CISe_epi_063	470	786	837	650
p3	UL	CISe_epi_065	470	821	822	620
p4	UL	CISe_epi_111	470	923	950	480 (-680)
p5	UL	CISe_epi_113b	470	907	-	200 (-730)
p6	UL	CISe_epi_109	470	943	-	700
p7	UL	CISe_epi_152b	470	997	-	790
n1	UL	CISe_epi_088	470	818	819	610 (-970)
n2	UL	CISe_epi_090	470	748	882	680 (-900)
n3	UL	CISe_epi_092	470	696	697	700
CGS	UL	CGSe_epi_109	520	1059	1061	770

Table A.1: *Overview of samples discussed in this work. The origin of the samples is either the University of Luxembourg (UL) or the Helmholtz Zentrum Berlin (HZB). T is the substrate temperature during growth.*

Table A.2 contains the results of EDX measurements on the samples. The samples were edged before the measurements to remove Cu_2Se. The results thus describe the bulk properties of the layers.

Thicknesses were determined from the SEM cross section pictures that are shown in Figures A.1 and A.2. The reading error was estimated to be ±20 nm. Some of the samples (p4, p5, n1, n2) show large fluctuations in the thickness. Top view images of the samples show that those structures cover the whole sample (see example of p4 in Table A.1), so that the thickness available for charge transport is reduced to the layer thickness in the valleys. The thickness of the mountains in between is given in parentheses.

The cross sections were not taken from the samples used for the electrical measurements but from other parts of the wafers from the corresponding MOVPE process.

Name	Cu	Se	In	Cu/In	Se/Cu+In	Se/Cu	Se/In
p1B*	23.0	45.8	23.2	0.99	0.99	1.99	1.98
p2	24.5	49.5	26.1	0.94	0.98	2.02	1.90
p3	24.3	49.8	25.8	0.94	0.99	2.05	1.93
p4	24.6	49.5	25.9	0.95	0.98	2.01	1.91
p5†	20.0	46.4	16.5	1.21	1.27	2.33	2.81
p6	24.6	49.9	25.5	0.96	1.00	2.03	1.96
p7	24.1	50.0	26.0	0.93	1.00	2.08	1.93
n1	24.5	49.6	25.9	0.94	0.99	2.02	1.92
n2	24.2	49.4	26.5	0.91	0.98	2.04	1.87
n3	24.5	49.4	26.0	0.94	0.98	2.01	1.90
CGS‡	24.9	51.6	23.5	1.06	1.06	2.07	2.19

*: Oxygen: 8.0%

†: Ga: 9.4%, As: 7.8% from GaAs substrate

‡: Ga replaces In

Table A.2: *EDX study: Percentages of atoms inside the layers.*

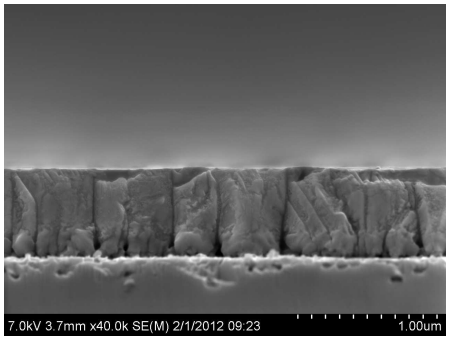

p1B

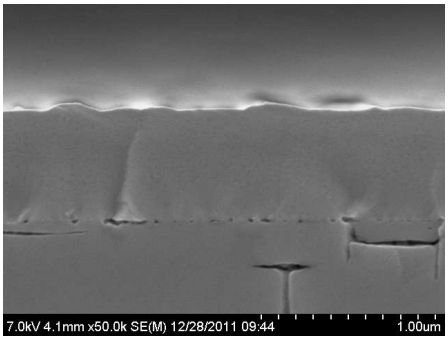

p2

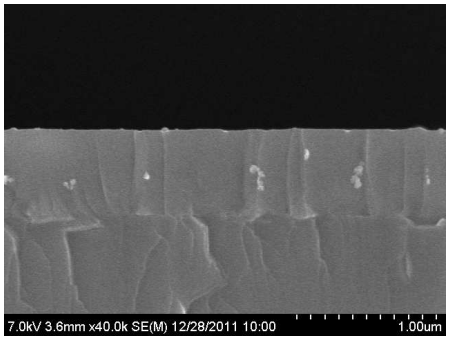

p3

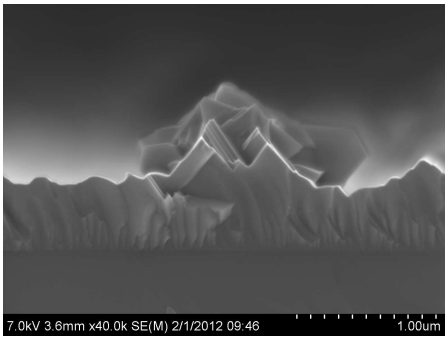

p4

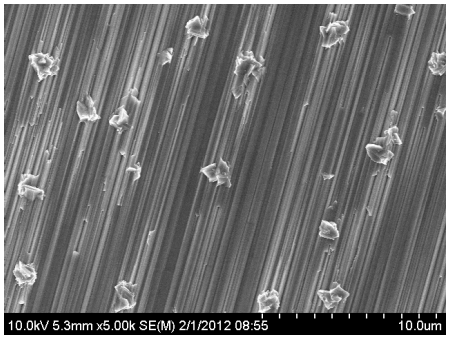

p4 top view

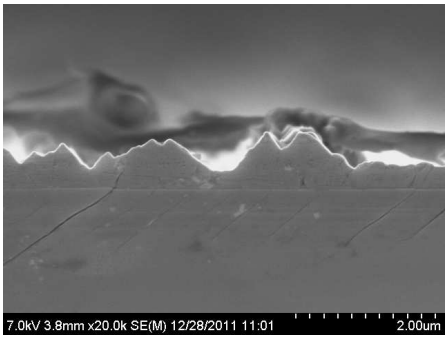

p5

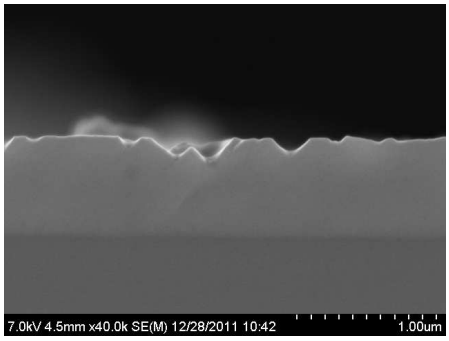

p6

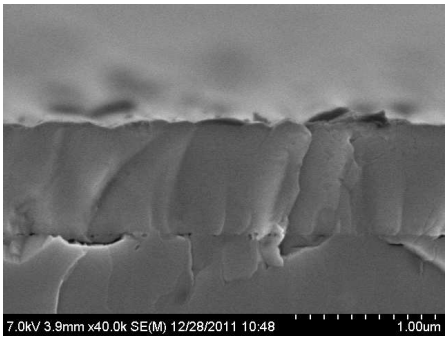

p7

Figure A.1: *Cross sections of the p-type layers*

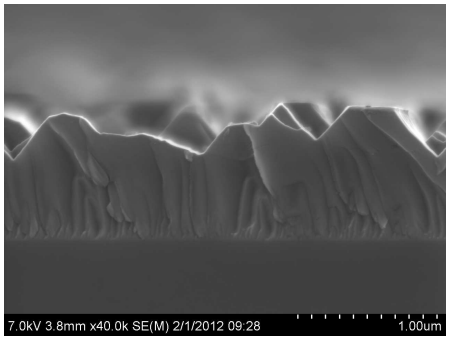

n1

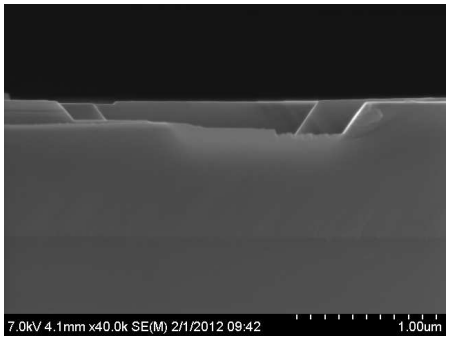

n2

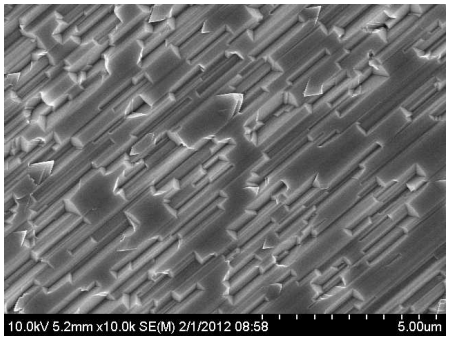

n2 top view

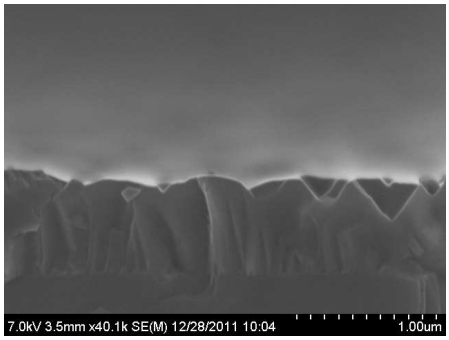

n3

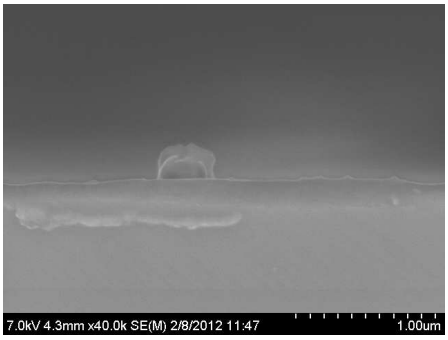

CGS

Figure A.2: *Cross sections of the n-type and $CuGaSe_2$ layers*

Appendix B

Constants and Symbols

B.1 Constants

a_B	$5.29177 \cdot 10^{-11}$ m	Bohr Radius
ϵ_0	$8.8542 \cdot 10^{-12}$ Fm^{-1}	Vacuum Permittivity
e	$1.6022 \cdot 10^{-19}$ C	Electron Charge
h	$6.6262 \cdot 10^{-34}$ Js	Planck Constant
$\hbar$	$1.0546 \cdot 10^{-34}$ Js	$\frac{h}{2\pi}$
k_B	$1.3807e-23\text{JK}^{-1}$	Boltzmann Constant
m_e	$9.1095 \cdot 10^{-31}$ kg	Free Electron Mass

B.2 Symbols

A	Sample Cross Section
$\vec{B}$	Magnetic Field
D	Optical Deformation Constant
$D_{C,V}(E)$	Density of States in the Conduction or Valence Band
d	Sample Thickness
$\vec{E}$	Electric Field
E_A	Acceptor Energy Level
E_a	Acceptor Activation Energy
E_{ac}	Acoustic Deformation Potential Constant
E_C	Conduction Band Minimum
E_D	Donor Energy Level
E_d	Donor Activation Energy
E_F	Fermi Level
E_G	Band Gap Energy
e_{pz}	Piezoelectric Constant
E_V	Valence Band Maximum
ϵ_r	Static Relative Permittivity, Dielectric Constant
ϵ_∞	High Frequency Relative Permittivity

$\vec{F}$	Field Force
I	Current
$\vec{j}$	Current Density
k	Momentum
l	Length
m_e^*	Effective Electron Mass
m_h^*	Effective Hole Mass
m_{ij}^*	Effective Mass tensor
μ	Charge Carrier Mobility
μ_{AC}	Mobility from Acoustic Phonon Scattering
μ_{BH}	Mobility from Ionised Impurity Scattering
μ_{GB}	Mobility from Grain Boundaries
μ_N	Mobility from Neutral Impurity Scattering
μ_{NPO}	Mobility from Optical Phonon Scattering
μ_{PO}	Mobility from Polar Optical Phonon Scattering
μ_{PZ}	Mobility from Piezoelectric Scattering
n	Free Electron Density
$N_{A,D}$	Defect Density
$N_{C,V}$	Effective Density of States in the Conduction or Valence Band
ν	Frequency of Light
p	Free Hole Density
Φ	Barrier Height at Grain Boundary
Φ_0	Incident Photon Flux
Φ_T	Transmitted Photon Flux
q	Electric Charge
R	Resistance
R_H	Hall Coefficient
ρ	Resistivity
ρ	Density
σ	Conductivity
σ_i	Scattering Cross Section
$\underline{\sigma}$	Conductivity Tensor
$\sigma_\square$	Sheet Conductivity
T	Transmission
τ	Relaxation Time
Θ	Typical Temperature of the Phonons
U	Voltage
$\vec{v}$	Velocity
v_d	Drift Velocity
v_s	Velocity of Sound

B.3 Values for $CuInSe_2$

ϵ_r	9.30	[Irie79]
	13.6	[Was86]
ϵ_∞	6.15	[Irie79]
	8.1	[Was86]
Θ	395 K	[Irie79]
ρ	$5.81\,\mathrm{g/cm^3}$	[Irie79]
v_s	$2.75 \cdot 10^5\,\mathrm{cm/s}$	[Irie79]

p-Type

D	12 eV	[Irie79]
E_{ac}	7 eV	[Irie79]
m_h^*	$0.73 \cdot m_e$	[Irie79]
	$0.71 \cdot m_e$	[Bod82]

n-Type

D	23 eV	[Irie79]
E_{ac}	13 eV	[Irie79]
m_e^*	$0.09 \cdot m_e$	[Irie79]
	$0.092 \cdot m_e$	[Bod82]

Appendix C

Source Code for Simulations

In this chapter, the most important routines for the simulation of charge carrier densities and mobilities are presented. They are written in the C++ based data analysis framework ROOT [Bru97].

C.1 Charge Carrier Statistics

This binary search algorithm is taken from [Ris07] and calculates for known defect densities (`N_A1, N_A2, N_D`), activation energies (`E_A1, E_A2, E_D`), band gap (`EG`), and temperature (`T`) the Fermi energy (`EF`), the densities of charged defects (`NA1minus, NA2minus, NDplus`), and the densities of free carriers (`p_theo, n_theo`). This example describes two acceptors and one donor but can easily be enhanced by an arbitrary number of additional defects. Changes from the original version were mainly made to translate it from C to C++.

```
const Double_t  g       = 2.;
const Double_t  k_B     = 8.617343e-5; //[eV/K]
Double_t EFmax = EG;  // upper frontier: conduction band minimum
Double_t EFmin = 0.0; // lower frontier: valence band maximum
Double_t charge;
// after k iterations: accuracy is EG * (0.5^k)
for(Int_t k = 0; k < 15; k++ )
{ // set start value for E_F
  EF        = (EFmax + EFmin) / 2.;
  // Number of charged acceptors A1 and A2 and of charged donors
  NA1minus = N_A1 / (1. + g * exp((E_V + E_A1 - EF) / (k_B * T)));
  NA2minus = N_A2 / (1. + g * exp((E_V + E_A2 - EF) / (k_B * T)));
  NDplus   = N_D  * (1. - (1./(1. + (1./g)
                          * exp((E_C - E_D - EF) / (k_B * T)))));
  //Boltzmann approximation for free holes and electrons
  p_theo   = calcN_V(T) * exp( - (EF - E_V) / (k_B * T));
  n_theo   = calcN_C(T) * exp( - (E_C - EF) / (k_B * T));
  //charge of the material
  charge   = (NDplus) - (NA1minus + NA2minus) + (p_theo - n_theo);
  //if positive increase lower frontier else decrease upper frontier
  if (charge >  0.0) EFmin = EF; if (charge <= 0.0) EFmax = EF;
}
```

The densities of state of the valence and conduction band ($|N_V, N_C|$) were calculated from the effective hole and electron masses ($|m_h, m_{e_{eff}}|$) as follows:

```
const Double_t m_e     = 9.1095e-31;        // [kg]
const Double_t pi      = 3.141593;
const Double_t h       = 6.6262e-34;        // [Js]
const Double_t m_h     = 0.7 * m_e;
const Double_t m_e_eff = 0.09 * m_e;
const Double_t k_B     = 1.3807e-23;        // [J/K]

Double_t calcN_V(Double_t T)
{
  return 2 * sqrt(pow(2 * pi * m_h * k_B * T/(h * h), 3)
                  )/1000000;    // [cm^(-3)]
}

Double_t calcN_C(Double_t T)
{
  return 2 * sqrt(pow(2 * pi * m_e_eff * k_B * T/(h * h), 3)
                  )/1000000;    // [cm^(-3)]
}
```

C.2 Mobilities

The mobilities resulting from the different scattering mechanisms are calculated with the following routines. All mobilities are calculated in cm^2/Vs, densities and energies are transferred from the main program in cm^{-3} and eV respectively. Constants are mostly given in SI units, so that some conversion factors are necessary.

Constants needed for the calculation of the mobilities

```
const Double_t k_B         = 1.3807e-23;     //[J/K]
const Double_t ElemCharge  = 1.6022e-19;     //[C]
const Double_t pi          = 3.141593;
const Double_t m_e         = 9.1093897e-31; //[kg]
const Double_t h           = 6.6262e-34;     //[Js]
const Double_t hbar        = h/(2. * pi);    //[Js]
const Double_t epsilon     = 8.8542E-12;
const Double_t theta       = 395;            //[K]
const Double_t rho_CISe    = 5770;           //[kg * m(-3)]
const Double_t epsilon_0   = 13.6;
const Double_t m_h = 0.7;      //in units of the free electron mass
const Double_t m_e = 0.09;     //in units of the free electron mass
```

Calculation of mobilities

```
Double_t calcMobility_npo(Double_t T,Double_t m_h)
{
  const Double_t D    = 6.8e8; //[eV/cm]
  const Double_t D_SI = D * ElemCharge * 100;

  Double_t F      = exp(5.44 * (1./sqrt(T/theta) - 1.));
  Double_t mu_npo = 4. * sqrt(2. * pi) * ElemCharge * hbar * hbar
                  * rho_CISe * sqrt(k_B * theta)
                  * F/(3. * sqrt(pow(m_h * m_e, 5.)) * D_SI * D_SI)
                  * 10000.;

  return mu_npo;
}

Double_t calcMobility_N(Double_t T, Double_t N_V,Double_t ptheo,
      Double_t N_A1, Double_t E_A1,Double_t N_A2, Double_t E_A2,
      Double_t N_N, Double_t E_F,Double_t m_h)
{
  const Double_t g_1 = 2.0;
  const Double_t g_2 = 2.0;
  const Double_t E_g = 1.0;  //[eV]
  Double_t a_B;
  Double_t N_x;
  Double_t mu_N;

  E_A2 = E_A2 * ElemCharge;
  E_A1 = E_A1 * ElemCharge;
  E_F  = E_F  * ElemCharge;
  N_A1 = N_A1 * 1000000.;
  N_A2 = N_A2 * 1000000.;
  N_V  = N_V  * 1000000.;

  a_B  = epsilon * epsilon_0 * hbar
       * hbar/(m_e * m_h * ElemCharge * ElemCharge);
  N_x  = N_A1/(1. + (1./g_1) * exp((E_F - E_A1)/(k_B * T)))
       + N_A2/(1. + (1./g_2) * exp((E_F - E_A2)/(k_B * T))) + N_N;
  mu_N = ElemCharge/(20 * a_B * hbar * N_x) * 10000;

  return mu_N;
}
```

```
Double_t calcMobility_BH(Double_t T, Double_t N_V, Double_t ptheo,
      Double_t N_D, Double_t N_A1, Double_t E_A1, Double_t N_A2,
      Double_t E_A2, Double_t N_N, Double_t E_F, Double_t m_h)
{
  const Double_t g_1 = 2.0;
  const Double_t g_2 = 2.0;
  Double_t N_x;
  Double_t NI;
  Double_t beta;
  Double_t f_of_beta;
  Double_t mu_BH;
  E_A2  = E_A2 * ElemCharge;
  E_A1  = E_A1 * ElemCharge;
  E_F   = E_F  * ElemCharge;
  N_D   = N_D  * 1000000.;
  N_A1  = N_A1 * 1000000.;
  N_A2  = N_A2 * 1000000.;
  N_V   = N_V  * 1000000.;
  ptheo = fabs(ptheo);

  N_x  = N_A1/(1. + (1./g_1) * exp((E_F - E_A1)/(k_B * T)))
       + N_A2/(1. + (1./g_2) * exp((E_F - E_A2)/(k_B * T))) + N_N;
  NI   = N_A1 + N_A2 - N_x + N_D + N_N;
  if (NI == 0) NI = 1;
  beta  = 2. * sqrt(6.) * k_B * T/(ElemCharge * hbar)
       * sqrt(m_h * m_e * epsilon_0 * epsilon/(ptheo * 1000000.));
  f_of_beta = log(1. + beta * beta)
       - beta * beta/(1. + beta * beta);
  mu_BH = pow(2, 7./2.) * pow(4. * pi * epsilon_0 * epsilon, 2)
       * pow(k_B * T, 3./2.)/(pow(pi, 3./2.)
         * pow(ElemCharge, 3.) * pow(m_h * m_e, 1./2.)
         * NI * f_of_beta) * 10000;
  return mu_BH;
}

Double_t calcMobility_ac(Double_t T, Double_t m_h)
{
  const Double_t velo = 2.18e3;              //[m/s]
  const Double_t E_ac = 6.5 * ElemCharge; //[eV*C]
  return (2. / 3.) * (sqrt(2. * pi) * ElemCharge * pow(hbar, 4.)
       * rho_CISe * velo * velo)/(E_ac * E_ac
         * pow(sqrt(m_e * m_h),5.) * pow(sqrt(k_B * T), 3.)) * 1.e4;
}

Double_t calcMobility_po(Double_t T, Double_t m_h)
{
  const Double_t epsilon_inf=8.1;
  Double_t Z     = theta / T;
  Double_t G     = 0.48 * exp(0.18 * Z);
  Double_t mupo1 = (sqrt(T) / (pow(sqrt(m_h), 3.) * theta));
  Double_t mupo2 = (1. / (1. / epsilon_inf  -  1. / epsilon_0));
  Double_t mupo3 = (exp(Z) - 1);
  return 25.4 * mupo1 * mupo2 * mupo3 * G;
}
```

Appendix D

Mobility Spectrum Analysis

The transformation from Equation (3.44) to Equation (3.46) can readily be understood in a descriptive way. [Beck87] has shown he validity of this transformation. This chapter follow his calculations.

The elements of the conductivity tensor are given by Equation (3.44)

$$\sigma_{xx}(B) = \frac{en\mu}{1+(\mu B)^2} \tag{D.1a}$$

$$\sigma_{xy}(B) = \frac{en\mu^2 B}{1+(\mu B)^2} \tag{D.1b}$$

In the general case R_H and ρ depend on the magnetic Field. McClure [McCl56] has derived the elements of the conductivity tensor by solving the Boltzmann equation under the assumption of an energy dependent relaxation time τ. For a single band, he obtains with f_0 the equilibrium distribution function:

$$\sigma_{xx} = \left(\frac{e^2}{(2\pi)^3}\right) \int d^3k \left(-\frac{\partial f_0}{\partial E}\right) \tau \sum_{i=1}^{\infty} \frac{|B(i-1)|^2 + |B(-i-1)|^2}{1+(i\omega_c\tau)^2} \tag{D.2}$$

and if the $k_x k_z$ plane is a mirror plane

$$\sigma_{xy} = \left(\frac{e^2}{(2\pi)^3}\right) \int d^3k \left(-\frac{\partial f_0}{\partial E}\right) \tau \sum_{i=1}^{\infty} \frac{i\omega_c\tau[|B(i-1)|^2 + |B(-i-1)|^2]}{1+(i\omega_c\tau)^2} \tag{D.3}$$

By introducing the effective mass m^*, the cyclotron mobility μ^*, the cyclotron frequency ω_c, and a set of conductivity density functions η_i^+ and η_i^-

$$\omega_c(n,E,k_z) = \frac{e}{m_c(n,E,k_z)} \cdot B \tag{D.4}$$

$$\mu^*(n,E,k_z) = \frac{e\cdot\tau(n,E,k_z)}{m_c(n,E,k_z)} \tag{D.5}$$

$$\eta_i^{\pm}(n,E,k_z) = \frac{e}{(2\pi)^3}\left(-\frac{\partial f_0}{\partial E}\right) m_c(n,E,k_z)\mu^*(n,E,k_z)|B(\pm i-1)|^2 \tag{D.6}$$

equations (D.2) and (D.3) can be written as:

$$\sigma_{xx} = \sum_n \int d^3k \sum_{i=1}^{\infty} \frac{\eta_i^+ + \eta_i^-}{1 + (i\mu^* B)^2} \tag{D.7a}$$

$$\sigma_{xy} = \sum_n \int d^3k \sum_{i=1}^{\infty} \frac{i\mu^* B(\eta_i^+ + \eta_i^-)}{1 + (i\mu^* B)^2} \tag{D.7b}$$

Finally, $\eta_i^{\pm}$ can be substituted by another conductivity density function $s(\mu)$

$$s(\mu) = \begin{cases} S^+(\mu), & (\mu > 0) \\ S^-(|\mu|), & (\mu < 0) \end{cases} \qquad \text{with} \tag{D.8}$$

$$S^{\pm}(\mu) = \sum_n \sum_{i=1}^{\infty} \int d^3k \eta_i^{\pm} \cdot \delta[\mu - i\mu^*] \tag{D.9}$$

so that (D.2) and (D.3) can be written as Equation (3.46)

$$\sigma_{xx}(B) = \int_{-\infty}^{\infty} \frac{s(\mu)d\mu}{1 + (\mu B)^2} \tag{D.10a}$$

$$\sigma_{xy}(B) = \int_{-\infty}^{\infty} \frac{\mu B s(\mu)d\mu}{1 + (\mu B)^2} \tag{D.10b}$$

Bibliography

[Agu11] I. Aguilera, J. Vidal, P. Wahnon, L. Reining, and S. Botti. First-principles study of the band structure and optical absorption of CuGaS(2). *Physical Review B*, 84(8), Aug 2011.

[Aru92] E. Arushanov, L. Essaleh, J. Galibert, J. Leotin, M.A. Arsene, J.P. Peyrade, and S. Askenazy. Shubnikov-de Haas Oscillations in N-$CuInSe_2$. *Applied Physics Letters*, 61(8):958–960, Aug 1992.

[Bar50] J. Bardeen and W. Shockley. Deformation potentials and mobilities in non-polar crystals. *Physical Review*, 80(1):72–80, Oct 1950.

[Beck87] W.A. Beck and J.R. Anderson. Determination of electrical transport properties using a novel magnetic field dependent Hall technique. *Journal of Applied Physics*, 62(2):541–544, Jul 1987.

[Bla85] J.S. Blakemore. *Solid State Physics*. Cambridge University Press, Cambridge, 2nd edition, 1985.

[Bod82] I.V. Bodnar and A.P. Bologa. Investigation of the $CuGa_xIn_{1-x}Se_2$ Solid-Solutions. *Crystal Research and Technology*, 17(3):339–344, 1982.

[Bot12] S. Botti, 2012. Université Lyon, unpublished.

[Bro51] H. Brooks. Scattering by Ionized Impurities in Semiconductors. *Physical Review*, 83:879, 1951.

[Bru97] R. Brun and F. Rademakers. ROOT - An object oriented data analysis framework. *Nuclear Instruments & Methods in Physics, Research Section A*, 389(1-2):81–86, Apr 1997. 5th International Workshop AIHENP 96, Lausanne, Switzerland, Sep 1996.

[Cham07] C. H. Champness, T. Cheung, and I. Shih. Room temperature transport measurements on Bridgman-grown p-type $CuIn_{1-x}Ga_xSe_2$. *Solar Energy Materials and Solar Cells*, 91(9):791–800, May 2007.

[Cie09] Test analysis done by Lakeshore, USA, contact via Detlef Cieslikowski, Cryophysics GmbH, Darmstadt, Germany. Dec 2009.

[Erg50] C. Erginsoy. Neutral Impurity Scattering in Semiconductors. *Physical Review*, 79:1013, 1950.

[Ger00] A. Gerhard. *Elektrische Defektspektroskopie an CuGaSe2 und verwandten Halbleiterdünnschichten*. PhD thesis, Freie Universität Berlin, Hahn-Meitner-Institut, Dec 2000.

[God00] T. Godecke, T. Haalboom, and F. Ernst. Phase equilibria of Cu-In-SeI. Stable states and nonequilibrium states of the In2Se3-Cu2Se subsystem. *Zeitschrift für Metallkunde*, 91(8):622–634, Aug 2000.

[Gre11] M.A. Green, K. Emery, Y. Hishikawa, W. Warta, and E.D. Dunlop. Solar cell efficiency tables (Version 38). *Progress in Photovoltaics*, 19(5):565–572, Aug 2011.

[Gue10] L. Guetay, C. Lienau, and G.H. Bauer. Subgrain size inhomogeneities in the luminescence spectra of thin film chalcopyrites. *Applied Physics Letters*, 97(5), Aug 2010.

[Hal1879] E.H. Hall. On a new action of the magnet on electric currents. *American Journal of Mathematics*, 2:287–292, 1879.

[Irie79] T. Irie, S. Endo, and S. Kimura. Electrical Properties of p- and n-Type $CuInSe_2$Single Crystals. *Japanese Journal of Applied Physics*, 18(7):1303–1310, 1979.

[Jac11] P. Jackson, D. Hariskos, E. Lotter, S. Paetel, R. Wuerz, R. Menner, W. Wischmann, and M. Powalla. New world record efficiency for Cu(In,Ga)Se(2) thin-film solar cells beyond 20%. *Progress in Photovoltaics*, 19(7, SI):894–897, NOV 2011. 25th EU PVSEC/5th WCPEC-5, Valencia, Spain, 2010.

[Key03] B.M. Keyes, P. Dippo, W.K. Metzger, J. AbuShama, and R. Noufi. Changes in the dominant recombination mechanisms of polycrystalline Cu(In,Ga)Se-2 occurring during growth. *Journal of Applied Physics*, 94(9):5584–5591, Nov 1 2003.

[Kia02] S. Kiatgamolchai, M. Myronov, O.A. Mironov, V.G. Kantser, E.H.C. Parker, and T.E. Whall. Mobility spectrum computational analysis using a maximum entropy approach. *Physical Review E*, 66(3, Part 2b), Sep 2002.

[Kit06] C. Kittel. *Einführung in die Festkörperphysik*. Oldenbourg, München, Germany, 14th edition, 2006.

[Lan05] S. Lany and A. Zunger. Anion vacancies as a source of persistent photoconductivity in II-VI and chalcopyrite semiconductors. *Physical Review B*, 72(3), Jul 2005.

[Lan06] S. Lany and A. Zunger. Light- and bias- induced metastabilities in Cu(In,Ga)Se_2 based solar cells caused by the (V-Se-V-Cu) vacancy complex. *Journal of Applied Physics*, 100(11), Dec 2006.

[Lar11] J.K. Larsen. *Inhomogeneities in Epitaxial Chalcopyrites Studied by Photoluminescence*. PhD thesis, Université du Luxembourg, Oct 2011.

[McCl56] J.W. McClure. Field Dependence of Magnetoconductivity. *Physival Review*, 101:1642–1646, 1965.

[Mig75] P. Migliorato, J.L. Shay, H.M. Kasper, and S. Wagner. Analysis of Electrical and Luminescent Properties of $CuInSe_2$. *Journal of Applied Physics*, 46(4):1777–1782, 1975.

[Neu78] H. Neumann, N. VanNam, H.J. Hobler, and G. Kuhn. Electrical Properties of n-Type $CuInSe_2$ Single Crystals. *Solid State Communications*, 25(11):899–902, 1978.

[Neu79] H. Neumann, R.D. Tomlinson, E. Nowak, and N. Avgerinos. Electrical Properties of p-Type $CuInSe_2$ Single Crystals. *Physica Status Solidi A – Applied Research*, 56(2):K137–K140, 1979.

[Neu90] H. Neumann and R.D. Tomlinson. Relation Between Electrical Properties and Composition in $CuInSe_2$ Single Crystals. *Solar Cells*, 28(4):301–313, May 1990.

[Nou84] R. Noufi, R. Axton, C. Herrington, and S.K. Deb. Electronic Properties versus Composition of Thin Films of $CuInSe_2$. *Applied Physics Letters*, 45(6):668–670, 1984.

[Org04] K. Orgassa. *Coherent optical Analysis of the ZnO/CdS/Cu(In,Ga)Se_2 Thin Film Solar Cell*. Shaker-Verlag, Aachen, Germany, 2004.

[Pan75] J.I. Pankove. *Optical processes in semiconductors*. Dover publications, 1975.

[Pau58] L.J. van der Pauw. A method of measuring specific resistivity and Hall effect of discs of arbitrary shape. *Philips Research Reports*, 13:1, 1958.

[Per08] C. Persson. Anisotropic hole-mass tensor of CuIn(1-x)Ga(x)(S,Se)(2): Presence of free carriers narrows the energy gap. *Applied Physics Letters*, 93(7), Aug 2008.

[Pos04] A.V. Postnikov and M.V. Yakushev. Lattice dynamics and stability of CuInSe2. *Thin Solid Films*, 451:141–144, Mar 2004. Symposium on Thin Film and Nono-Structured Materials for Photovoltaics, Strasbourg, France, Jun, 2003.

[Put60] E.H. Putley. *The Hall Effect and Related Phenomena*. Butterworths, London, 1960.

[Rab98] M.K. Rabadanov and I.A. Verin. X-ray diffraction study of CuInSe2 single crystals. *Inorganic Materials*, 34(1):14–16, Jan 1998.

[Reg04] N. Rega. *Photolumineszenz von epitaktischen Cu(In,Ga)Se2-Schichten*. PhD thesis, Freie Universität Berlin, Hahn-Meitner-Institut, Feb 2004.

[Rin95] C. Rincón, S.M. Wasim, and J.L. Ochoa. Shallow donors, metallic conductivity, and metal-insulator transition in n-type $CuInSe_2$. *Phys. Status Solidi A-Appl. Res.*, 148(1):251–258, Mar 1995.

[Ris07] B.T. Rissom. *Elektrische Transporteigenschaften von epitaktischen und polykristallinen Chalkopyrit-Schichten*. PhD thesis, Freie Universität Berlin, Hahn-Meitner-Institut, May 2007.

[Rot06] J. Rothman, J. Meilhan, G. Perrais, J.-P. Belle, and O. Gravrand. Maximum entropy mobility spectrum analysis of HgCdTe heterostructures. *Journal of Electronic Materials*, 35(6):1174–1184, Jun 2006. US Workshop on the Physics and Chemistry of II-VI Materials, Cambridge, MA, Sep 20-22, 2005.

[Rot10] J. Rothman, 2010. CEA Grenoble, France, private communications.

[Sche11] R. Scheer and H.-W. Schock. *Chalcogenide Photovoltaics – Physics, Technolohies, and Thin Film Devices*. Wiley-VCH, Weinheim, Germany, 1st edition, 2011.

[Schul02] S. Schuler. *Transporteigenschaften und Defekte in polykristallinen $CuGaSe_2$-Schichten und Heterostrukturen*. PhD thesis, Freie Universität Berlin, Hahn-Meitner-Institut, May 2002.

[Schum78] B. Schumann, C. Georgi, A. Tempel, G. Kühn, Nguyen Van Nam, H. Neumann, and W. Hörig. Epitaxial Layers of $CuInSe_2$ on GaAs. *Thin Solid Films*, 52(1):45–52, 1978.

[Schum81] B. Schumann, H. Neumann, E. Nowak, and G. Kuhn. Influence of Substrate Surface Polarity on Epitaxial Layer Growth of $CuInSe_2$ on GaAs. *Crystal research and Technology*, 16(6):675–680, 1981.

[See02] K. Seeger. *Semiconductor Physics – An Introduction*. Springer, Berlin, Heidelberg, New York, 8th edition, 2002.

[Sha75] J.L. Shay and .J.H. Wernick. *Ternary Chalcopyrite Semiconductors: Growth, Electronic Properities, and Applications*. Pergamon Press, Oxford, 1975.

[Sie05] S Siebentritt. Hole transport mechanisms in CuGaSe2. *Thin Solid Films*, 480(SI):312–317, Jun 2005. EMRS Symposium on Thin Film Chalcogenide Photovoltaic Materials, Strasbourg, France, May 24-28, 2004.

[Sie07] S. Siebentritt, T. Eisenbarth, M. Wimmer, C. Leendertz, F. Streicher, S. Sadewasser, and M.C.. Lux-Steiner. A Sigma 3 Grain Boundary in an Epitaxial Chalcopyrite Film. *Thin Solid Films*, 515(15):6168–6171, May 2007. Symposium on Thin Film Chalcogenide Photovoltaic Materials Held at the EMRS 2006 Spring Conference, Nice, FRANCE, MAY 29-JUN 02, 2006.

[Sie08] S. Siebentritt and T. Rissom. Metastable behavior of donors in CuGaSe(2) under illumination. *Applied Physics Letters*, 92(6), Feb 2008.

[Sie11] S. Siebentritt, 2011. Universite du Luxembourg, TDK Professorship, private communications.

[Str99] G.B. Stringfellow. *Organometallic Vapor-Phase Epitaxy: Theory and Practice.* Academic Press, 2nd edition, 1999.

[Sze81] S.M. Sze. *Physics of Semiconductor Devices.* Wiley-Interscience, 1981.

[Uma10] G. A. Umana-Membreno, J. Antoszewski, L. Faraone, E. P. G. Smith, G. M. Venzor, S. M. Johnson, and V. Phillips. Investigation of Multicarrier Transport in LPE-Grown Hg(1-x)Cd(x)Te Layers. *Journal of Electronic Materials*, 39(7):1023–1029, Jul 2010. 28th United States Workshop on Physics and Chemistry of II-VI Materials, Chicago, IL, Oct 06-08, 2009.

[Vur98] I. Vurgaftman, J.R. Meyer, C.A. Hoffman, D. Redfern, J. Antoszewski, L. Faraone, and J.R. Lindemuth. Improved quantitative mobility spectrum analysis for Hall characterization. *Journal of Applied Physics*, 84(9):4966–4973, Nov 1998.

[Was84] S.M. Wasim and A. Noguera. Transport Properties of n-Type $CuInSe_2$. *Phys. Status Solidi A-Appl. Res.*, 82(2):553–559, 1984.

[Was86] S.M. Wasim. Transport Properties of $CuInSe_2$. *Solar Cells*, 16(1-4):289–316, Jan-Feb 1986.

[Wei77] H. Weinert, H. Neumann, H.J. Hobler, G. Kuhn, and N. VanNam. Infrared Faraday-Effect in n-Type $CuInSe_2$. *Physica Status Solidi B – Basic Research*, 81(1):K59–K61, 1977.

[Yu10] P.Y. Yu and M. Cardona. *Fundamentals of semiconductors: physics and materials properties.* Springer Verlag, 4th edition, 2010.

[Zhan98] S.B. Zhang, S.H. Wei, A. Zunger, and H. Katayama-Yoshida. Defect physics of the CuInSe2 chalcopyrite semiconductor. *Physical Review B*, 57(16):9642–9656, Apr 1998.

[Zhao04] Y.J. Zhao, C. Persson, S. Lany, and A. Zunger. Why can CuInSe2 be readily equilibrium-doped n-type but the wider-gap CuGaSe2 cannot? *Applied Physics Letters*, 85(24):5860–5862, Dec 2004.

List of Figures

List of Tables

Acknowledgements

Many people have directly or indirectly contributed to this work and I would like to thank all of them. This work would not have been possible without you!

First I want to thank my supervisor Susanne Siebentritt for giving me the opportunity to work in the LPV team and for guiding me into the world of photovoltaics. Thank you very much for our discussions, for your ideas, and for your always successful efforts to find time even if you had none.

Furthermore, I want to thank Sascha Sadewasser and Roland Sanctuary for agreeing to be members of the CET and Silvana Botti and Levent Gütay for being part in the defense committee.

It really was a pleasure for me to work in the LPV team. Every member of the group helped creating the excellent atmosphere and spirit. Especially I want to thank: Thomas Schuler for developing and maintaining the software for the experimental setup, for help with fractious software and for finding solutions for all (non standard) problems. Danielle Schoder and Patricia Ramoa for help with everything that needed more than a scientist or engineer. Maxime Thevenin for last minute SEM images and EDX data. David Regesch for the simulations of absorption and for help with the interpretation of the EDX results. My office mates Levent Gütay, Jes Larsen, Katja Hönes, Alex Redinger, Valérie Depredurand, and Yasuhiro Aida for many discussions and answers. Thomas Schuler, Dominik Berg and Jes Larsen for frequent help with the non remote parts of my remote control measurements and everybody else in the team for helping now and then, just always when I asked.

A special thanks goes to Johan Rothman at CEA Grenoble for introduction to mobility spectrum analysis and providing me his MEMSA software.

I also want to thank Matthias Altenhöfer for proof reading and for polishing my LaTeX tables.

A very important help were the many people who provided me bed & breakfast whenever I needed: Dominik, Katja, Valerie, Pit, Anna and Daniel, my parents and all the others who also offered me to stay at their place. Without you, I would probably have spent several hundred hours more on the European highways. Thank you, Michael, for accepting me as your office co-worker.

I am very grateful to my parents, Margit and Wolfgang Altenhöfer, for their enthusiasm about their grandchildren and the unlimited willingness to take care of them.

Finally I want to thank Fritzi, Emilian, and Helene for all the support you gave me. Thank you Fritzi for having been the best part time single mother in the world. Thank you Emilian and Helene for being so happy about the world and so friendly to your parents and everybody.